INFRARED HYPERSPECTRAL IMAGING FOR POINT-OF-CARE WOUND ASSESSMENT

by

BEN OLIVER LUKE MELLORS

A thesis submitted to The University of Birmingham for the degree of DOCTOR OF PHILOSOPHY

Physical Sciences for Health Doctoral Training Centre

College of Engineering and Physical Sciences

The University of Birmingham

September 2021

UNIVERSITY^{OF} BIRMINGHAM

University of Birmingham Research Archive

e-theses repository

Abstract

Wound healing assessment and management are both important in ensuring a correct healing sequence. Most of these assessment techniques involve simple observation with the naked eye, which causes two main issues: the parameters assessed are highly subjective, and they rely upon the knowledge and experience of a trained medical professional. Any failure or incorrect management can result in further complications and even fatality, therefore quantitative wound assessment techniques are the next step towards a more accessible and reliable wound management strategy.

Current research in this field is focused on utilising non-invasive imaging techniques, mainly within the visible and infrared (IR) range, to identify the biological and chemical changes during the wound healing process. Any abnormalities can then be identified earlier to aid in the correct diagnosis and treatment of the wound. Technologies that utilise concepts of non-contact imaging, such as optical imaging and spectroscopy can be used to obtain spatial and spectral maps of biomarkers, which provide valuable information on the wound (e.g., precursors to improper healing or delineate viable and necrotic tissue). This work extends this research further by investigating two different imaging modalities, Negative Contrast Imaging (NCI), along with Spatial Frequency Domain Imaging (SFDI) for the applications of point of care wound assessment.

Intelligent data analysis algorithms, in the form of k-means clustering and principal component analysis were applied to spectral data, collected from wound biopsies as part of a previous study, highlighting the ability to diagnose wound healing status from the contrast of spectral information, which is not reliant upon a subjective clinical diagnosis. These methods provided the motivation for a larger cell culture trauma

study, in which the NCI was utilised to obtain spectral reflectance maps across a 2.5-3.5 μm wavelength region of both healthy and traumatised human epidermal fibroblasts, induced via chemical assays. Using the same intelligent analysis tools, along with pre-processing methods including spectral derivatives, the resulting clusters can be utilised as a diagnostic tool for the assessment of cellular health and were quantifiable metrics were defined to compare the different analysis methods

Near infrared (NIR) methodologies were also investigated, with two areas of SFDI identified for further advancements. Current SFDI acquisition and optical property parameter recovery is performed via a pixel-wise process, generating large amounts of data and a high computational burden for parameter recovery. Data reduction, through the application of Compressive Sensing (CS) at both the image acquisition and data analysis stages provided up to a 90% reduction in data, whilst maintaining <10% error in recovered absorption and reduced scattering optical maps.

This pixel-wise methodology also affects the forward modelling and inverse problem (imaging), based upon the diffusion approximation or Monte-Carlo methods due to their pixel-independent nature. NIRFAST, an existing FEM based NIR modelling tool, was adapted to produce pixel-dependent forward modelling for heterogenic samples, providing a mechanism towards a pixel dependent SFDI image modelling and parameter recovery system.

Acknowledgments

I would like to first thank my three supervisors for this PhD project. Dr Abigail Spear for her support in understanding the underlying biology and guidance throughout my time at Dstl for data collection. Dr Chris Howle for his knowledge of the negative contrast imaging system and help with initial system training. My greatest appreciation goes to Professor Hamid Dehghani, whose unquestionable dedication to research in all aspects of biomedical imaging allowed me to explore new techniques within the lab and university, whilst also being available for weekly meetings, discussing all aspects of work, whilst developing additional soft skills that are invaluable for life after a PhD. A special mention should also go to both Dr Kelly Curtis and Sara Macildowie, both of Dstl, for their support and friendship during my time at Porton Down. I would also like to thank the Physical Sciences-for-Health CDT, along with all my colleagues and supervisors across the 4-year programme for providing the knowledge and guidance to pursue the broad range of topics covered across my time in Birmingham.

I would like to acknowledge my friends and colleagues in the Medical Imaging lab, both past and present, for making each day a great place to work and learn, and those more senior for mentoring and advise about the various stages of the academic process. In particular, Dr Daniel Lighter and Dr George Rowley for guidance, and Alex Bentley and Guy Perkins who made working in a dark basement more enjoyable than first seemed possible.

I would like to thank my friends outside of UoB for listening to random bits of science over the course of my 8+ years in university and my family for supporting me in following my dreams whilst continually sparking my interest in the wider world.

Finally, my appreciation to my fiancée, Dr Sophie Broadway-Stringer, who has been a part of my life throughout my academic studies, without which none of it would be possible, and I would not be stood where I am today.

Publications

Journal Papers

The application of NIRFAST to spatial frequency domain forward modelling, working towards pixel-dependent methodologies. Validation of a finite element-based method within both the spatial and frequency domain, before demonstrating the importance of pixel dependency for increased heterogenic models. This paper forms the work presented in Chapter 6.

> **Mellors B.O.L.,** and Dehghani H. A Pixel-Dependent Finite Element Model for Spatial Frequency Domain Imaging Using NIRFAST. Photonics 2021, 8, 310.

Compressive Sensing was applied to different stages of the spatial frequency domain imaging analysis workflow, with a data reduction of up to 90% capable, whilst maintaining parameter recovery accuracy. This work is presented in Chapter 5.

> **Mellors B.O.L.,** Bentley A., Spear A.M., Howle C.R., and Dehghani H, November 2020. Applications of compressing sensing in spatial frequency domain imaging. Journal of Biomedical Optics, 25(11), p112904

A novel cell trauma study which utilises machine learning methods for the classification of spectral data from a hyperspectral negative contrasting imaging result. K-means, PCA and spectral derivative data processing methodologies were

applied, with a >94% accuracy in classifying healthy/traumatised cell cultures, with work presented in Chapter 4.

Mellors B.O.L., Spear A.M., Howle C.R., Curtis K., Macildowie S. and Dehghani H, September 2020. Machine learning utilising spectral derivative data improves cellular health classification through hyperspectral infra-red spectroscopy. PLOS ONE, 15(9), p0238647

Conference proceedings

The development of a numerical simulation tool for spatial frequency domain imaging, validated against current methods for parameter recovery, alongside the demonstration of heterogenic light propagation simulations. This work contributes to Chapter 6.

Mellors B.O.L. and Dehghani H., June 2021. Application of Numerical Methods for Heterogenic Spatial Frequency Domain Imaging Simulations
. European Conference of Biomedical Optics, OSA, EM2C.3.

Implementation of a pixel-dependent forward modelling tool for spatial frequency domain imaging. Simulations of both homogenous and heterogenous samples, demonstrating a novel forward modelling tool. This work contributes also to Chapter 6.

Mellors B.O.L. and Dehghani H., March 2021. Towards pixel-dependent spatial frequency domain imaging modelling and recovery. Photonics West, SPIE BiOS, 1163919

Investigation into the applications of compressive sensing algorithms upon heterogenic spatial frequency domain imaging data. Optimisation of the appropriate compressive sensing approach for the data collection stage of the modality workflow. This work is presented in Chapter 5.

Mellors B.O.L., Howle C.R., Spear A.M. and Dehghani H., April 2020. Compressive Sensing Based Spatial Frequency Domain Imaging Reconstruction. Biophotonics Congress: Biomedical Optics 2020, OSA, SW2D.4.

Preliminary study on the application of machine learning algorithms for the detection of cellular health using hyperspectral data, with this work shown in Chapter 4

Mellors B.O.L., Spear A.M., Howle C.R. and Dehghani H., April 2020*. Cellular health detection using Machine Learning and hyperspectral NIR. Laser Applications in Life Sciences. *Conference delayed due to Covid-19.

Novel utilisation of a liquid-air interface configuration and a negative contrast imaging device reflectance imaging system for the collection of spectral data from live cells within an in vitro environment. This work contributes to the first part of Chapter 4.

Mellors B.O.L., Dehghani H., Howle C.R. and Spear A.M., July 2019. Cell Trauma Detection Using Infra-red Live Cell Imaging. European Conference of Biomedical Optics, OSA, 110730M.

Initial study on the use of machine learning for hyperspectral data from both negative contrast imaging and Fourier-transform infrared spectroscopy. This study is shown in Chapter 3.

Mellors B.O.L., Dehghani H., Howle C.R. and Spear A.M., March 2019. Mid-infrared spectroscopic imaging to assess wounded tissue health. Photonics West, SPIE BiOS, 10873OU.

Contents

List of Figures

List of Tables

Abbreviations

â	Photon vector
ADT	Active dynamic therapy
ALI	Air-liquid interface
BG	Background
c	Speed of light
c_i	Chromophore concentration
C_x	Covariance Matrix
CaF_2	Calcium Fluoride
CCD	Charge-coupled device
CMOS	Complementary metal oxide semiconductor
CS	Compressive Sensing
cs-SFDI	Compressive Sensing Spatial Frequency Domain Imaging
D	Diffusion coefficient
DA	Diffusion Approximation
DIRT	Dynamic infrared thermography
DMD	Digital micromirror device
DMS	Defence Medical Services
Dstl	Defence Science Technology Laboratory
E	Photon Energy
f	Frequency
FEM	Finite element method
FGF	Fibroblast growth factor

FoV	Field of View
FTIR	Fourier-Transform Infrared
h	Planck's constant
HCI	Health Clustering Index
GUI	Graphical User Interface
H_2O	Water
H_2O_2	Hydrogen Peroxide
HbO	Oxyhaemoglobin
HbR	Deoxyhaemoglobin
HDFa	Human dermal fibroblast
HSI	Hyperspectral Imaging
I	Intensity
ICGA	Indocyanine green video-angiography
ICOPO	Intracavity optical parametric oscillator
IR	Infrared
k	Cluster Number
KNN	k-nearest neighbour
L	Path length
LDA	Linear discriminant analysis
LLI	Liquid-liquid interface
LDI/LDPI	Laser doppler perfusion imaging
LED	Light emitting diode
LSI/LSCI	Laser speckle contrast imaging

MCT	Mercury Cadmium Telluride
ML	Machine learning
MSI	Multispectral Imaging
MWIR	Mid-wave infrared
n	Refractive index
NADH	Nicotinamide adenine dinucleotide
NCI	Negative Contrast Imaging
NIR	Near infrared
NIRS	Near-infrared spectroscopy
NMRC	Naval Medical Research Center
OCT	Optical Coherence Tomography
OPCP	Operational Patient Care Pathway
PC	Principal Component
PCA	Principal Component Analysis
PET	Polyethylene terephthalate
PLS	Partial least squares
PS-OCT	Polarization sensitive optical coherence tomography
RGB	Red Green Blue
RMS	Root Mean Squared
ROI	Region of interest
RTE	Radiative transport equation
SFDI	Spatial Frequency Domain Imaging
SFM	Serum free media

SSOP	Single snapshot of optical property
SVD	Singular value decomposition
SVM	Support vector machine
SWIR	Short-wave infrared
TCI	Trauma Clustering Index
TRLs	Technology readiness levels
UV	Ultraviolet
VN1D	Vector Normalised 1st Derivative
VP	Virtual Photonics
λ	Wavelength
θ	Angle
ε$_i$	Excitation coefficient
μ$_a$	Absorption coefficient
μ$_s$	Scattering coefficient
μ$_s$'	Reduced scattering coefficient

CHAPTER 1

1 Introduction

1.1 Background

Traumatic injuries, whether in military or civilian personnel, are a leading cause of mortality and morbidity worldwide, accounting for 11% of the global burden of disease [1]. Wound assessment and management from point of injury throughout the evolution of the wound are important to ensure appropriate healing with minimal scarring and to avoid an acute wound becoming chronic in nature. The majority of wound assessment techniques currently employed in clinical practice involve simple observation with the naked eye, which causes two main issues: the parameters assessed are highly subjective, and they rely upon the knowledge and experience of a trained medical professional. Any failure or incorrect management can result in further complications and even fatality [2]. Therefore, objective and quantitative wound assessment techniques, which are preferably non-invasive, would provide a step-change in realising a more accessible and reliable wound management strategy.

Current research in this field is focused on utilising optical imaging techniques, mainly within the visible and near infrared (NIR) range, in order to identify the biological and chemical changes during the wound healing process, often in an non-invasive manner [3, 4]. Any abnormalities can then be identified earlier to aid in the correct diagnosis and treatment of the wound. Whilst these methodologies have offered some advancements in the field, limited work has been performed beyond this, particularly

from the NIR into the short-wave infrared (SWIR) and mid-wave infrared (MWIR) regions using non-invasive modalities. This work aims to address this through the development of state-of-the-art imaging methodologies for wound monitoring applications. Due to the interdisciplinary nature of this work, a grounding in the fundamental biology of wound healing is presented within this chapter, along with further motivations for this work.

Chapter 2 then considers the background of optical imaging within biological tissue, before presenting a review of current imaging modalities within the field. Chapter 3 presents novel analysis of data obtained from combat wound biopsies by the Defence Science Technology Laboratory (Dstl) to maximise the information gathered from precious clinical samples.

Chapter 4 then applies these methods to cellular trauma data, collected using a negative contrast imaging (NCI) device. Full details of the cell trauma methodology are presented, alongside the use of a unique signal detection technique.

Chapter 5 then considers the use of Spatial Frequency Domain Imaging (SFDI) for wound healing assessment, focusing upon the application of Compressive Sensing (CS) to the image analysis protocols. Chapter 6, the final results chapter, investigates the implementation of a finite element method (FEM) tool for numerical based simulations for SFDI, before overall conclusions and future work are discussed in Chapter 7.

1.2 Thesis Contributions

In this thesis, contributions are made to the wound healing field through the investigation of two imaging modalities, NCI and SFDI. Improvements to the data

analysis steps alongside novel applications of the techniques to biologically relevant data, in the form of wound biopsies, cell cultures, human hand imaging and tissue models have been made. Primarily, these can be broken down into key areas:

- Intelligent data analysis, through the application of clustering and data reduction methodologies, of historical spectral data from wound biopsies demonstrates non-subjective methods for assessing wound healing state. This work demonstrates the additional information available across the full spectral region to aid in sample discrimination. These methods provide the basis for a further cell culture study.

- To further assess the intelligent analysis methods developed, cell cultures of wound relevant human keratinocytes were utilised alongside a trauma inducing assess to create samples for novel NCI spectral analysis. Using the ground truth sample information demonstrates accurate clustering of healthy and traumatised samples using pre-processing in the form of background subtracted spectral derivative data. This further demonstrates the applicability of intelligent data analysis methods for non-subjective wound assessment.

- Alongside this, SFDI methodologies were investigated for data reduction approaches, moving towards hyperspectral data collection. Here it was shown that compressive sensing, on biologically relevant samples of increased heterogeneity, were able to be reconstructed at both the image acquisition and data analysis stage using reduced data.

- Additionally, through the adaptation of existing FEM based modelling tools, forwards modelling of samples of increasing heterogeneity were modelled for

pixel-dependent SFDI. This work advances the modelling capabilities for wound healing applications, moving towards improved parameter recovery and hyperspectral modelling

Overall, this these contributes the foundations for improved wound healing methodologies and approaches to reduce the reliance upon subjectivity gold standard tools that rely upon trained and experience clinicians.

1.3 Wound Healing

The wound healing process is a natural and complex series of events that occurs following tissue injury. These events take place at both the cellular and molecular level, resulting in the resurfacing, reconstruction and overall restoration of the injured tissue [5]. Whilst this process is continual, it is often broken down into four key overlapping phases: Haemostasis, Inflammation, Proliferation and Maturation [6] (Figure 1.1). Each of these phases must occur for a wound to heal correctly, and any deviation from this can result in incomplete healing or lead to further complications such as infection.
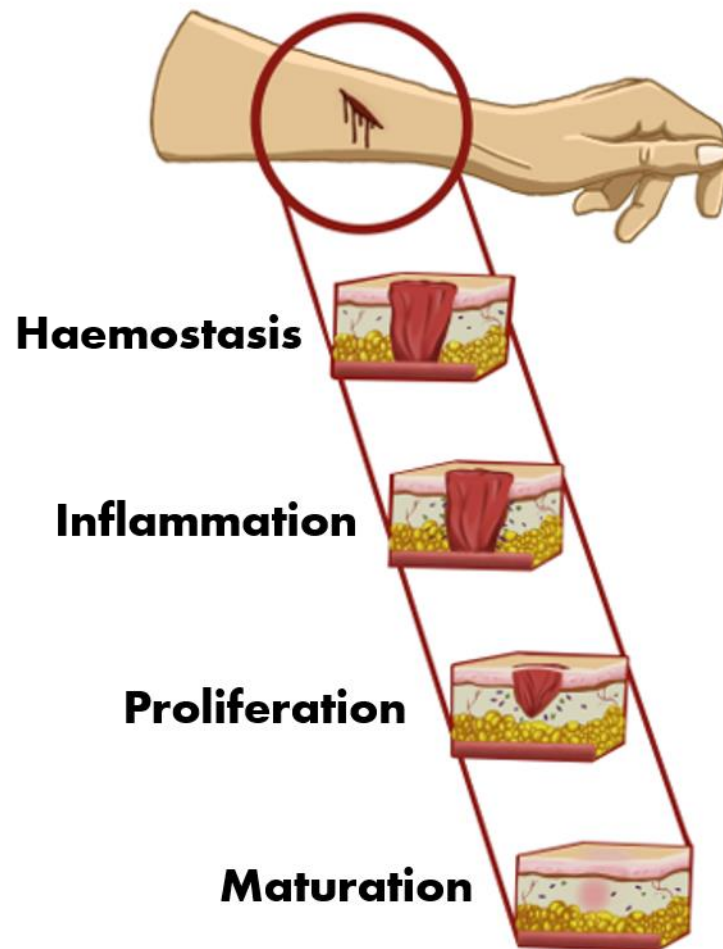
Figure 1.1: The four stages of wound healing. Schematic representation of each of the four wound healing phases.[1]

1.3.1 Haemostasis

The first stage of the wound healing process is haemostasis. When wounding occurs, breaching the epidermis, and other structures depending on the severity of the wound, blood vessels are disrupted, and blood constituents are leaked from the wound. From the very first moments of injury, molecular and cellular processes are initiated to form a clot in order to stem the loss of blood. Initially, the blood vessels supplying the affected area constrict, in a process called vasoconstriction. This limits

---

[1] Figure created by Hollie Broadway-Stringer

the supply of blood and reduces the initial blood loss, which causes the wound to temporarily blanch. The revealed subendothelium causes platelet activation upon attachment to the exposed collagen. This then releases cytokines, chemokines and hormones, such as fibroblast growth factor (FGF), in order to control the bleeding whilst promoting clot formation. Alongside this, chemokines then attract inflammatory cells to the wounded area, in a process called chemotaxis, before the next phase begins. This stage is initiated immediately following injury and can last for up to 3 days, but it is primarily active within the first hour post-trauma [7].

1.3.2 Inflammation

Following the activation of platelets, inflammatory cells, including neutrophils, macrophages and lymphocytes migrate to the wounded area. Neutrophils are the predominate cells in the early stages of inflammation. They have many functions, with one of the most important being the removal of both invasive microbes and cellular debris. During this phase, clinical signs such as swelling, pain and redness occur. Macrophages initially release cytokines, to recruit additional leukocytes to increase the inflammatory response [8]. They also play a key role in the healing process by inducing and removing apoptotic cells. Lymphocytes are also an important cell type during this phase, although their role is not fully understood, but it is believed they are important for cellular immunity and antibody production [9, 10]. Finally, macrophages undergo a phenotype transition that stimulates further cell types, initiating the next phase of wound healing [11].

1.3.3 Proliferation

The proliferation phase overlaps with inflammatory phase, beginning within 3-5 days of injury in regular wound healing. This phase can be split into different sub phases,

which do not occur in discrete time frames, but combine and overlap to contribute to the overall proliferation phase [12].

Epithelialisation

Epithelialisation (or re-epithelialisation) is the process of the reformation of the epithelium over the wound surface. Epidermal cells, such as keratinocytes, from the edge of wounded surface migrate short distances to generate a protective layer between the underlying wound and the environment. As the cells migrate, along intracellular actin microfilaments, they dissect the wound. They secrete collagenases and plasminogen activators, which promote the production of collagen and plasmin respectively. This process continues, with the cells interacting with the underlying matrix, until the wound is fully covered with the new epithelial layer [13].

Fibroplasia

Fibroplasia is the process in which new fibrous tissue is formed and begins between 3-5 days post injury and can last up to 14 days. Fibroblast cells are a key component in the formation of this tissue. They are responsible for the production of a variety of the extracellular components, such as collagen, elastin and fibronectin. The most important of these is collagen, which is secreted into the extracellular space in the form of procollagen, that undergoes further interactions to form the final collagen filaments [5].

Angiogenesis

Angiogenesis is the formation of new blood vessels, which is a vital process to help sustain the newly formed tissue. Macrophages produce angiogenic factors in response to low tissue oxygenation, which recruit additional endothelial cells. New

blood vessels are formed, increasing oxygenation and the delivery of healing factors to the wounded region [14].

Contraction

Wound contraction is the final sub-phase of proliferation and involves the movement of wound edges to close the wound defect. This contraction is dependent upon the myofibroblast activity and connection with the extracellular matrix [15].

1.3.4 Maturation

The remodelling stage is the final phase in the wound healing process. This stage typical occurs after 21 days of injury and can last for years. It is characterised by the continued degradation and deposition of collagen within the wound. Collagenases and matrix metalloproteinases aid in the removal of excess collagen, while inhibitors of metalloproteinases ensure a balance of between the removal of old collagen and formation of new fibres.

Type III collagen is remodelled to type I collagen, cellular activity is reduced and the number of vessels is also reduced in the wound area [16].

Overall, the wound healing process involves the interaction of multiple cell types, each performing different, and often multiple roles in a multiphase process. The complexity of this process creates many diagnostic problems, with improper healing likely at any stage, and that can be attributed to multiple factors. A visual representation of the wound healing timeline is shown Figure 1.2, with approximate duration for each phase and the overlapping that occurs also represented. This provides an estimation of the wound healing time scale, which is dependent on a

variety of additional factors such as the wound severity, patient age along with any underlying health conditions.
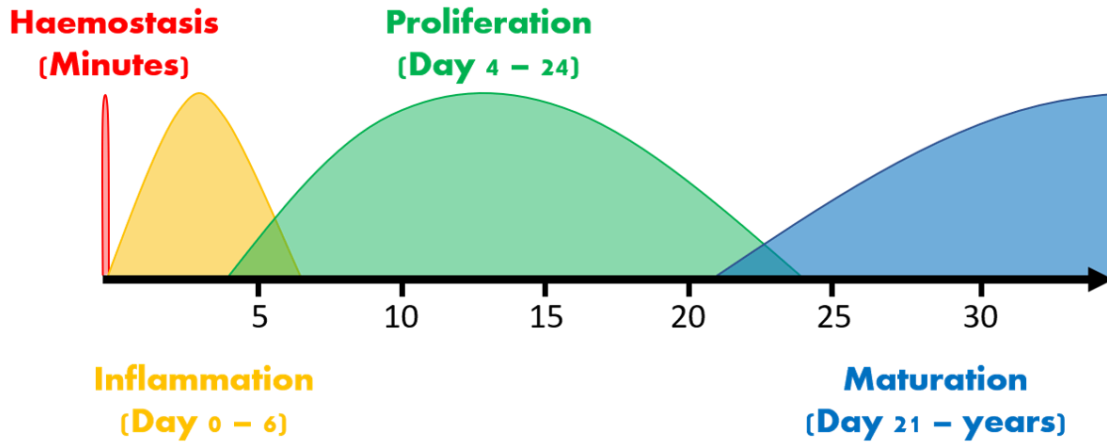
Figure 1.2: Wound healing timeline. The approximate duration of each of the four phases of wound healing is shown across the full wound healing timeline. The overlapping of phases is also represented.

1.4 Wound Healing Issues

With the high complexity and multistage nature of the wound healing process, there are many reasons how, and why, incorrect wound healing can occur. These factors can be split into two categories, local and systemic (Table 1.1).

Local Factors	Systematic Factors
Oxygenation	Age and Gender
Infection	Sex hormones
Foreign body	Stress
Venous sufficiency	Ischemia
	Diseases: *Diabetes, Keloids, Fibrosis, Hereditary healing disorders, Jaundice, Uremia*
	Obesity
	Medications
	Alcoholism and smoking
	Immunocompromised conditions
	Nutrition

Table 1.1: Factors affecting wound healing.

These factors can be involved singularly or simultaneously and can affect any of the four healing phases. Wound healing statistics show that, in the year 2017/18, wound management cost the NHS approximately £8.3 billion [17], with non-healing wounds affecting between 3-6 million people in the US [18].

1.5 Clinical Wound Assessment

Despite the significant cost of wound management, in both the NHS and worldwide, clinical wound assessment has changed very little in the last few decades. Wound assessment involves the identification and collection of information about the patient and how the wound occurred. Continued assessment of the wound is required throughout the healing process to identify any changes. Within the UK, initial assessment is commonly undertaken by a clinician, with follow up assessment completed by nurses, or other health care professionals. This highlights one of the

main issues with the current assessment methods, the introduction of subjectivity from different assessors [2].

To the author's knowledge, there is no standardised assessment tool for generic wounds. Assessment tools do exist for specific wound types however, such as the Bates-Jensen wound assessment tool, designed for pressure ulcers. This is a good example of the current gold standard method for wound assessment. The test consists of the measurement of 13 wound components independently, with a score between one and five given for each component. The components include clearly measurable values, such as wound size and epithelialisation coverage, but also many subjective measures including exudate amount (none, scant, small, moderate or large), as well as exudate type and necrotic tissue type. The scores are then totalled and recorded on a weekly basis, in order to track the wound healing process [19]. The full assessment tool is available in Appendix A.1. Despite some clear guidelines, assessment tools like this only increase the subjectivity further, with the assessment commonly completed by different practitioners with varying levels of training and experience.

1.6 Military Wounds and Assessment

The previous text highlights the general outline of wound healing difficulties and clinical assessments; however, special consideration must be given to wounds from the battlefield. Trauma sustained during combat provides some unique medical challenges, largely associated with the mechanism and severity of injury, and the environment and logistical context in which injuries are managed. The recent conflicts in Iraq and Afghanistan saw the development of allied post hoc trauma care to a point of capability never before achieved in war [20]. The mechanism of injury

produced by military munitions often generates injuries of a greater number and of a far higher severity than the relatively low energy mechanisms of, for example, a fall from height or a motor vehicle collision. Injuries often involve the loss of a large volume of tissue which may include traumatic amputation of more than one limb. Combat wounds are highly contaminated with fragment debris, clothing, soil, fungal spores, and foreign bacteria. The wounds also exhibit high levels of exudate and are prone to fungal and bacterial injections.

These unique challenges are then translated further during the assessment and management stage. Initial assessments are often performed by battlefield medics or trained soldiers, who all receive a basic training in wound management at the first instance [21]. Patients are then transferred through a series of dedicated medical facilities, generally of increasing sophistication, before final evacuation to a firm base. For the recent operations in Afghanistan this was the Queen Elizabeth hospital in Birmingham. The Operational Patient Care Pathway (OPCP) details how injured personnel should be managed from point of wounding up until evacuation to firm base when performing joint medical support on NATO operations [22]. The precise timelines and nature of this pathway may change depending on the location and environment of combat. Some of the current UK Defence Medical research requirements are geared towards consideration of a more complex and protracted OPCP than experienced in the conflict in Afghanistan. A cartoon depicting an example of this more complex OPCP can be seen in Figure 1.3 [23]. Regardless of the precise nature of the OPCP injured personnel will be subject to multiple wound assessments, in both sterile and non-sterile environments, further increasing the subjectivity of current wound assessment techniques. In an attempt to reduce some

of this subjectivity, simple digital photography is used by Defence Medical Services (DMS) during its wound management procedure. Images are taken at a variety of different stages, including during dressing changes. This allows the nurse/clinician to make independent comparisons of any progress made, with the previous assessment report providing additional information, opposed to the only source. This method has also been transferred to the field hospital using telemedicine, with consultations between the DMS and on-site clinicians common [24]. This technology has been taken one step further, with the use of 3D imaging within the clinic. These images offer additional details on wound topography and depth, with accompanying software that is able to accurately calculation wound area and volume [25].
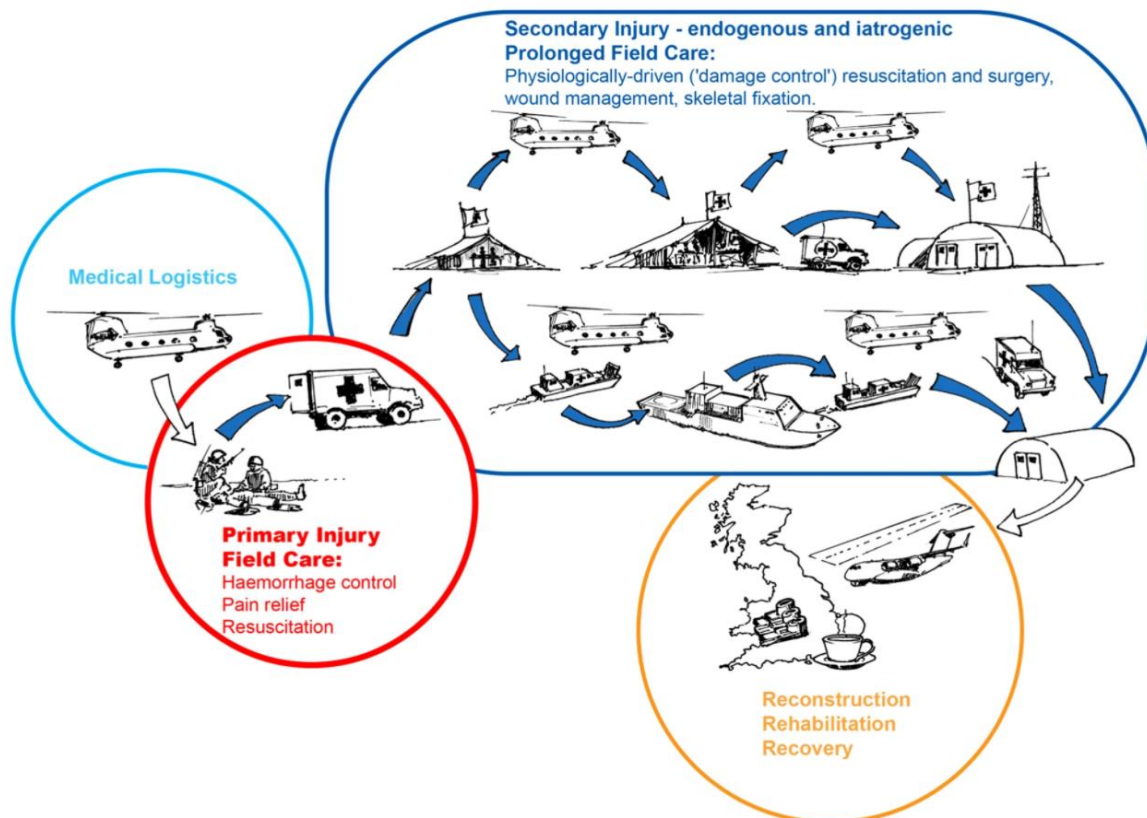
Figure 1.3: Operational Patient Care Pathway (OPCP). The main operational stages for a modern battlefield injury. This figure has been replicated from [23].

1.7   Wound Debridement

Whilst some wounds do heal naturally following the previously described four stage process, more complex wounds, such as those experienced within a military setting, require wound management to promote adequate healing. The main surgical intervention technique applied to wounds, particularly those of a more severe, complex nature, is wound debridement.   This is the first in a four step general process, known as DIME: Debridement, Inflammation management, Moisture control, and Environmental and Epithelialisation assessment [26]. Wound debridement is the removal of dead tissue, scar tissue, debris and any other material which will prevent regular healing. A clinician will assess a wound before any intervention is made, along with a surgical consult, to determine the boundaries for

14

the debridement. Multiple wound debridement's can occur on the same wound, with the continual assessment of the wound and surrounding tissue vital to ensure this step is not taken unnecessarily. Again, the designation of healthy tissue and that which is to be removed during debridement is performed in a subjective manner, whilst staining of wounds is possible [27], this is an invasive technique and cases of adverse reactions to the chemical dye have been reported, alongside impairments to the overall wound healing process [28, 29].

The boundaries of healthy/necrotic tissue occur at the cellular level, further compounding the issue of accurately identifying the correct tissue to remove. The removal of excess healthy tissue can further delay the wound healing process, whilst the failure to successfully debride the wound fully can result in infection with further wound healing complications. These issues are amplified in a military setting, with complex wounds, and further tissue loss from larger wounds. The magnitude of primary and secondary tissue loss demands novel reconstructive approaches and comprehensive programmes of functional rehabilitation [30].

1.8 Conclusion

The biological and chemical process for a full wounding pathway is complex, highly integrated, and subject to issues at any stages. Whilst the individual stages are understood, there has been limited improvements in the wound healing assessment methodologies. Current gold standard wound assessments are based upon visual observation throughout the healing process, performed by a variety of medical professionals with different levels of experience and training. This introduces the issues with the subjective form of opinions of varying wound assessors, and the subjectivity of the parameters themselves. These issues are compounded when

considering wounds from a military setting, due to both the complex logistical pathway and the severity and additional complications arising of the chronic wounds.

NIR imaging has been shown to address these issues, with multi-parameter assessment possible, using non-invasive, portable and robust methodologies, demonstrating the ability to utilise and advance these technologies for a point of care wound assessment tool. This chapter has shown the biological motivation for this work, whilst also introducing the background problem itself. The following chapter will provide a fundamental overview of imaging within biological tissues, before reviewing current imaging modalities that are being applied to the field of wound assessment.

Chapter 2

2 Wound assessment imaging technologies

Traditional wound assessment techniques, as discussed in section 1.5, rely heavily upon visual observation by trained and experienced clinicians. New technologies are currently in development to aid in this process, focusing on a wide variety of imaging techniques, including those in the visible and infrared (IR) wavelength regions. These techniques aim to provide further information on the wound characteristics, including quantification of oxygenation, haemoglobin and other wound relevant markers, such as lipid concentration and cytochrome-c-oxidase. With a better quantification of wound parameters, more accurate and objective assessments can be made, preventing unnecessary surgery, excessive tissue loss with a potential of saving lives.

Imaging methods collect information regarding the properties of the skin, wound bed and any other objects/tissue within a wounded area. These are analysed and interpreted, using intelligent data analysis methods, in order to assess overall wound severity, as well as wound healing potential and progress. These imaging techniques cover a broad range of wound types, with a large proportion focused on burns. Despite this initial focus area, these technologies are applicable to different wound types, with factors such as depth, size, vascularisation, and hydration all key to healing. These methods utilise the optical properties of soft tissue, which weakly absorb and highly scatter NIR light. This allows for a deeper interrogation, as compared to the ultraviolet (UV) and optical range.

2.1 Imaging biological tissue

In order to understand the requirements and challenges for imaging within biological tissues, the fundamentals of light interaction within the diffuse region of the electromagnetic spectrum must be discussed. Within this region, photon interaction is dominated by two principal effects, absorption, and scattering, which will be discussed further. The first interactions of light with tissue, regarding reflection and refraction will also be presented, to provide a thorough overview of tissue-light interactions.

The elementary particle used to quantise energy from the electromagnetic spectrum is called a photon. It is often described as a 'packet' of energy with its interactions at the atomic level key to the previously mentioned effects. A single photons energy, E, is dependent on its frequency, f, or wavelength, λ, as described by the Planck-Einstein relation shown in Equation 2.1.

$$E = hf = \frac{hc}{\lambda}, \tag{2.1}$$

where c is the speed of light in vacuum and h is Planck's constant [31]. When photons interact with biological tissue, the first phenomena occur at the tissue boundary. When the incident photon beam enters the biological tissue, the beam is either refracted or reflected, due to the differing refractive indices between mediums. This refractive index defines the speed at which the beams travels through any given media and is defined as the ratio between c and the speed of light within the medium [32]. Figure 2.1 depicts these interactions, between two separate media of refractive indices n_1 and n_2.
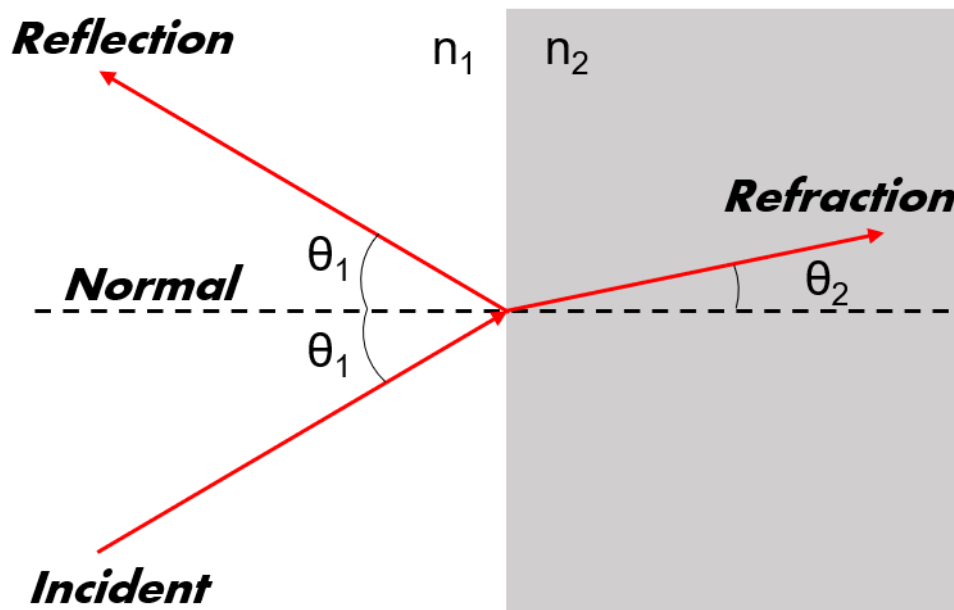
Figure 2.1: Reflection and refraction schematic. An incident light beam, propagating through a medium with refractive index n_1 at an angle θ_1 to the normal. The beam is reflected from the medium interface at the same angle, and/or refracted into the second medium, at an angle θ_2, determined using Snell's Law (Equation 2.2).

At this boundary, part of the beam is reflected at an angle θ_1 to the normal, equal to the incident angle. This reflection is also known as specular reflection. The remaining beam propagates through to the second medium where it undergoes refraction. This occurs due to the changes in both the speed and direction of the propagating beam, with the new propagation angle, θ_2, determined using Snell's law [33]:

$$n_1 sin\,\theta_1 = n_2 sin\,\theta_2. \qquad (2.2)$$

2.1.1 Absorption

Once an incident photon beam has propagated into the tissue, whose energy is not high enough to eject or ionise, the energy can be transferred to an electron within a molecule inside the medium. This absorption of the energy raises the electrons energy level, moving it to a higher state. As this beam travels through the medium,

the probability of a given photon being absorbed is defined by the absorption coefficient, μ_a.
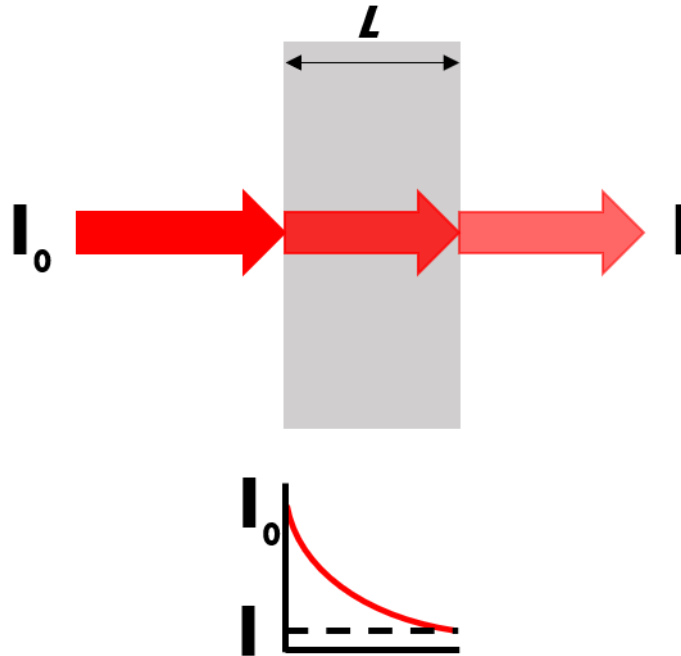
Figure 2.2: Absorption schematic.

As the beam attenuates through the medium, the resulting loss in intensity, in a purely absorbing medium, can be defined using the Lambert-Bouger law [34]:

$$I = I_0 e^{-\mu_a L},\qquad(2.3)$$

where, I_0 is the incident light intensity, L, the pathlength and, I, the residual intensity. This is represented with the schematic shown in Figure 2.2 with the exponential decay of the Lambert-Bouguer law also shown. The absorption coefficient is dependent upon the medium's chromophore concentrations through the Beer-Lambert law [35]:

$$\mu_a(\lambda) = \sum_{i=1}^{n} \varepsilon_i(\lambda) c_i,\qquad(2.4)$$

where, within a given medium containing i chromophores, ε is the wavelength dependent excitation coefficient and c_i is the chromophore concentrations. The

excited electron will also return to its ground state, through processes including fluorescence, where a photon of energy equal to the difference in ground and excited state is realised from the molecule, which will be discussed later within this chapter.

2.1.2 Scattering

Within biological tissue, light propagation in the visible-MWIR range is described as diffuse, which is where scattering is the dominant interaction. When a photon changes direction due to interaction with a particle within the medium, the photon will scatter with no energy transferred (elastic) or a small transfer (inelastic) due to the differences in refractive index between the particle and medium background. Inelastic scattering is the basis for Raman spectroscopy (2.2.8), however these events are rare in biological tissue within the visible and NIR ranges. When the size of the scattering particle is comparable to the photon wavelength, as is the case with vis-NIR light and many biological constituents (cell membrane, nucleus, and mitochondria), elastic scattering occurs [36]. As with absorption, the probability of a scattering event can be defined using a single coefficient, μ_s, the scattering coefficient.
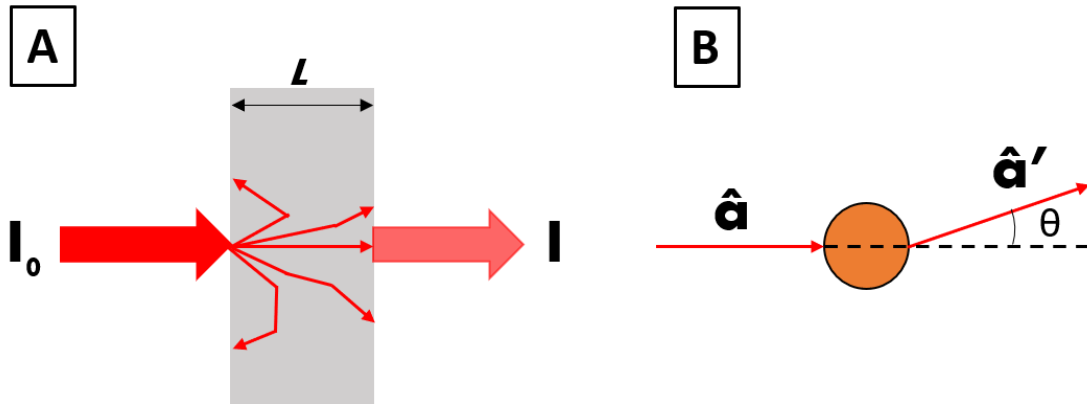
Figure 2.3: Scattering schematic. A: Scattering through a medium. B: Single scattering event.

The photons can scatter in both a forward or backward direction, with multiple scattering events possible. Assuming a scattering only medium, as shown in Figure 2.3 A, photons which scatters and transmit through the sample, contributing to *I*, the reduced transmitted intensity, via the following exponential relationship:

$$I = I_0 e^{-\mu_s L}. \tag{2.5}$$

Those photons that do not propagate through the length of the tissue can scatter back out of the medium, contributing to the diffuse reflectance. Whilst this coefficient contains information of the scattering probability, the angle of the scattered photon is not equal for all particles. The reduced scattering coefficient, μ_s', considers this angle through the anisotropy factor, *g*. The mean cosine value of the scattering angle, *θ* (Figure 2.3 B), is related to this factor, where an incident photon vector *â* is scattered to a new vector *â'*. The anisotropy has a value between -1 to 1, with -1 representing fully back scattered light, 0 an isotropic scatterer (equal in all directions) and 1, a fully forward scattering medium, whilst in biological tissue, typical values range from 0.7-0.99 [37]. The scattering, reduced scattering and anisotropic factor are related via:

$$\mu_s' = (1 - g)\mu_s.$$ *(2.6)*

Both μ_a and μ_s' have units of mm^{-1}, therefore the inverse of these coefficients contains information regarding the average propagation distance a photon will travel before experience either an absorption or scattering event.

2.1.3 Functional Imaging

Whilst absorption and scattering provide us with some information regarding a tissue or sample of interest, these parameters are dictated by the presence of different biological chromophores (Equation 2.4). To understand the contributions of these chromophores, and how these are utilised for the benefit of imaging biological tissue within the vis-MWIR window, a quantisation of different chromophores is required. For biological tissue, the key parameters are shown in Figure 2.4. This figure also highlights the importance of the optical window, in which water absorption remains low, whilst tissue chromophores, such as oxy- and deoxyhaemoglobin, fat, collagen, and cytochrome c have defined absorption spectra. The ability to quantise these chromophores provides the motivation for biological imaging within this wavelength window.
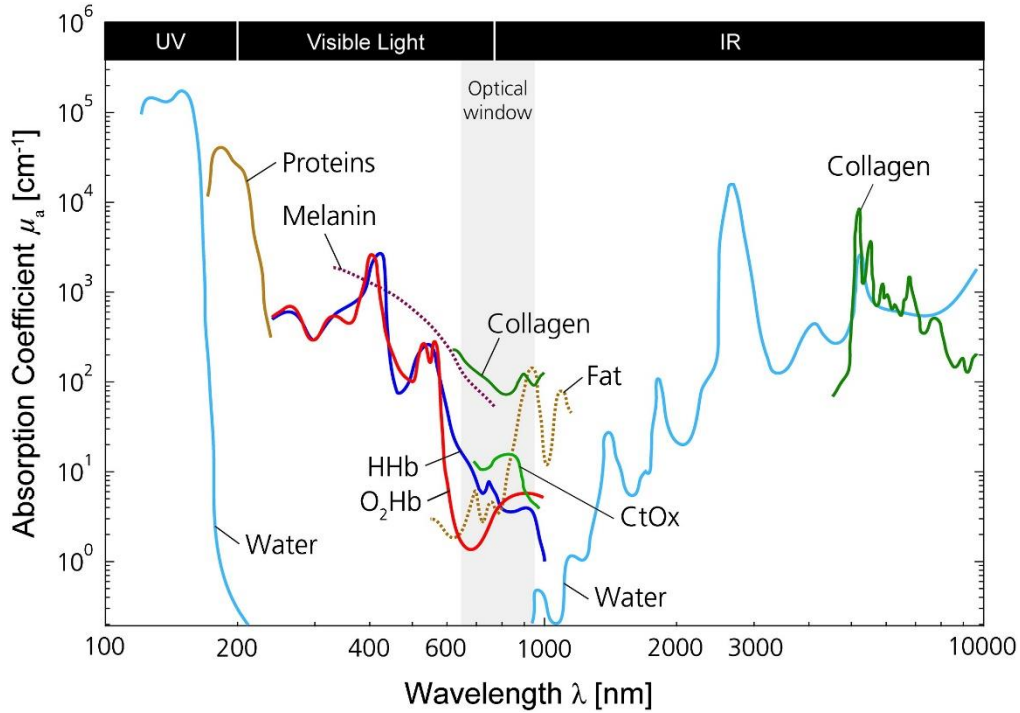
Figure 2.4: Absorption spectra for a key biological chromophores present in human tissue [38].

Haemoglobin is a key molecule whose absorption spectra is dependent on the presence of bound oxygen. The molecule is a water-soluble globular protein, consisting of two alpha and two beta chains, where HHb is the non-bound deoxyhaemoglobin molecule and O_2Hb oxyhaemoglobin [39]. Imaging at two or more wavelengths allows for the decoupling of these chromophore contributions, which can be utilised to determine two clinically relevant parameters: total haemoglobin (tHb) and oxygen saturation (StO_2), where:

$$tHb = HHb + O_2Hb, \qquad (2.7)$$

$$StO_2 = \frac{O_2Hb}{tHb}. \qquad (2.8)$$

These parameters are useful for both diagnostic and monitoring purposes for varying pathologies, including wound healing [40].

2.1.4 Radiative Transport Equation and Diffusion Approximation

With a knowledge of the fundamentals of photon interaction within biological tissue, alongside how these parameters can be used to determine chromophore concentrations for diagnostic and monitoring purposes, the final step is understanding how to extract this information through the modelling of light interactions. The radiative transport equation (RTE), also known as the Boltzmann equation, is a complex integro-differential equation used to model the transport of light through an absorbing and scattering medium [41]:

$$\frac{1}{c}\frac{\delta L(\vec{r},\hat{a},t)}{\delta t} = -\hat{a} \cdot \nabla L(\vec{r},\hat{a},t) - \mu_t L(\vec{r},\hat{a},t) +$$

$$\mu_s \int_{4\pi} L(\vec{r},\hat{a},t)P(\hat{a},\hat{a}')d\Omega' + S(\vec{r},\hat{a},t)$$

(2.9)

Where $L(\vec{r},\hat{a},t)$ is the radiance, defined as the energy flow per unit area per unit solid angle per unit time – at position $\vec{r}$, time, t, in direction $\hat{a}$. The total attenuation coefficient, μ_t, is defined as $(\mu_a + \mu_s)$, whilst P represents the probability of changing direction due to scatter all from the source $S(\vec{r},\hat{a},t)$. Due to its complexity, solving the RTE for all but the most trivial cases are both challenging and computationally expensive.

A series of assumptions can be made to simplify the RTE into the diffusion approximation (DA), allowing for an analytical solution. The given assumptions are as follows:

- The dominant photon interaction is scattering.
- Light fluence does not change rapidly with time.

- The region of interest is a large distance from both the source location and boundaries.

By expanding the source and the radiance, the DA can be defined as a first order, P_1 spherical approximation assuming isotropic distribution, resulting in a time dependent form [41]:

$$\frac{1}{c}\frac{\delta\Phi(\vec{r},t)}{\delta t} + \mu_a\Phi(\vec{r},t) - \nabla \cdot [D\nabla\Phi(\vec{r},t)] = S(\vec{r},t), \qquad (2.10)$$

where $\Phi(\vec{r},t)$ is the fluence rate, $S(\vec{r},t)$ is the isotropic source and D the diffusion coefficient, which is defined as:

$$D = \frac{1}{3(\mu_a + \mu_s')}. \qquad (2.11)$$

This represents a simplified approach to solving light propagation predictions, with varying forms of Equation 2.10 for different applications, such as time independent and continuous wave, which are common applications in biological light propagation models. Both the RTE and DA can be applied to varying models for simulating light propagation, with Monte Carlo models utilised to numerically solve the RTE [42], and FEM for discretised complex geometries, where simple infinite or semi-infinite analytical solutions of the DA are no longer valid [43]. These methods are applied across a variety of different imaging modalities for wound healing assessments, which the remainder of this chapter will review.

2.2 Non-invasive imaging wound assessment techniques

An important characteristic of these imaging modalities is that they are non-invasive. With the sensitivity of the wound healing process, and the high risk of infection, ensuring minimal interference with the wound is vital, which largely explains why the

current best practice is still visual inspection for clinical wound assessment. With these non-invasive methods, the true cellular environment of the wound is not disturbed or affected, allowing for uninterrupted data collection. A variety of these imaging techniques are discussed below, with a key gap in the literature identified at the SWIR/MWIR spectral range, alongside the need for robust analysis protocols, reducing the subjectivity associated with multiple visual assessments.

2.2.1 Photography

The simplest methodology for recording wound healing progression is using digital photography. A series of images, collected throughout the wound healing phases, can provide an accurate record of a variety of wound facets, such as size, colour, and healing progression [44, 45]. Considerations for simple issues, such as consistent imaging parameters including field of view, lighting, and resolution limit the wider availability of this technique. However, imaging with a digital camera is cheap and simple compared to other techniques to be discussed later. Advances in image processing and time-of-flight cameras allow for depth sensitive measurements and automated wound area monitoring, moving towards 3D structural imaging [46-48]. Despite these advantages, digital photography is only suitable for estimation of wound healing progression, applicable as a complimentary methodology, requiring validation from trained clinicians.

2.2.2 Thermography

Measurements of the emitted broadband IR photons from objects is known as thermography, or thermal imaging. Many objects, including skin and wounds, emit thermal IR photons and it has been proved that this radiation correlates to the temperature of the object. This allows for thermographic images from the wound

area to be analysed to identify changes in temperature, and with image processing, pseudo-coloured images can also be generated for simpler visual interpretation [49]. An example of a thermographic wound image is shown in Figure 2.5.
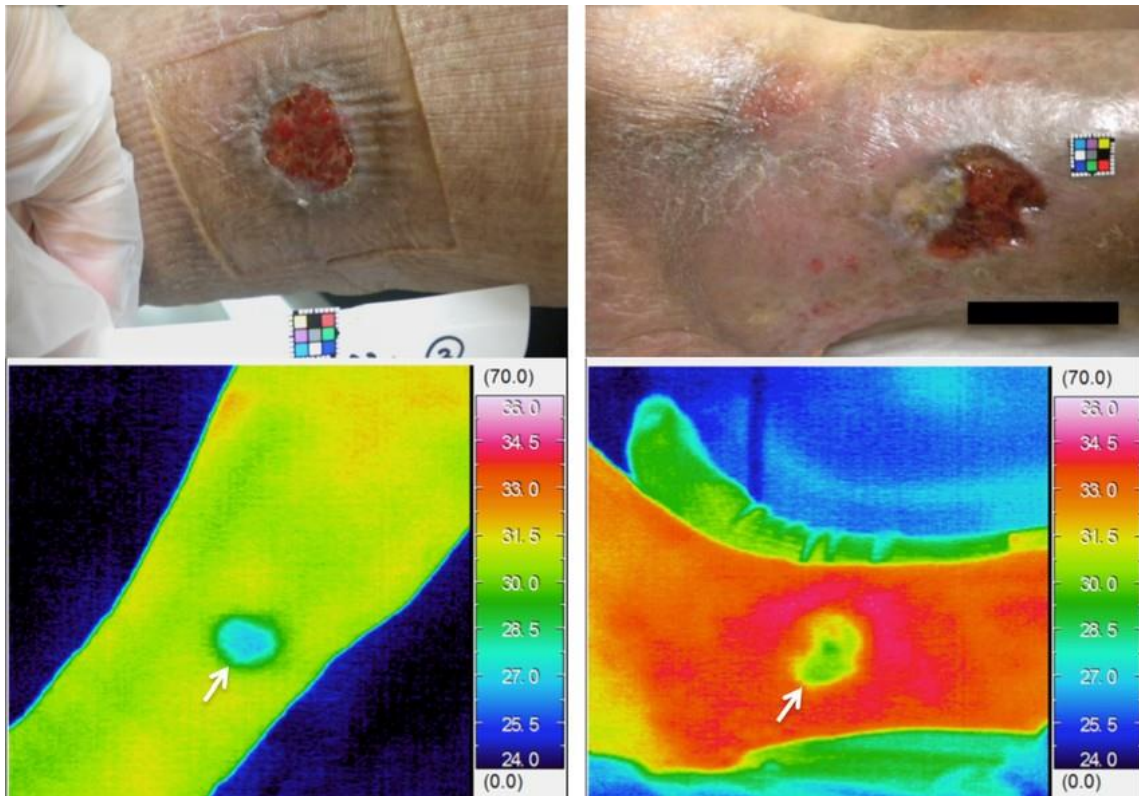
Figure 2.5: Example thermography images. Both the gross appearance and thermographic images are shown on a left and right ankle venous leg ulcer. Adapted from [49].

The use of thermography has been researched since the early 1960s, where it was implemented in the assessment of burn depth. It was found to have an accuracy of 90% in diagnosing the correct burn classification, when confirmed with histological measurements and is based upon the principle that burns are warmer than uninjured skin [50], whilst other wound types may be colder when observed in tissue, such as the ulcer shown in Figure 2.5. These studies have been continued further, with thermographic imaging used to predict the healing outcomes of burns, to determine if they will heal within a three week window or require excision [51].

A more advanced technique than the static thermography described above is active dynamic thermography (ADT). In this method, an initial set of static measurements is taken using the previously described thermography method of naturally emitting photons. This is then followed by thermal excitation, usually a halogen lamp, and subsequent imaging to detect the thermal diffusivity of different tissue components. ADT has been used along with high-resolution thermal imaging cameras to assess burn depths, with comparisons between the static IR and ADT methods, proving ADT is superior for burn depth classification [52].

With the increase in demand for faster and cheaper assessment methods, smart-phone apps are now being assessed for potential clinical use. This system works through a smartphone attached to a thermal imager, which is used to diagnose wound healing. Via an app, measurements of not only temperature, but also blood flow and wound inflammatory index can be taken to aid in a fast and effective wound assessment. The blood flow is measured using temporal temperate changes whilst the wound inflammatory index, as first proposed by Bharara *et.al.* is a quantitative measure of the wound temperature, isotherm area and total wound bed area [53, 54]. Despite these advantages, any measurements have yet to be taken on human tissue, and the modality only focuses upon blood flow. To measure this blood flow, the process of angiogenesis (section 1.3) needs to have already begun, with a more significant advantage being able to predict this process, making this an assessment tool rather than a diagnostic aid. However, with the simplicity of this system, it has potential for wider clinical use in poorer and less accessible medical facilities [53].

Thermography has not only been investigated with burn wounds, but also diabetic ulcers, pressure ulcers and other generic wound types [55]. One such wound type

is a free flap, experienced in some surgeries. Dynamic Infrared Thermography (DIRT) is used to indirectly determine blood perfusion through the recording of temperature in these skin flaps. This method has been compared to a current clinical method, indocyanine green video-angiography (ICGA). ICGA, however, is an invasive method, therefore with DIRT having been shown to perform comparably, it is a promising and preferable alternative [56].

2.2.3 Fluorescence Imaging

Fluorescence imaging is a technique that uses either endogenous or exogenous fluorophores within the skin. The basic concept of fluorescence imaging is to excite a fluorophore using a particular wavelength of laser light, followed by detection of the emitted light, which is filtered to ensure only the fluorescence emission is measured. The measured intensity is proportional to both the fluorophore concentration and size, which is used to determine the biological or chemical measurement of interest.

One of the most common techniques is the use of indocyanine green (ICG) dye, which can be used to determine vascularisation and burn depth [57]. The ICG dye is an exogenous dye and is injected into the circulatory system. In order to make the method non-invasive, endogenous fluorophores can be used. An example of this technique is fluorescence lifetime imaging. In this method, nicotinamide adenine dinucleotide (NADH) is used as a natural fluorophore. Found in the wound bed, NADH can be used as a marker in cutaneous wound healing [58]. This method allows for the quantification of cellular metabolism, which can be used along with other methods to improve the overall wound healing assessment procedure. Endogenous fluorescence has also been used for wound boundary infection

detection. Figure 2.6 depicts both a white light and fluorescent image for diabetic foot ulcer diagnostics. The red fluorescence depicts the infected tissue that is not-visible in the white image and would be missed using simple visual inspection techniques.
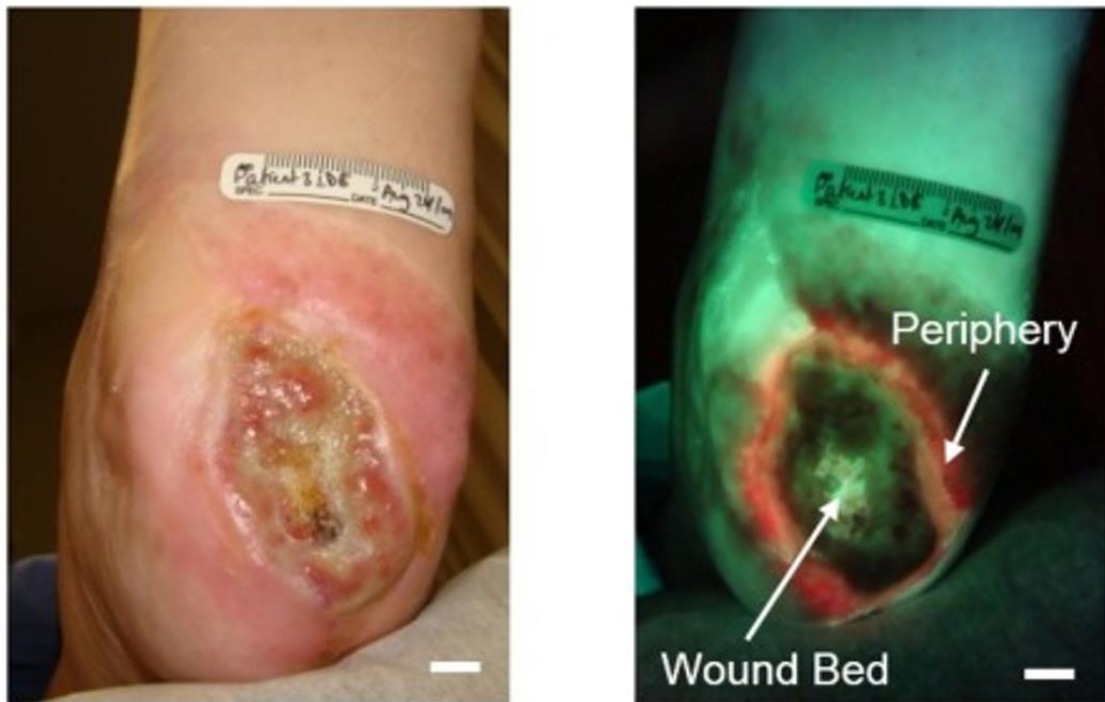
Figure 2.6: Endogenous fluorescence wound boundary detection. Comparison between white light and fluorescence imaging of a diabetic foot ulcer. Scale bars are 1 cm, image adapted from [59].

Despite the clear advantages of these techniques, issues arise with the complexity of the equipment required. The lasers and detectors often require trained and experienced clinicians, as well as controlled hospital conditions. In order to get assessments of wounds at an earlier stage, and in more diverse areas, such as battlefield hospitals or even the patient's home, investigations have begun into portable technologies. This research has initially focused on the application of skin healing rejections in transplants but would be applicable to all wound types. The device consists of 6 red laser diodes and has been shown to work with both auto-

fluorescence from tissue components, as well as exogenous fluorophores. This can detect levels of inflammation from the skin, and be used to assess the wound healing progression [60].

2.2.4 Spectroscopy

Visible Light Spectroscopy

Imaging spectroscopic methods are based upon combining a spectral light source, either broadband and modulated or narrow band and tuneable, to provide sample illumination at variable wavelengths, with a camera, or other light collection mechanism with a tuneable filter to collect the spectral response. The combination of these techniques collects a series of images, at each wavelength, generating spectral data of each pixel of the captured image. Depending on the number of spectra collected, these can be categorised as multispectral or hyperspectral.

In a traditional digital camera image, only light from three channels, red, green, and blue (RGB) is collected and used to build the image (Figure 2.7)
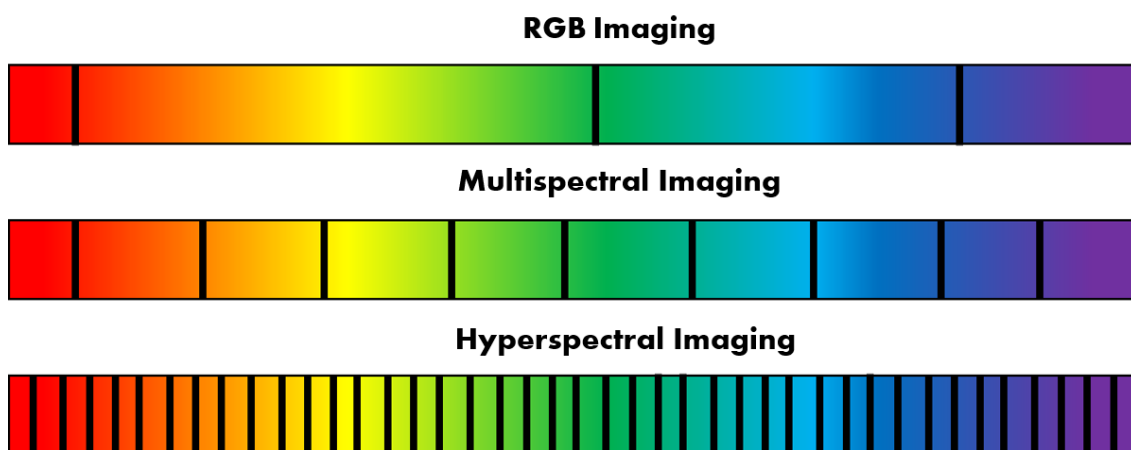
Figure 2.7 RGB, Multispectral and Hyperspectral Imaging.

However, in hyperspectral imaging (HSI), data is collected at a much higher resolution, often with hundreds of different images collected per sample. This

information is combined to generate a 3D data hypercube. This contains two spatial dimensions and one spectral dimension. Therefore, any hyperspectral image contains a spectral map of information, with the spectrum of each individual pixel available. An example of this is shown in Figure 2.7 [61]. Multispectral imaging (MSI), also shown in Figure 2.7, is similar to HSI. It also collects a 3D hypercube, with fewer wavelengths taken, often 10-100 per hypercube.
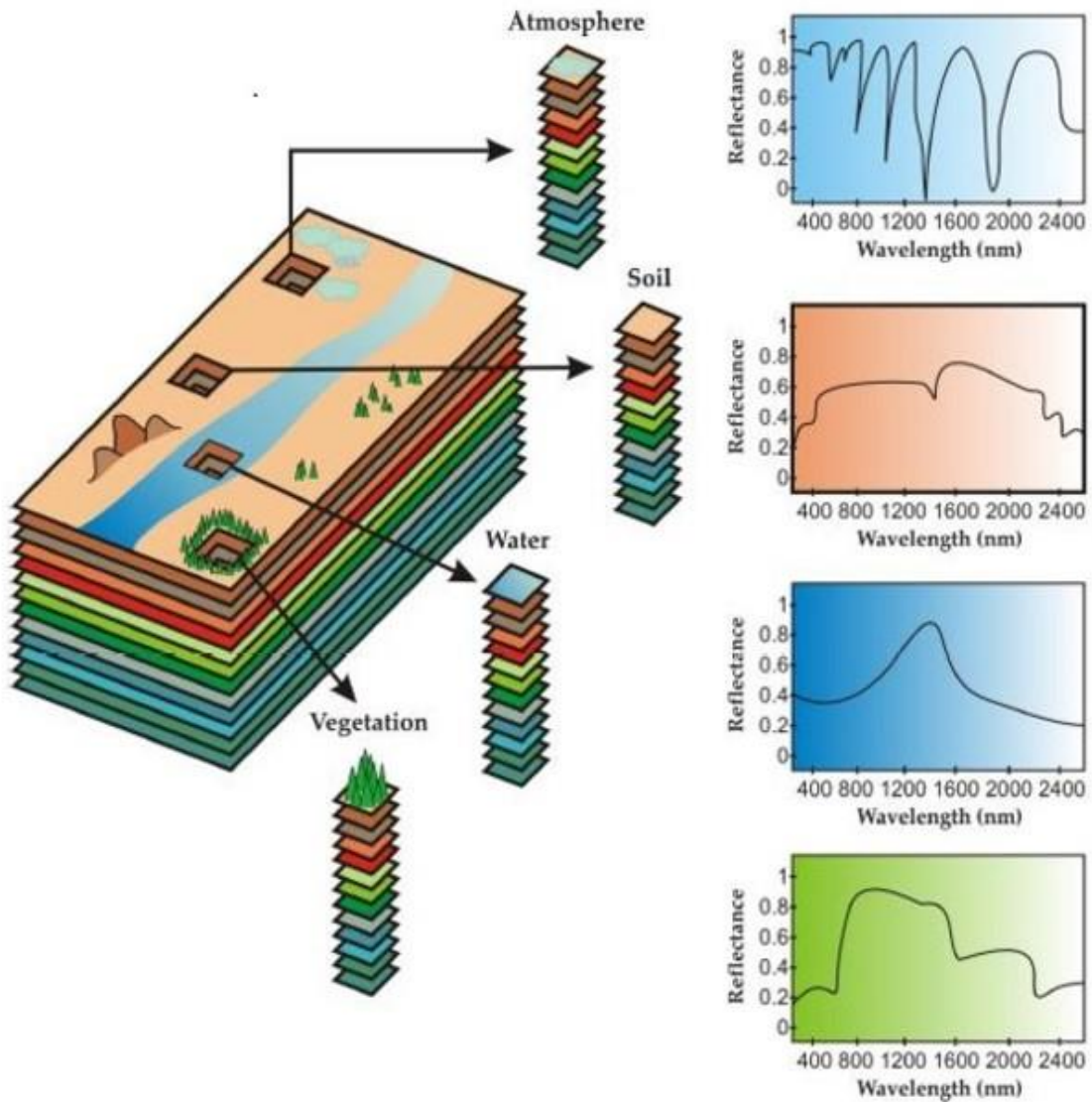
Figure 2.8: Hyperspectral imaging schematic. This figure has been replicated from [61].

HSI methods have been employed to assess a variety of different wound types and medical applications [62]. These methods traditionally use visible to near infrared light to investigate tissue oxygenation, via O_2Hb and HHb respectively. Other tissue parameters such as melanin content, burn characteristics, and epidermal thickness have also been measured [4]. Through the measurement of these parameters at multiple wavelengths, each of which has a depth dependency due to the differing

penetration depths of photons at varying wavelengths, information regarding the properties of the sample at varying depths can be obtained.

HSI is more commonly used as it offers higher spectral resolution as compared to multi-spectral measurements and is more suitable for the clinical setting, with modern system imaging within only a few seconds now achievable, compared to earlier imaging systems. A preliminary study by Calin *et.al* has used HSI to assess burn depth. Hyperspectral images of a leg and foot burn were taken 5 days post injury. These were taken with a simple imaging setup, consisting of only a hyperspectral camera, imaging 346 spectral bands between 400-1000 nm, and a pair of 300 W halogen lamps. The resulting images were then analysed and principal component analysis was used to identify different burn regions [63]. This study shows promising results and merits further investigation, with only one patient imaged for this initial study.

MSI has also been used widely but is often focused on specific wavelengths. MSI is used within the clinic currently, with dermatological detection of skin lesions [64], and is also being investigated in the assessment of diabetic foot ulcers. Traditional RGB imaging has been compared to MSI of 36 wavelengths between 430 - 780 nm imaging of *in vivo* artificial wounds upon pigs back, to assess chromophore mapping. It was found that multispectral imaging identified the ability to determine regions of the epithelium and those of granulated tissue, through the additional spectral information for discrimination, compared to simple RGB imaging, which can aid in both burn diagnostics and treatment [65].

Near Infrared Spectroscopy

Many instrumental methods in development for wound assessment utilise NIR light, 850 - 1000 nm. The soft tissue that is characteristic of skin and muscle wounds have optimal optical properties for NIR wavelengths, specifically that it is weakly absorbed and highly scattered, making it more suitable than visible or UV methods. Near-infrared spectroscopy (NIRS) is a technique which utilises these characteristics by collecting spectral information from strongly absorbing compounds in the NIR region. The two compounds that are used to determine the tissue oxygenation are O_2Hb and HHb, which have peak absorption wavelengths of 760 nm and 900 nm respectively. Water content, which is linked to tissue edema, can also be analysed with a peak absorption of around 980 nm.
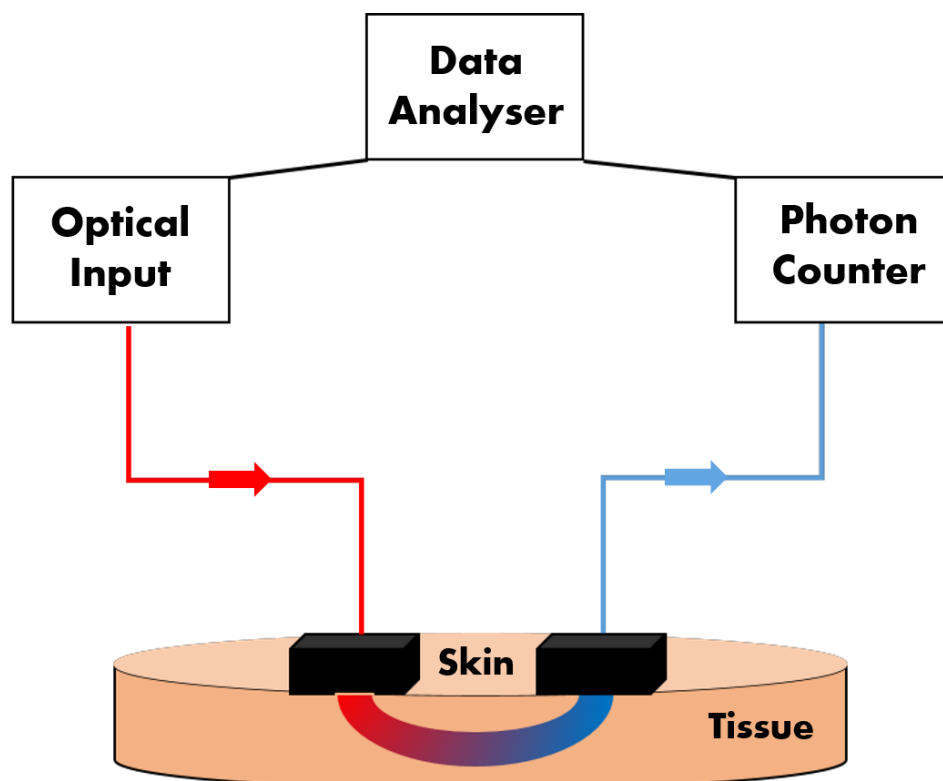
Figure 2.9: A simple near-infrared spectroscopy example.

A simple example of a NIRS set up is shown in Figure 2.9. Briefly, a system of light-emitting diodes (LEDs) or laser diodes are used to illuminate the tissue through the

skin. The light then passes through the tissue, being absorbed, reflected or scattered, with the diffuse reflected signals collected by a CMOS (complementary metal oxide semiconductor) or photodiode detector from the skin surface, which are typically located a few centimetres away from the source. These signals can then be analysed to quantify the concentration of a given compound, such as O_2Hb, HHb and H_2O, which provide further information for a variety of wound types.

Blood perfusion and oxygenation have been measured using NIRS. Discrete wavelengths of light were used to determine these physiological parameters, which can be used as a metric for determining wound severity [66]. Tissue oxygenation has been utilised to differentiate between healing and non-healing wounds in diabetic foot ulcers. 24 wound subjects were imaged over a 4 week period, with an 82% positive prediction of wound healing, highlighting the potential of the technique to predict successful healing, prior to any costly and potentially ineffective treatments [67].

Burn wound assessment is also a key area of research, with the focus upon burn depth classification and tissue edema. As the severity of a burn increases, there is a reduction in circulation, which can be correlated with the levels of HHb, O_2Hb and H_2O. NIRS has been shown to be able to characterise between superficial and full thickness burns, with successful determination of superficial, partial and full thickness burns with the additional edema quantification [68].

Commercially available devices, such as the Kent Imaging device, have been shown to aid in wound assessment for a variety of wound types, through the measurement of oxygen perfusion. This device uses an array of IR emitters to capture data from

large areas of skin (150 cm^2). In an eight second imaging window, it collects a clinical image (conventional photo), as well as an oxygenated and deoxygenated image respectively. Built in algorithms then allow for these images to be overlaid, to display overall tissue oxygenation. This device has been used with diabetic foot ulcers, looking at predicting wound healing dehiscence, skin graft incorporation and gangrenous changes to toes [69].

2.2.5 Perfusion Imaging

Perfusion imaging methods are those that are based on the observation and quantification of how blood flows through tissue, including the heart, skin and muscle. One of the most widely used techniques for perfusion imaging is Laser Doppler Perfusion Imaging (LDI or LDPI). LDI uses the Doppler principle to measure the changes in wavelength of backscattered light from moving erythrocytes within the tissue. A source laser is used to illuminate a region of interest, with the reflected light from both the static tissue and moving red blood cells collected. A schematic image of this is shown in Figure 2.10. The light from the moving erythrocytes experiences a shift in wavelength, either blue or red shifted, depending on the direction of movement. This is then compared with the reflected light for the stationary tissue, which remains at the same wavelength, in order to calculate both blood density and perfusion within the tissue [70].

LDI has been approved by the American Food and Drug Administration as a method to assess the depth of burn tissue [71]. This is used clinically alongside traditional visual assessments, to reduce the decision-making time for skin grafts, and improve the overall treatment of the wound. Although this method is used with a clinician, it has also been shown to accurately predict burn depth independently, with more

accuracy when compared to clinical visual assessment alone [72], although this was only tested upon a small sample type, with further trials needed before it could be implemented without an experienced clinician. LDI has only been applied in a limited manner to other types of wound healing, other than burns, with diabetic ulcers [73], pressure ulcers [74] and scar progression [75]. Historically, this method has also been used to look at wound healing, which focused on the microcirculation of skin flaps, to identify normal wound healing and necrotic tissue [55].

LDI is a method that uses single point illumination, with a scanning mechanism, to measure the whole sample, as shown in Figure 2.6. Another method, laser speckle contrast imaging (LSI or LSCI), can be used to measure a larger 2D surface to image the tissue in full. LSI expands a coherent laser output to illuminate a 2D shape upon the region of interest. The surface imaged contains many irregularities, as the back reflected photons can experience constructive or destructive interference, which creates a speckle pattern. When the measured surface contains moving objects, such as erythrocytes, these speckle patterns contain dynamic information that can be used to calculate blood flow, via image blur analysis.
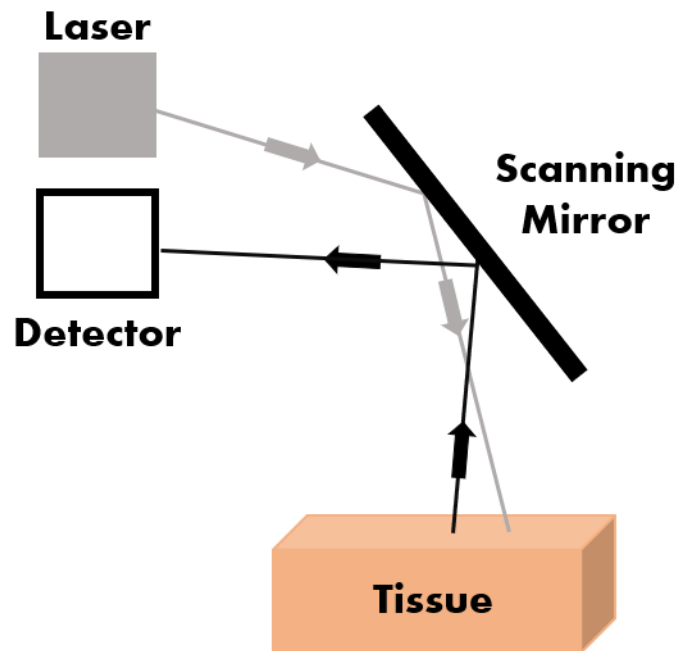
Figure 2.10: Laser Doppler Perfusion Imaging (LDI) schematic. Changes in the wavelength of backscattered light from the moving red blood cells, which are observed due to the Doppler principle, are measured to determine the density and perfusion of blood within the tissue region of interest.

The level of blurring correlates to the blood flow, although LSI is only a qualitative technique, compared to LDI which can be used quantitatively [76]. Similarly to LDI, LSI has been predominately applied to burn wound assessment, where it can identify regions that require grafting in less time than traditional visual inspection methods [77].

2.2.6 Spatial Frequency Domain Imaging

Spatial frequency domain imaging (SFDI) is a form of NIR spectroscopy with a different illumination method. In SFDI, spatially modulated light patterns are projected onto a region of interest in the NIR range. The illumination consists of sinusoidal incoherent monochromatic light patterns at specific frequencies and three different phases. The diffused backscattered light is collected and processed to determine the reflectance at each specific wavelength and spatial frequency. This

is then further separated into absorption and reduced scattering through the use of a light propagation model, including Monte Carlo simulations or diffusion equation approximations [78].

An example of the experimental setup and spatial illumination patterns is shown in Figure 2.11. An illumination source, such as an LED, illuminates a digital micromirror device (DMD) to generate the spatially modulated patterns. This is projected onto a sample of interest, and the backscattered light is collected using a charge coupled device (CCD) camera. These methods then allow for the quantification of tissue parameters, O_2Hb, HHb and H_2O, which are used for the diagnostics of the state of wound healing. SFDI has mainly been used for burn wound imaging and diabetic ulcers, due to its ability to provide depth selectivity, with commercial systems used clinically within the US [79, 80]. Animal models have been used to show that this method can characterise burn wound depths, which is a vital step for wound assessment and appropriate treatment [81]. SFDI allows for the assessment of large areas, when compared the microscopic methods, providing clinicians with a greater ability to predict areas at risk of further damage, via vascular damage spreading, or edema progression [82].
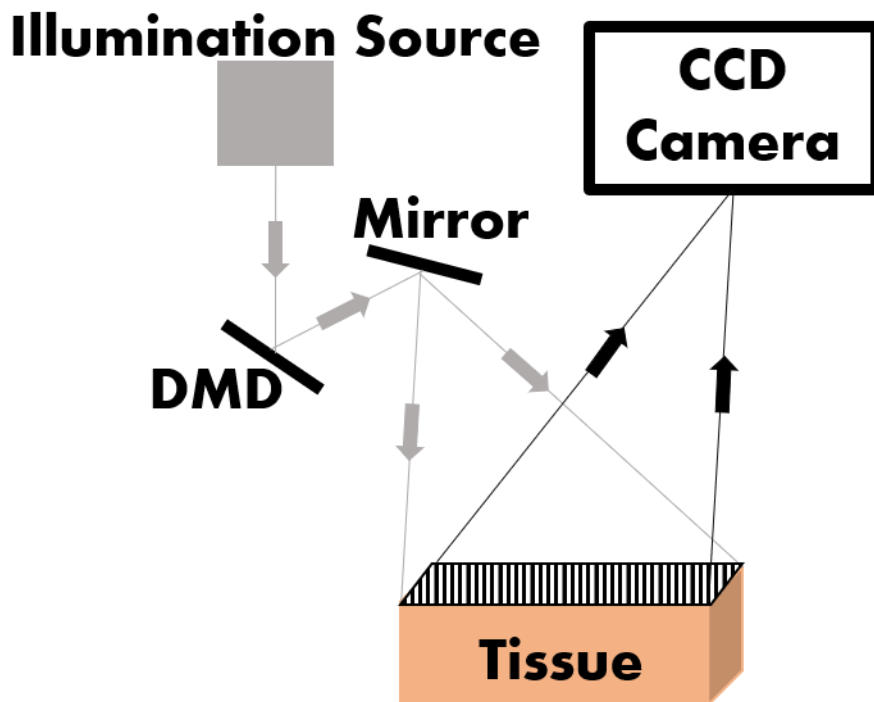
Figure 2.11: Simple SFDI setup

The 2D quantitative maps generated by SFDI have been preliminary trialled for the assessment of surgical cutaneous wounds. Skin flaps cut during surgery can suffer complications from vascular occlusion. SFDI has been used to image these flaps to quantify changes within the wound, allowing clinical intervention before complete tissues loss [83]. More recently, pressure ulcers have also been investigated using this technique. Early detection of these wounds can drastically reduce costs and complications of treatment, and a preliminary study has shown that SFDI can be used to quantify the current wound status of a small sample of patients [84]. Overall, the depth specificity of the technique is its main advantage, while further work is needed to reduce the imaging time whilst maintaining the image resolution.

2.2.7 Optical Coherence Tomography

Optical Coherence Tomography (OCT) is a technique which produces 2D images based on the principal of low-coherence interferometry [85]. Often referred to as

'optical ultrasound', OCT uses NIR light and measures the optically scattered light from the tissue, compared to a reference source. A beam of laser light is split into two optical paths, with once reflected from a reference plate, and one from a sample of interest. These reflected beams then recombine to generate an interference pattern, as shown in Figure 2.12. If the difference in length of the light pathways is equal to the coherence length of the source, the coherence signal is imaged. In general, OCT images tissue with a large field of view (up to 20 x 20 cm^2) [86], generating structural information for larger tissue regions.
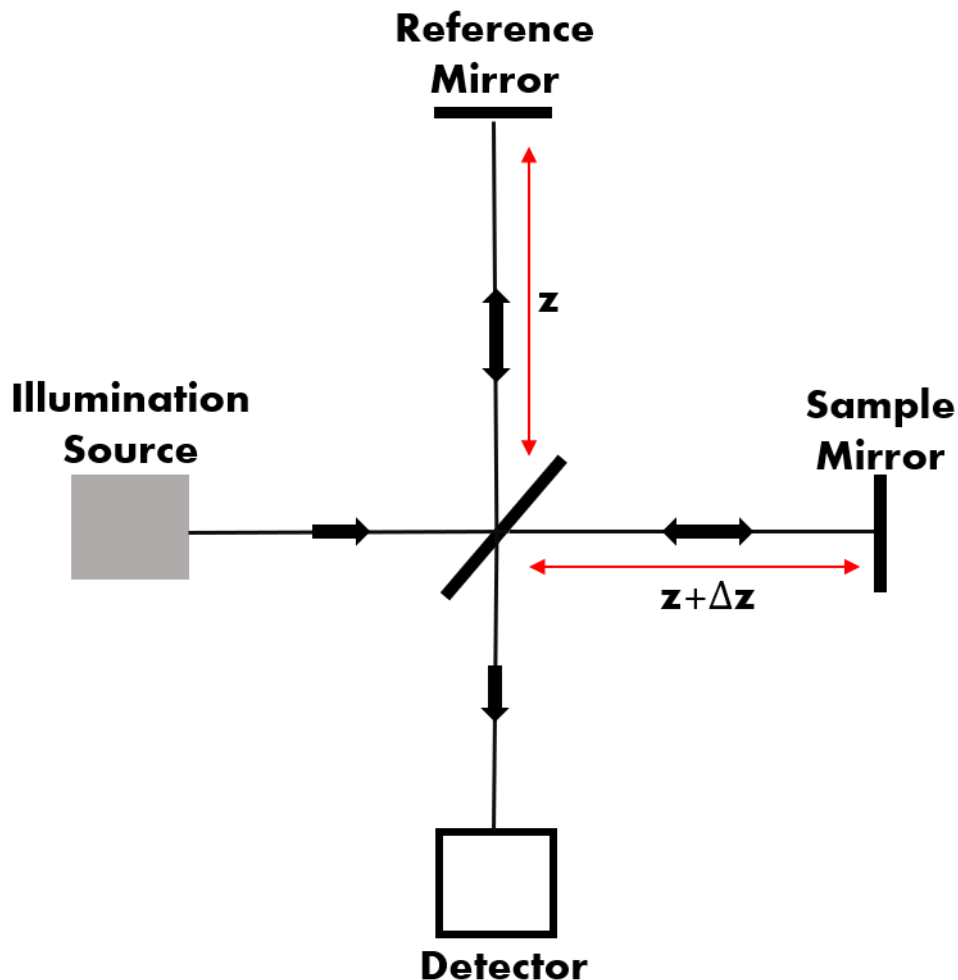
Figure 2.12: OCT schematic set-up.

An additional modification of OCT is the measurement of the light polarization. Polarization sensitive OCT (PS-OCT) measures the changes in the polarization of the illuminated light, which occurs due to materials within the skin, mainly collagen. PS-OCT has been used in the assessment of burn depth, due to the relationship between collagen birefringence and burn severity, which is reduced with increasing wound severity [87]. This method has also been taken one step further with burn depth, as PS-OCT has also been shown to provide information on the microvasculature of burns, which would also be useful in other wound type assessments [88].

OCT has been used to assess *in vivo* wound healing in a small animal study. Cutaneous wounds were induced, and OCT was used to assess structural changes observed during the wound healing process. Through the measurement of the epidermal layer of the skin, the wound healing process can be tracked during the reepithelization phase, whilst also measuring wound size and depth mode, which is made possible by OCT's macroscopic imaging method [89]. Despite these advantages, OCT is limited by only providing structural information, and requires supplementary imaging methods to the provide the key cellular level information needed for the most accurate wound assessment techniques.

2.2.8 Raman Spectroscopy

Although not always an imaging technique, Raman spectroscopy has also been used to investigate healing for a variety of wound types. Raman spectroscopy utilises inelastic scattering of light from a monochromatic source, in the visible, near

infrared or UV range. Laser light interacts with the molecular vibrations of the sample, causing the photons to scatter. These consist of both Rayleigh and Raman scattered light. When the energy of the light is unaffected, the light is Rayleigh scattered, but when altered, this is Raman scattering. The light can both decrease or increase in energy and is known as Stokes or anti-Stokes shift respectively. Figure 2.13 shows a schematic representation of the Raman principle and spectroscopy method.
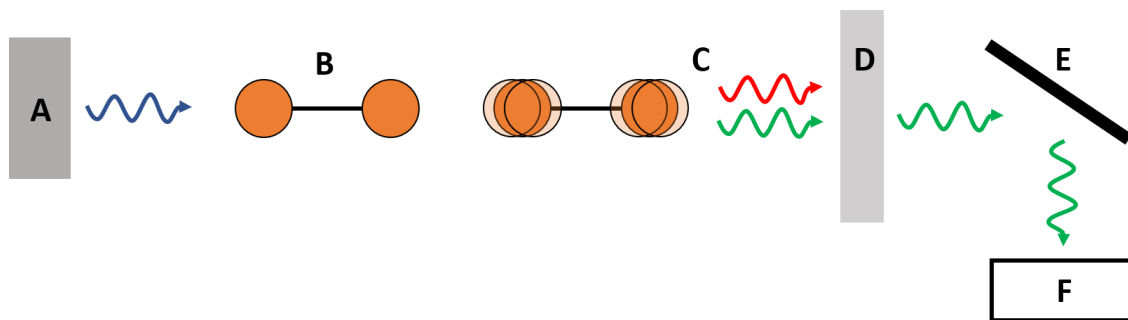
Figure 2.13: Schematic representation of Raman spectroscopy. A: Monochromatic light source in the UV, visible or near-IR range, B: Target molecule within a sample, C: Light is scattered from the molecule and then undergo both Rayleigh and Raman scattering processes, D: A narrow band filter is used to block out the considerably stronger Rayleigh scattering, leaving only the Raman scattered light, E: Diffraction grating used to determine the spectral resolution, F: Detector.

Approximately 10^{-8} of the incident photons are converted to a Raman signal [90], therefore only a weak signal is observed, and considerations for maximising this signal must be made to target specific molecules of interest. One such area is collagen, which plays a key role in wound healing, as discussed in Chapter 1. Gene expression for collagen has been investigated in combat wounds, with 24 samples of both normal and impaired healing measured [90]. Samples of 1 cm^3 were

collected from wound debridement samples before being processed for gene expression analysis. It was found that gene expression for both collagen type I α1 and collagen type III α1 were lower for wounds that experienced impaired healing, compared to those which healed normally [90]. Despite these promising results, this was only a preliminary study and further investigations on a greater number of samples and patients' needs to be performed. Chronic wounds have also been analysed with Raman spectroscopy. Mouse models were used, with full thickness dermal wounds induced at different time points corresponding to the different stages of the wound healing process. Spectral data was collected from each of the samples and analysed using multivariate spectral analysis. Cluster analysis was used to separate the wounds by the healing stage, with outliers identified as those experiencing improper healing [91]. Raman spectroscopy has similarly been used in burn wounds and diabetic foot ulcers [92, 93].

Although Raman spectroscopy has provided positive results for a variety of wound types, the low signal presents a couple of key issues. The first is that the instrumentation needed to detect this signal needs to be sensitive and optimised, and current methods are limited to lab-based studies. Secondly, the weak signal is reduced further by any contamination, and combat and blast injuries suffer this in greater amounts compared with other wound types. Finally, heating from over exposure of the laser, when trying to maximise the signal detected, can cause the sample to heat, damage and even cover the Raman spectrum completely.

2.2.9 Negative Contrast Imaging

One final technique that has been used to investigate the wound healing field is a negative contrast imaging (NCI) device. This NCI device, developed by M Squared

Lasers (West of Scotland Science Park, Glasgow, UK), is a reflectance imaging device that collects hyperspectral images from illumination in both the SWIR and MWIR spectral regions. The device has been used previously to identify spectral differences between wound biopsies, with 7 human samples imaged to predict the wound healing outcome [94], along with chemical detection applications [95, 96]. This device is made up of an optical parametric oscillator as its SWIR/MWIR (1.5 – 1.9 μm and 2.4 – 3.8 μm) photon source along with an image acquisition system containing a Mercury Cadmium Telluride (MCT) detector. The generated images are the result of the back reflected light collected for each pixel, up to a 512 by 512 image resolution. Each hyperspectral data cube consists of images collected between a user specified wavelength range, with a resolution of up to 2 nm. Spectral changes were observed between samples that underwent correct healing, compared to those that dehisced or showed delayed healing. This spectral change was observed in the 3100 nm wavelength region, related to changes in common chemical bonds, such as C-C and C-H, and was initially identified using Fourier Transform Infrared (FTIR) microspectroscopy. This brief proof-of-concept study extended the wavelengths of investigation beyond the NIR region, with the ability to detect multiple chemical and biological changes within a unique spectral fingerprint.

The NCI device is not commercially available, with the limited sample study representing the first application in biomedical imaging. The NCI device maturity can be described through technology readiness levels (TRLs), which are a measure for assessing an emerging technology, developed by NASA during the 1970s [97]. The NCI has reached a TRL of 3-4, with the next stage of development requiring further investment, which is currently not in place. TRLs are not reached via a linear cost

relationship, with the development costs at approximately 13% for reaching TRL 4, compared with the full cost of a TRL 9 system [98], therefore significant investment would be required to advance the NCI technology further along the developmental timeline.

2.3 Intelligent Data Analysis

The aim of the methods discussed in section 2.2 is to provide additional information, which is not obtainable via simple observation, to aid clinicians in the wound assessment process. However, even with this additional information, the subjectivity of individual medical and clinical staff analysing the data can still occur. For example, the fluorescence imaging shown in Figure 2.6 utilises a handheld imaging device to identify the areas of chronic wound infection via endogenous autofluorescence [59]. Whilst this method provides clearer images of the boundaries in real time, the gradient across the wound boundary must still be assessed and created by visual observation, producing room for subjective analysis. Similarly, the resulting spectra for FTIR imaging in section 2.2.9 still requires the visual assessment of the obtained reflectance spectra to separate out the different wound healing pathologies for diagnostic purposes, whilst also unable to identify one third of the healthy wounds [94]. Additional processing and analysis of data obtained from these wound assessment methodologies can therefore aid in this processing, providing even more information to aid in point-of-care wound assessment to reduce or even remove any potential subjectivity of a clinician's assessment.

These data analysis methods can be split into two main parts: pre-processing and intelligent analysis. Data pre-processing aims to deal with any problems with the data, such as missing or noisy data, whilst also optimising any information within to

aid in the data analysis processing. The data analysis then extracts this information for a variety of uses such as prediction and diagnosis, as is with the cases of wound healing assessment [99].

2.3.1 Data pre-processing

Data pre-processing for wound assessment covers a wide range of methodologies. Simple ordering and editing can help remove unwanted data and repeated data, removing any bias from experimental error or the extraction of relevant data from a larger data set. For example, the removal of pixels to separate out a specific region of interest, whilst selecting a specific subset of a full sweep region can reduce the processing time [100].

Noise reduction and filtering of data represents another large area of pre-processing methodologies. Noise can be attributed to data from a variety of experimental sources such as amplifiers, analogue-to-digital conversions or external sources [101]. Median filtering, alongside adaptions of this technique such as adaptive median filtering, are common place in both single wavelength images and spectral methods, reducing the effect of noise in both cases before the data analysis stage [102, 103]. Additional filters can also be applied in isolation or combination of the above to correct, homogenous or equalise specific wavelengths of an image or spectra [104-106].

Spectral derivatives and normalisation are also used as common pre-processing steps within spectral analysis. These steps aim to extract any key features within the data, whilst also improving signal to noise ratios. First and second spectral

derivatives are the most used, with normalisation proceeding to allow comparison
between different samples containing varying noise [107, 108].
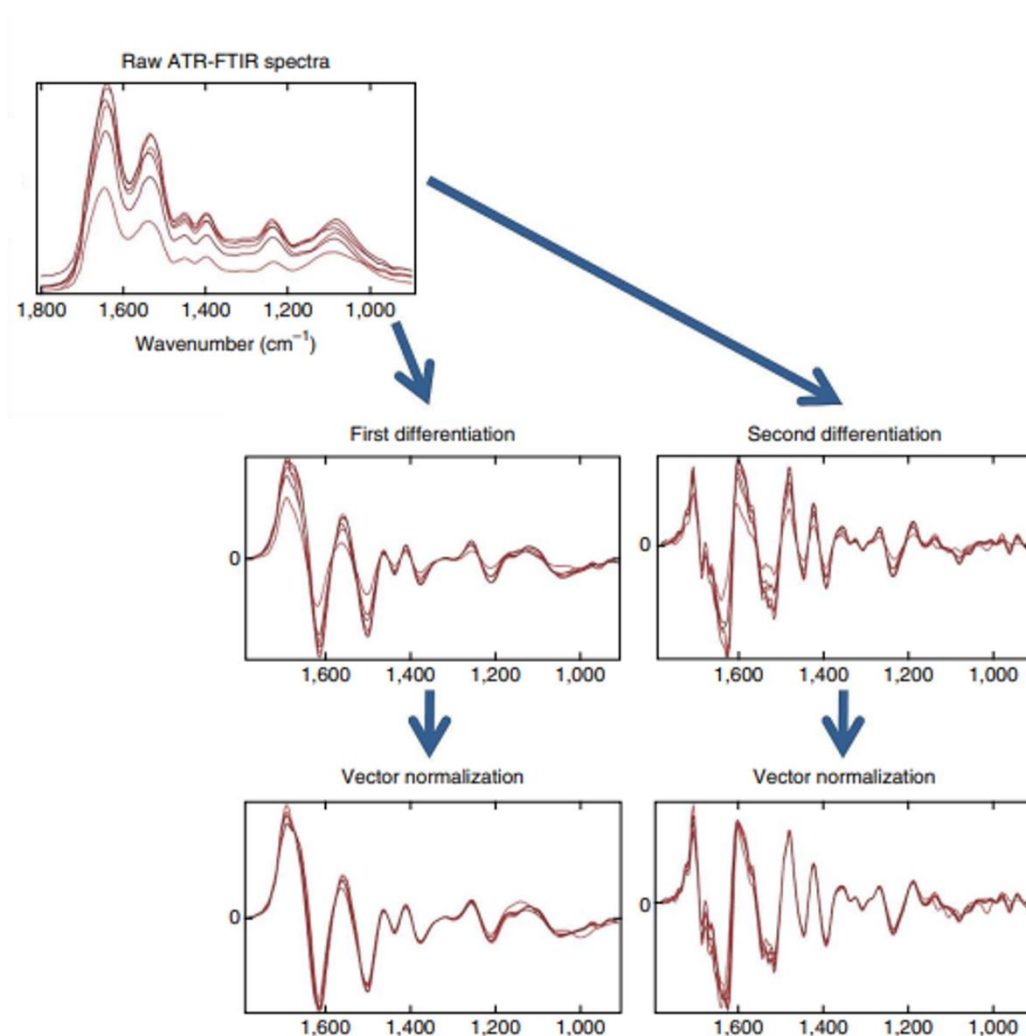
Figure 2.14: Spectral derivative and vector normalisation. A common spectral analysis pre-processing method takes the first or second spectral derivative of the raw signal before performing vector normalisation, allowing for comparison across large data sets. Adapted from [109]

A final pre-processing method to note is data reduction. Often, spectral data can be
remapped to a different space in which the key features can be extracted, and noise
or unwanted data can be removed. These methods include principal component
analysis (PCA) and singular value decomposition (SVD), which both use linear

dimensional reduction and are used in wound assessment methodologies [110], including those for diabetic foot ulcers and burns [111, 112].

2.3.2 Data analysis methods

The pre-processing and feature extraction methods discussed in the previous section are undertaken for specific data analysis methods, to improve the outcome of the process. The data analysis methods aim to group or classify similar samples, which for the case of wound healing, assist or undertake fully, the processes of assessment or diagnosis. The optimised data sets can then undergo machine learning processing of varying methods to generate the result. These methods can be broadly split into three classes: clustering, classification and neural networks.

Clustering

Clustering methods are a form of unsupervised machine learning, in which the data is group into clustering using a similarity parameter. As an unsupervised technique, these methods do not require any *a priori* information about each sample's origin. Clustering methods, such as k-means and hierarchical clustering are commonly used for spectral data to group similar spectra for wound assessment purposes [113-115].

A further clustering method, known a fuzzy c-means has been used to cluster pixels of diabetic ulcers, similar to those seen in Figure 2.6. Like k-means, each data point is however assigned a 'weighting' to all clusters, create a soft linkage to each cluster, compared to the hard assignment of k-means [116]. Using the mean Euclidian distance metric, an accuracy of up to 99% was achieved in identifying different tissue types [117]

Classification

If *a priori* information is used, the methods become supervised learning techniques and can be broadly determined as classifiers. Classifiers split the data into training, testing and often validation subsets, therefore meaning more data is generally required than used in some clustering methods. The data also requires labelling by a trained clinician or expert to build the classifier initially.

Many different classification tools exist for the wound imaging and spectra assessment and analysis. These include linear discriminant analysis (LDA), support vector machines (SVM), k-nearest neighbours (KNN), Bayesian classifiers and neural networks, which will be discussed further in the next subsection [65, 118, 119]. The decision to use any of these methods is based on data availability, ease of training and computational time [109]. In the field of burn wound assessment, SVMs have been used to analysis NIRS data which has also undergone data reduction via PCA. The method identified different microbial species within the wound bed to detect levels of infection, with up to a 100% detection rate [120].

Neural Networks

A final subset of classifiers commonly used in wound assessment is neural networks. These methods are more prevalent with the increase of eHealth medicine, and have been applied to a variety of wound types [121]. A neural network contains an input and output layer, with a series of neurons in which the original data is acted upon with via a specific function. Each layer then outputs to the next via series of weightings. These are defined as self-learning methods which model human neurons and synapses. An example of these methods is using feedforward neural networks for detection. A five-layered feedforward neural network was design to

perform wound segmentation and detection upon chronic wounds. These networks were optimised to handle varying input images to improve the overall robustness.

Overall, the intelligent data analysis methods discussed aim to reduce the reliance upon trained and experienced clinicians to perform individual diagnosis and assessment across a variety of different wound types. These methods help process the additional information obtained from the wound imaging and spectroscopy methods discussed in 2.2.

2.4 Conclusion

The imaging modalities described above are at the cutting edge of current wound assessment research. The most common wound type for assessment is burns, which could be for a variety of reasons. Burns are which have easily definable grades of severity, which can be produced repeatably in both *in vivo* and *ex vivo* samples [122]. The severity of the wound can be independently classified via the wound histology, providing a ground truth for modalities to be compared with. Quantification of the accuracy of these methods can then be made, and easily compared with current best practise clinical methods, as well as other novel methods currently in development. Burn wounds are also common across all ages, sexes, and races, and are experienced worldwide, with little difference between wound characteristics for burns of the same severity. Overall, burns experience many issues that are common in all wound types, vascularisation problems, necrosis, edema and infection, making them a suitable model for generic wound assessment. A summary table of the different wound assessment techniques discussed, along with the wound types they have been applied to is shown in Table 2.1.

Imaging Modality	Wound Type
Photography	*Burn [123]*
	Pressure Ulcer [45]
Thermography	*Burns [50-53]*
	Diabetic Ulcers[55]
	Skin Flap [56]
Fluorescence	*Burn [57, 58]*
	Transplant [60]
Multi- and Hyperspectral	*Burn [4, 63]*
	Skin Lesions [60]
Near-Infrared Spectroscopy	*Burn [68, 69]*
	Diabetic Ulcers [66, 67]
Spatial Frequency Domain Imaging	*Burn [81, 82, 124]*
	Skin Flap [83]
Perfusion Imaging	*Burn [71, 72, 77]*
	Diabetic Ulcers [73]
	Pressure Ulcers [74]
	Scar Progression [75]
Optical Coherence Tomography	*Burn [87] [88]*
	Cutaneous [89]
Raman Spectroscopy	*Blast [125]*
	Burn [92]
	Chronic [91]
	Diabetic Ulcers [93]
Negative Contrast Imaging	*Blast [94, 126, 127]*

Table 2.1: Summary table of non-invasive wound assessment methods

Whilst these methods represent some of the latest advancements in wound assessment, there are a few common areas in which they are limited. Despite the

success of many studies, the gold standard wound healing assessment remains visual observation. Although many of the methods offer additional visual information, such as pseudo colour images [128], these ultimately still require interpretation by a trained expert, resulting in the subjectivity of the method and any resulting assessment or diagnosis. Whilst some methods of intelligent data analysis, as discussed in section 2.3, there is a clinical need for a robust imaging modality that provides both quantitative information for the assessment of different wound healing parameters and complimentary analysis tools based on computational methods, removing the subjectivity of current methods.

Additionally, these methods have been focused within the visual and NIR regions, with limited work performed beyond this. Whilst the clear benefits of imaging within this region have been discussed in section 2.1.3, additional information regarding further wound healing facets exists within the SWIR-MWIR range [127], with further discussion of the particular spectral regions and parameters of interest to come in the following chapter. The remainder of this thesis will discuss work made to further the field in these two areas of interest.

Chapter 3

3 Intelligent data analysis

Within this chapter, novel data analysis methods are applied to previously obtained FTIR results [94]. As discussed in section 2.3, intelligent pre-processing and analysis methods can be used to extract additional information for assessment and diagnosis of wounds. An initial study at Dstl, in collaboration with the Naval Medical Research Center (NMRC), Bethesda, Maryland, USA, investigated the spectral differences between different wound biopsies using both FTIR and NCI methods in the IR region. Whilst visible differences were identified between the seven samples measured, and key spectral regions for discrimination between three different wound states: healed, delayed and dehisced, were identified, these were only discovered through detailed visual observation of the spectra, which is a laborious process and unsuitable for larger data sets. In this chapter, work to create a machine learning based robust methodology for spectral differentiation is presented and applied to the existing FTIR wound biopsy data. The material for this chapter is based upon work presented at the Photonics West Conference 2019 'Mid-infrared spectroscopic imaging to assess wounded tissue health'.

3.1 Introduction

Wound healing assessment and management are both important in ensuring a correct healing sequence. The majority of these assessment techniques involve simple observation with the naked eye, which has two main drawbacks: the parameters assessed are highly subjective, and interpretation relies upon the

knowledge and experience of trained medical professionals. Any failure in wound assessment or incorrect management can result in further complications and even fatality [2], therefore quantitative and more objective techniques are the next step to a more accessible and reliable wound management strategy. Previously, seven different wound samples (waste material from serial debridement's of US military personnel injured in Afghanistan) were characterised using Raman spectroscopy [129, 130]. These samples were also subjected to FTIR to identify key spectral regions for discrimination between three different wound states: healed, delayed and dehisced. Healed wounds were defined as those that definitively closed within the thirty-day window post injury. Delayed wounds are those that exhibited definitive wound closure two standard deviations away from the regular wound healing closure time window. Finally, dehisced wounds were defined as those that ruptured following surgical intervention, re-opening the wound.

The FTIR data from this study exhibited differences in the spectra for two of the three healed results within the 3400-3000 cm^{-1} spectral region, when compared with all other spectra. However, these differences were only discovered through detailed visual observation of the spectra, which is a laborious process and unsuitable for larger data sets. For 'big data' a variety of machine learning and computational techniques can be used to separate data sets, providing labels for different subsets and grouping similar data together. These techniques, along with data reduction methods can detect differences in large data sets using computational algorithms. For instance, this approach can provide a robust method for distinguishing between the different pathological outcomes observed in the previous study [94], by

attempting to extract features within the data that may not be obvious in the simple plotted spectra.

In the present study, clustering was observed using both raw data and data that had been dimensionally reduced using principal component analysis when using an unsupervised computational algorithm. Separation of data into regular/irregular healing and the three different pathological outcomes was then investigated to provide more objective wound assessment.

3.2 Methods

3.2.1 Clinical Biopsies

The clinical data, collected as part of a previous study [94], from the wound biopsies were performed under the review boards of the NMRC and the Walter Reed National Military Center. Patients for this study were all over 18 years old and had experienced high-energy combat-related traumatic injuries. Informed consent was provided prior to biopsy collection for all participants. The wounds for this study all had an Injury Severity Score greater than or equal to 9 and a wound surface area of greater than 75 cm^2 or a traumatic amputation with an open wound [131]. During surgical wound debridement, biopsies of approximately 1 cm^3 were collected from the wound bed, every 48 to 72 hours. Following collection, the biopsies were fixed in 10% neutral buffered formalin. These were then stored at 4 °C until use. Finally, the wound closure time point was determined by the attending surgeon.

3.2.2 Fourier Transform Infrared Spectroscopy of Wound Biopsies

FTIR microspectroscopy of the seven different wound samples was performed using a Bruker Optics LUMOS FTIR microscope, which comprises a liquid nitrogen cooled

Mercury Cadmium Telluride (MCT) detector along with a ZnSe beam splitter. The samples were mounted to an aluminium coated mirror slide, which was then placed upon a motorized x-y stage attached to the interferometer. For each sample, a minimum of nine FTIR spectra were collected from different locations (Figure 3.1) with a sampling aperture size of 120 x 120 μm. Each single-point spectrum consisted of an average of 32 scans with a spectral resolution of 4 cm^{-1} in the spectral region 650-4000 cm^{-1} (2.5-15.4 μm). Background scans from a region containing no sample were also taken and normalized against each sample spectrum.
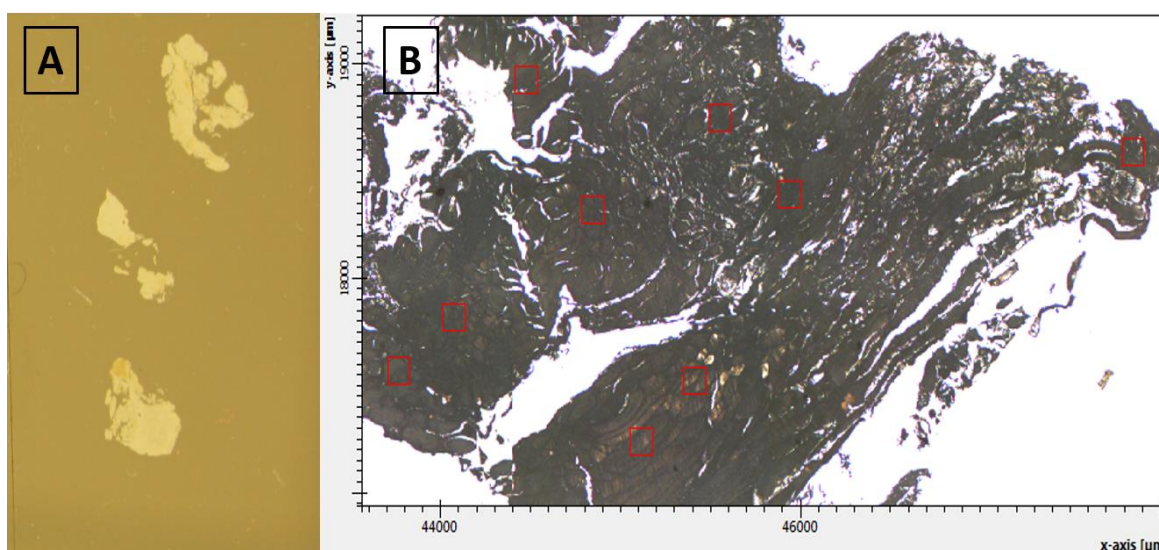
Figure 3.1: Wound biopsy and FTIR map. A: Example photograph of the formalin-fixed tissue biopsies from different debridement's of a typical wound. B: Tissue biopsy image from the FTIR collection. Spectra were collected from multiple locations on each section sample (red boxes) which are 120 x 120 μm.

3.2.3 Fourier Transform Infrared Spectroscopy Spectral Difference

In a previous study [94], visual representation of the seven different spectra exhibited a difference at approximately 3200 cm^{-1}. Figure 3.2 A shows the mean spectra from each of the wound samples, which has been baseline corrected using a 15-point linear interpolation and normalised to the amine I peak. These differences

are highlighted further when the vector normalised 1st derivative of each wound sample spectra is considered. These whole spectra are shown in Figure 3.2 B, with the key region-of-interest shown in Figure 3.2 D. However, these differences are only visible in wounds A and B, with the third healed wound, wound C, exhibiting similar results to the delayed and dehisced wounds.
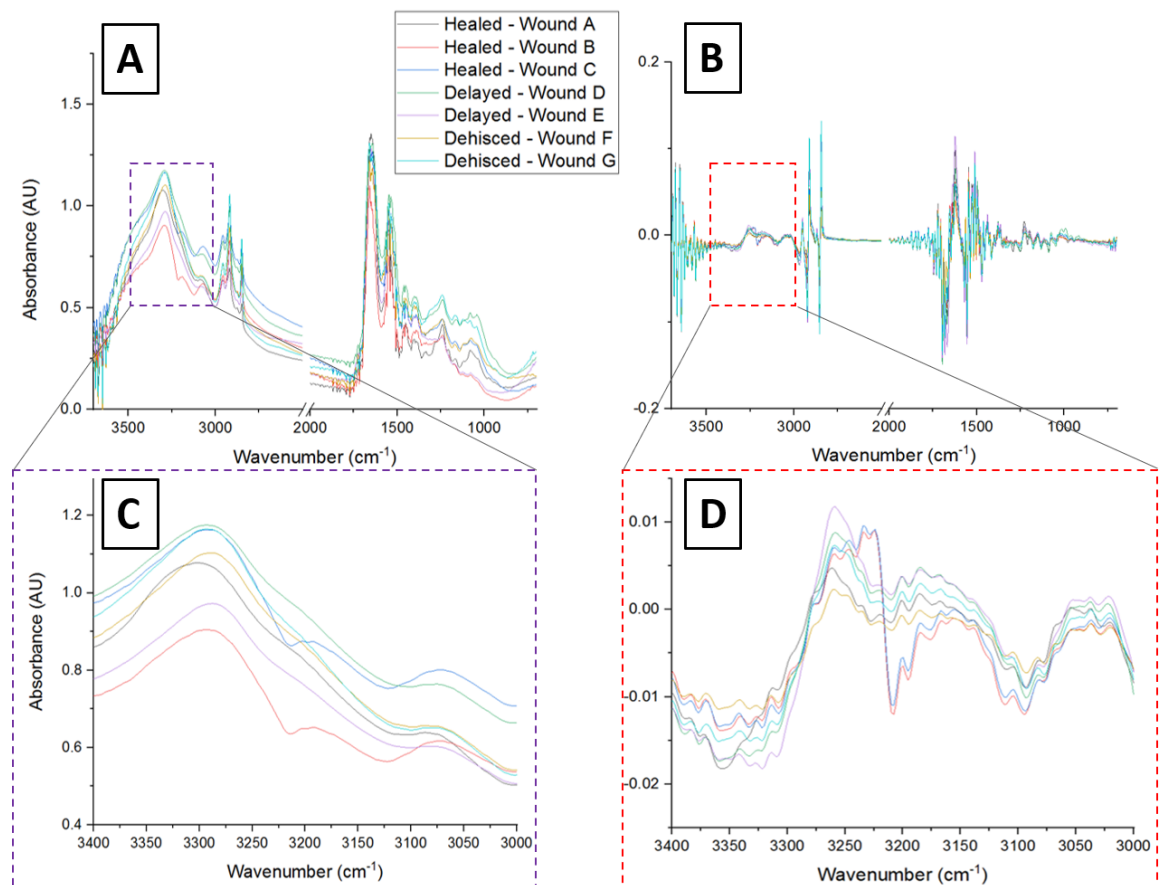
Figure 3.2 FTIR spectral panel. A: FTIR spectra collected from each of the seven different wound tissue samples. Each spectrum consists of the mean value from the different locations, as shown in Figure 3.1. These values are then baseline corrected using a 15-point interpolated linear baseline and normalised to the intensity of the amide I peak. B: Vector normalised 1st derivative spectra of the FTIR spectra. C: An expanded region detailing a spectral region of interest with key differences between the majority of healed spectra. D: Same wavenumber region of the vector normalised spectra with a clear visual difference between two of the three healed wound tissue samples.

3.2.4 K-means clustering

K-means clustering is a method of unsupervised machine learning, which has been applied to a variety of biomedical applications [132]. Typically, supervised classification methods, such as convolutional neural networks, are used. However, these methods require larger sample numbers in excess of 1000, allowing some data to be used as training sets with pre-labelled outcomes to train classifiers [133]. The aim of the k-means algorithm is to take unlabelled data and group them into k clusters, which exhibit similar properties. This method can be used with FTIR data with the aim of grouping different spectra into clusters [109].

An example of the k-means clustering algorithm used is outlined in Figure 3.3, which is a 2D data set containing 6 data points represented by crosses. Using a pre-defined number of clusters, k = 3, cluster centroids were randomly assigned within the 2D space, shown as circles of three different colours. Each data point was then assigned to its nearest cluster centroid completing the first iteration. The centroid means were recalculated using the mean value for each dimension from the data points assigned to it, shown as the centroid relocation step. This process was repeated until convergence, which can be defined as either a set number of iterations, or the point at which no data points change cluster following centroid relocation.
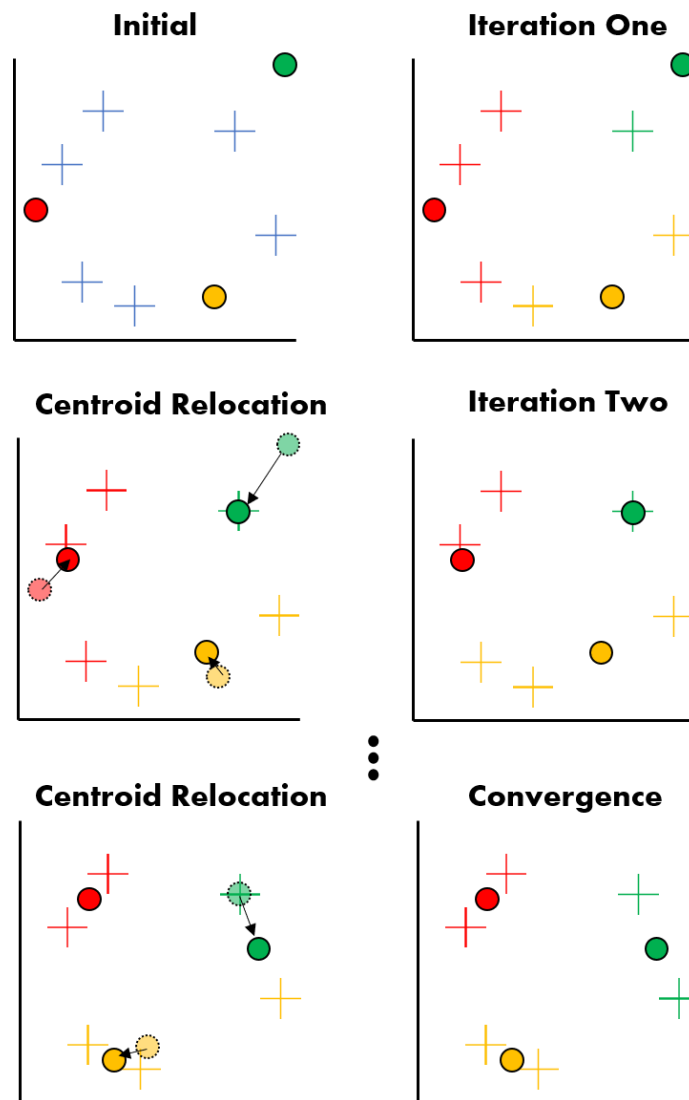
Figure 3.3: k-means clustering. Simple 2D k-means clustering example for k = 3 clusters upon 6 data points. Three cluster centroids (Circles) are initiated at random, and the data points (Crosses) are assigned to their nearest centroid in the first iteration. The cluster centroids are then relocated, before the point assignment is repeated in the next iteration. This process is repeated until convergence, defined as either a set number of iterations, or when no points change cluster assignment.

With three different pathological outcomes observed across the seven samples, clustering with k = 2, to differentiate regular and disrupted healing, and k = 3, to differentiate the different outcomes, were investigated. Using the full FTIR spectra, the dimensionality of the data is 1667 and the cosine similarity metric was utilised to measure the data point to centroid distance. Due to the random nature of the cluster centroid locations, the clustering algorithm was repeated to find the modal

cluster, and its frequency reported as the modal cluster frequency in subsequent results.

3.2.5 Principal Component Analysis

Principal component analysis (PCA) is a dimensionality reduction technique used on large data sets with minimum data loss and has been applied to FTIR spectra previously, to aid in clustering and classification [134]. PCA reduces this data into a lower number of dimensions, known as principal components (PCs), which are output in decreasing order of variance and are linearly uncorrelated. In order to determine the PCs of a data set, first the covariance matrix, C_x, is calculated by transforming the normalised original data matrix such that their covariance is represented within a diagonal matrix:

$$C_x = \frac{1}{n-1}(X - \overline{X})(X - \overline{X})^T \qquad (3.1)$$

where X is the m × n original data matrix, m is the number of measurement types, n the number of samples and where each column of $\overline{X}$ is a mean value of X. From this, the eigenvalues and eigenvectors are calculated and sorted from largest to smallest based on their eigenvalues. This creates an m × m matrix whose rows each represent a value along a given PC.

This linear transformation projects the data onto a new coordinate system, where the greatest variance within the data is exhibited across the first coordinate system PC1, second over PC2, etc. A schematic example is shown within Figure 3.4, where a set of data points, represented in two dimensions can be processed using PCA, and the new PCA dimensional axis can be used to represent the data, with the

maximum variance of the data shown along PCA dimension 1, and the orthogonal

axis representing the 2nd PCA dimension.
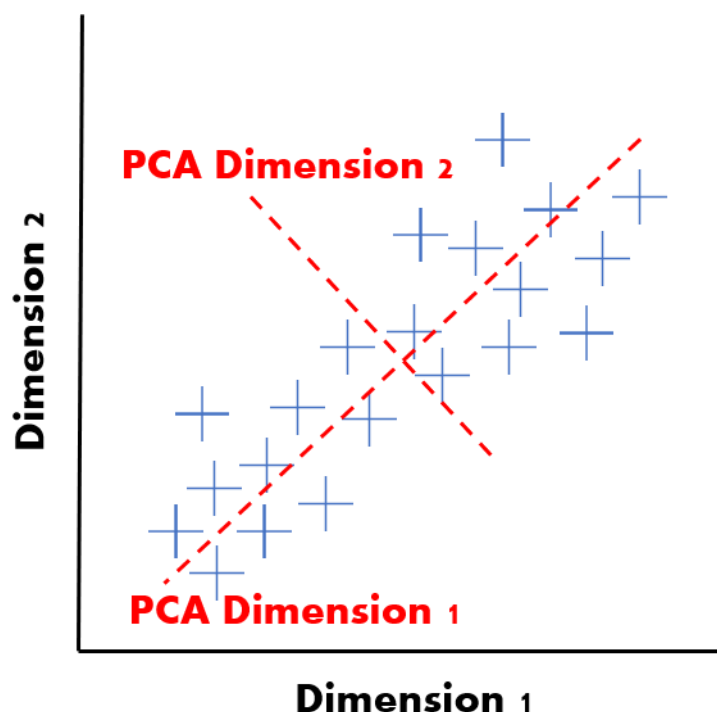
Figure 3.4: Principal Component Analysis Example. Simple 2D PCA example for a collection of data points. Using PCA, the data can be projected onto new dimensions, PCA Dimension 1 and 2, which represent the greatest variance within the original data.

Although each of these PCs does not represent a physical value, such as a given

intensity at a specific wavenumber, it separates the data to find the maximum

variance, allowing for any hidden distinguishing features to be extracted. PCA is

used as a pre-clustering step, aiming to reduce the 1667-dimensional full spectra

data. Following this dimensional reduction, the PCs which corresponded to >95% of

the variance were selected, with k-means clustering then applied to the reduced

data set, as described in 3.2.4. The combination of k-means clustering and PCA is

suitable for the low sample numbers within this study and is common in biological

spectral analysis [135, 136].

3.3 Results and Discussion

3.3.1 K-means clustering optimisation

K-means clustering is an unsupervised learning algorithm that aims to collect similar data into k groups. The initiation of this algorithm uses a random cluster centroid, meaning the start location for each cluster will vary each time the algorithm is ran, potentially producing different final cluster, so repeat runs of the clustering are required to collect the optimal outcome. In order to quantify this parameter, the modal clustering method is used. The modal cluster is defined as the highest occurring clustering outcome across a series of algorithm repeats, with its frequency also used for optimisation. This frequency, at which the modal cluster occurred, was recorded for an increasing number of clustering repeats. The optimal number of clustering repeats was defined by the modal frequency varying by <0.5%, which occurred at 10,000 repeats for both 2 and 3 clustering groups (Figure 3.5). This figure depicts the modal cluster frequency for both the 2 cluster (red line and left-hand y axis) and 3 cluster (blue line and right-hand y axis). At lower numbers of repeats, the modal clustering frequency varies greatly, showing the data is dependent on the initial clustering values. The larger number of repeats appears to stabilise this result, confirming the modal cluster.
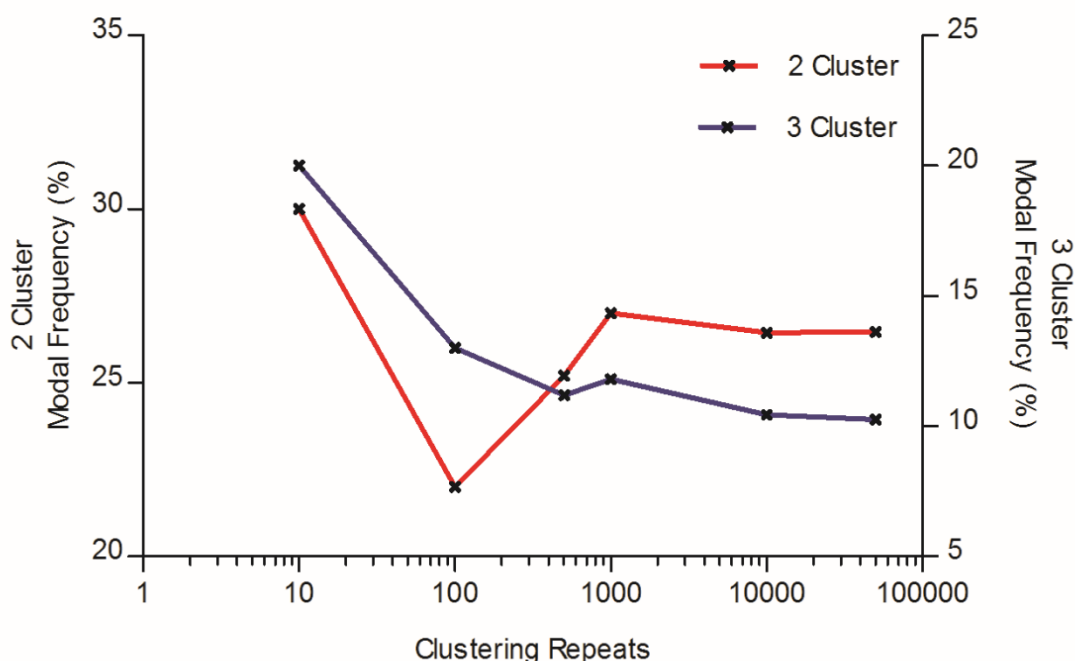
Figure 3.5: k-means optimisation. Due to the random initiation of clusters in the k-means algorithm, repeats are required to improve the accuracy of the result. The optimal clustering repeat number was determined when the frequency of the modal cluster varied by <0.5%, which occurred at 10,000 repeats for both 2 and 3 initial clusters.

3.3.2 Data selection

Figure 3.2 shows the full spectral results of both the absorbance spectral data and the vector-normalised 1st derivative (VN1D) data. Both data sets, along with the PCA data from the VN1D spectra, were subjected to the k-means clustering algorithm in order to cluster the spectra into different pathological outcomes. Initially, an investigation into the separation of the data into two clusters, regular and irregular wound healing, denoted as green and red in Table 3.1 was performed. For each data set, the modal cluster is shown, and compared to the ground truth pathological outcome as determined by the attending surgeon. The frequency at which the modal cluster occurred within the 10,000 repeats is also shown. This process was then

repeated for the k=3 models, with green, yellow, and red colours denoting the regular healing, delayed and dehisced data respectively.

3.3.3 K-means clustering

Two cluster analysis

The simple absorbance data produced a modal clustering which contained both false negatives and positives, and a low model clustering frequency of only 16.14%. An improvement was observed when the VN1D data was analysed with an increase in the modal clustering frequency and a reduced number of false negatives; however, a much greater improvement was made when PCA is applied to this data.

Clustering of this data set produced a 97.51% modal cluster which correctly clustered two of the three healed wounds, observed in Figure 3.2 B and D. The use of the whole data set also produced an improved modal clustering than the reduced data set containing the FTIR spectra from 3500-3000 cm^{-1}, suggesting additional discriminative information lies outside of this observed region of interest.

Data Set	Modal Wound Cluster							Modal Cluster Frequency
Ground Truth	A	B	C	D	E	F	G	N/A
Absorbance	red	green	green	green	green	red	red	16.14%
Vector-normalised 1st derivative	red	green	green	red	red	green	red	26.69%
PCA of VN 1st derivative	red	green	green	red	red	red	red	97.13%
PCA of VN 1st derivative (3500-3000 cm^{-1})	red	green	green	red	red	red	red	95.51%

Table 3.1: k-means results for k = 2 clusters. Regular healed wounds are denoted in 'green', while irregular healed wounds (delayed and dehisced) are denoted in 'red'. Following 10,000 repeats of the clustering algorithm, the modal cluster and modal clustering frequency for different data sets are shown.

68

Three cluster analysis

Although the two-class clustering provided an accurate method for detecting two of the three healed wounds, without the need for human spectral assessment, three class clustering could detect and cluster the three different pathological outcomes observed within the biopsy data set. The results for k=2 clustering demonstrated the presence of additional information within the full spectral region obtained by the FTIR, therefore only the three full spectra data sets were analysed with three-class clustering, with the results shown in Table 3.2. The PCA data from the VN1D spectra accurately clustered the three healed samples correctly but produced a false positive result for wound sample G, which clustered as a delayed sample. This modal cluster was also seen in the VN1D data set alone, but with a lower modal clustering.

Data Set	Modal Wound Cluster							Modal Cluster Frequency
Ground Truth	A	B	C	D	E	F	G	N/A
Absorbance								8.32%
Vector-normalised 1st derivative								10.02%
PCA of VN 1st derivative								68.5%

Table 3.2: k-means clustering results for k=3 clusters Regular healed wounds are denoted in 'green', while delayed wounds are shown as 'yellow' and dehisced are denoted in 'red'. Following 10,000 repeats of the clustering algorithm, the modal cluster and modal clustering frequency for different data sets are shown.

The seven different wound samples can be visualised in their respective clusters by displaying the data along the first two principal components (Figure 3.6). Although this clustering does not accurately group all the biopsies, the three wounds that healed regularly were separated successfully.
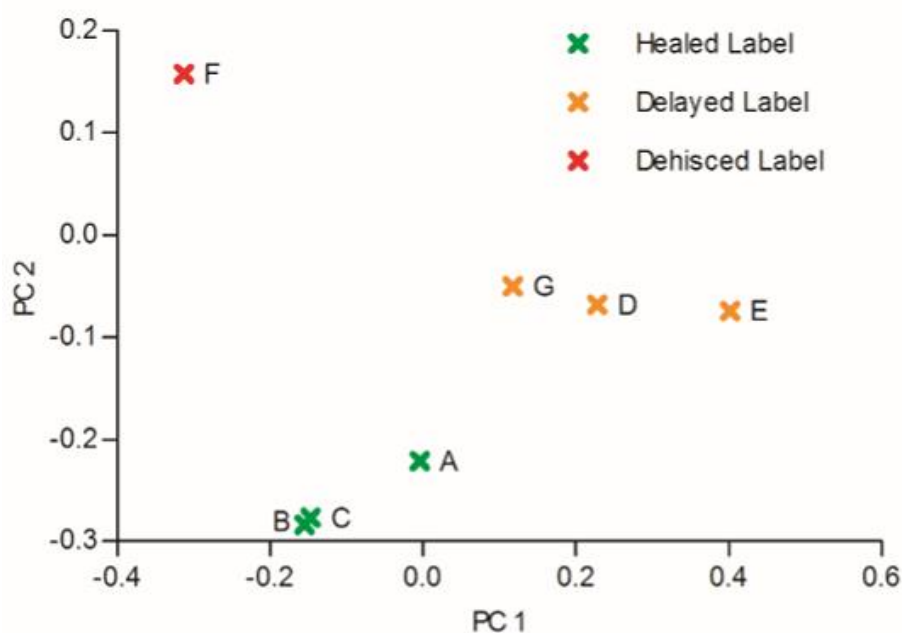
Figure 3.6: Three cluster PCA visualisation. Following the application of principal component analysis to the vector normalised 1st derivative data, the seven different wound samples are clustered into three separate groups, corresponding to the difference pathological outcomes. Only wound G is incorrectly clustered when comparted to the ground truth labels. This cluster was observed as the modal cluster with a frequency of 68.5%.

3.4 Conclusion

Seven wound biopsies taken from blast injuries were analysed using FTIR microscopy in the mid-infrared region. Visual inspection of a key region, 3500-3000 cm^{-1}, showed spectral differences for two of three samples which observed regular healing. However, the third healed biopsy, along with the others which observed delayed and dehisced healing were indistinguishable, and manual inspection of spectra is not suitable for a larger data set. Clustering, via the k-means algorithm, was applied to the spectra, along with principal component analysis, a dimensionality reduction technique. These machine learning techniques were applied to group similar spectra for diagnostic purposes. With two clusters, the same result occurred, with two of three healed samples being identifiable. With three

clusters, following the application of PCA, the three healed wound samples were separated from the others in the modal cluster, demonstrating the ability of intelligent data analysis methods using dimensional reduction and ML based methods for improving diagnostics. However, the two other pathological outcomes were not fully matched correctly. Additionally, with only seven samples examined, classification methods were not suitable due to a lack of training data, and the reliability of the clustering methods described would need to be tested further. Despite our best efforts, additional samples were not available due to reasons beyond our control. Nevertheless, the work has shown a possible method for discrimination and clustering of FTIR spectra, which is not reliant upon a subjective clinical diagnosis. Alongside this, clinical colleagues have identified the essential need for non-invasive non-contact imaging methods for guided wound debridement which can be seamlessly integrated into the field. Future work will focus upon control of the levels of trauma each sample receives through lab-based trauma inducing experimental methods for cellular studies and performing a larger study to increase the sample size. Investigations into wound relevant cell cultures will look at spectral changes between healthy and traumatised cells, with the levels of induced chemical trauma controlled and independently verified, all of which are the topic of the following chapter.

Chapter 4

4 Negative Contrast Imaging Cellular Health

The previous chapter highlighted the ability of machine learning based methods for intelligent spectral data analysis, performed upon a small set of human tissue samples, imaged as part of a previous study [94]. Due to the limited sample number, alongside the requirement to control the sample trauma for investigations into differing cell trauma methods, the following work utilises cell cultures models for trauma analysis. An introduction into the motivation beyond the use of *in vitro* trauma models is presented, along with an outline of the methods used. This, alongside the use of the NCI device to collect spectral information of varying cell trauma models, generates the data for which the previously described data analysis methods are applied and modified for the larger data set. This work has been published in PLOS ONE under the title *'Machine learning utilising spectral derivative data improves cellular health classification through hyperspectral infra-red spectroscopy'* [127].

4.1 Introduction

IR hyperspectral imaging and spectroscopy methods have been used widely in clinical applications for a variety of medical problems since the 1990s [137]. One of the most common areas for this technology is within the field of wound healing and diagnostics, covering a range of medical applications including diabetic foot ulcers [138] and burns [139]. These methods detect spectral information, such as those discussed in 2.1.3 from the underlying biology and assess differences between healthy and non-healthy tissue and their cellular constituents. Despite these

73

advances, many of such methods are still focused upon the NIR optical window, while there has been some insight into the SWIR region, incorporating 900 to 2500 nm [140]. This has also been extended further into the MWIR region with both IR and Raman microspectroscopy [141], but little work has been done using macro tissue or cellular models.

Spectroscopic imaging in the extended IR region, beyond the conventional NIR methods used, requires additional considerations for both sample preparation and imaging methodology. Due to the high absorption of water within this region, biological samples are often chemically 'fixed' to remove the unwanted water signature [142], however this process can also remove significant spectral features, such as water concentration itself, along with degradation of the cell membrane which effects lipid concentrations, for accurate classification [143, 144]. Despite these challenges, imaging further into the IR window would provide complimentary information about specific spectral features such as lipids, collagen and other cellular constituents for clinical diagnostics, alongside current imaging modalities including SFDI [145], LDPI [71] and thermography [146], which are more readily available.

Most methods used to date investigate *ex vivo* tissue samples only, which contain multiple signals from bulk tissue, such as cells, blood and other tissue constituents. These mixed signals are difficult to separate, prompting work towards in vivo methods of individual elements contributing to detectable spectral features. Live cell imaging methods have been advancing in the last two decades, through the use of microspectroscopy and Raman spectroscopy [146, 147]. These also often require specialised cell preparations, including fixing and drying of samples, which have

been shown to exhibit a loss in cellular content, effecting the resulting IR spectra and detectable contrast [144]. More recently, the work has moved towards custom imaging systems for live cell analysis, such as the use of narrow viewing windows and IR transparent housing [148]. It has been shown that in both the SWIR and MWIR, spectral regions of interest corresponding to lipids (1200, 1400, 1700, and 3333-3533 nm), collagen (1200 and 1500 nm) and other cellular constituents are detectable [147, 149, 150]. These studies highlight the need for further inspection into the IR region, with the need to target several different wavelengths of interest across a broad spectral range using a hyperspectral approach that will maximise signal contrast and features, while minimizing signal contamination from its local sampling environment.

Compared to the methods discussed, hyperspectral methods utilise up to three orders of magnitude more wavelengths, vastly increasing the size and dimensionality of the resulting data-set. This subsequently creates an additional need for intelligent data analysis, which was introduced through the concepts of classification and dimensionality reduction in Chapter 3, to produce both reliable and easy-to-interpret results for the clinical setting. In traditional clinical imaging, simple statistics such as mean values, standard deviation and range, of simple detectable characteristics such as intensity of each pixel within a single image, or the differences across a temporal data-set, are used to aid clinical diagnosis. However, for larger dimensional data-sets this provides a challenge with the increased number of variables and dependability of these values across samples, imaging environment and sample preparation, i.e., signal contamination. The use of machine learning (ML) in medical applications is not new [151], although the majority of these methods

use supervised learning approaches, which require large data-sets, which are not often available within pre-clinical studies, where these methods are typically developed. Unsupervised methods, such as clustering, alongside dimensionality reduction methods, offer an alternative; these require reduced data-sets removing any bias created in the supervision stage [152].

K-means clustering provides a method in which a pre-defined number of clusters can be used. For a binary diagnostic problem of healthy versus traumatised as used for this study, k=2, where k is the number of required clusters, creating a two-cluster problem designed for the separation of the two different cell states. K-means is often used in medical image processing to provide an improvement in image segmentation of different tissue types or classes, where ML tool is specifically applied to increase the accuracy of segmentation, as well as the total throughput of images as compared to human image analysis [153]. K-means has also been applied in the field of spectral analysis for clinical diagnosis, with endoscopic imaging producing a large spectral data-set, which were sampled and analysed using a pre-determined number of clusters to represent the different clinical diagnoses [154]. These applications, although just an example and not completely covering the vast amount of work undertaken in this field, highlight the ability of k-means clustering as an intuitive, controllable, and simple method for grouping similar data for diagnostic purposes.

PCA is an additional tool used for high dimensional data to aid in the clustering/classification process. PCA reduces the dimensionality of the data by re-representing the information onto a set of principal components that highlight the largest variability within the data-set [155]. PCA is often used in Raman

spectroscopy applications, for example, where spectral information is collected from different biological systems, such as single cells or tissue samples, with many high dimensional spectra collected from each system. PCA aids in the extraction of the differences between the obtained spectra, whilst reducing the dimensionality, aiding further with the post-processing computational time [156] and is commonly applied in spectral analysis prior to k-means clustering [135].

All the clustering methods outlined above utilise data from an imaging modality which typically undergoes pre-processing to improve clustering output, such as background noise removal, spectra/temporal smoothing, bias removal and averaging. Such data pre-processing converts raw measured data to different 'data-types' typically containing different information content. The use and effect of such data-types and utilisation of any clustering algorithm, then itself becomes an important issue to better understand the information content and feature selection for classification.

Here a combination of the use of IR hyperspectral imaging within the SWIR/MWIR window is presented alongside the use of unsupervised machine learning methods for diagnostic analysis. The combination of these two techniques, which combines the imaging method's ability to detect subtle spectral differences between cell culture models and the ability of ML to identify and classify these, produces a novel approach for the detection and diagnosis of cellular health. A live cell model was created, containing cells of relevance to wound biology and with facets that permitted interrogation in the mid-IR range and cell death induced. Spectral data was collected from live and dead/dying cells with the aim of determining spectral differences and grouping the two different cell states. K-means clustering and PCA

were applied to different data-types, to determine which method provides the most accurate and reliable diagnostic tool. The aim of this work is to provide a binary clustering tool for the diagnosis of the state of cell health. Following clustering, the use of *a-posteriori* information allows for a quantifiable comparison of the diagnostics tools ability to accurately diagnose the two different cellular health states.

4.2 Methods

4.2.1 Cell culture

Human dermal fibroblast (HDFa, Gibco) cells were cultured in 12-well Costar Transwell inserts with a polyethylene terephthalate (PET) membrane (Corning) in Medium 106 supplemented with Low serum growth supplement (all Gibco) at liquid-liquid interface (LLI) (4 inserts/plate). Growth medium was removed from inside the insert and reduced to 0.5 mL below the insert to achieve air-liquid interface (ALI), immediately before infrared imaging (Figure 4.1).
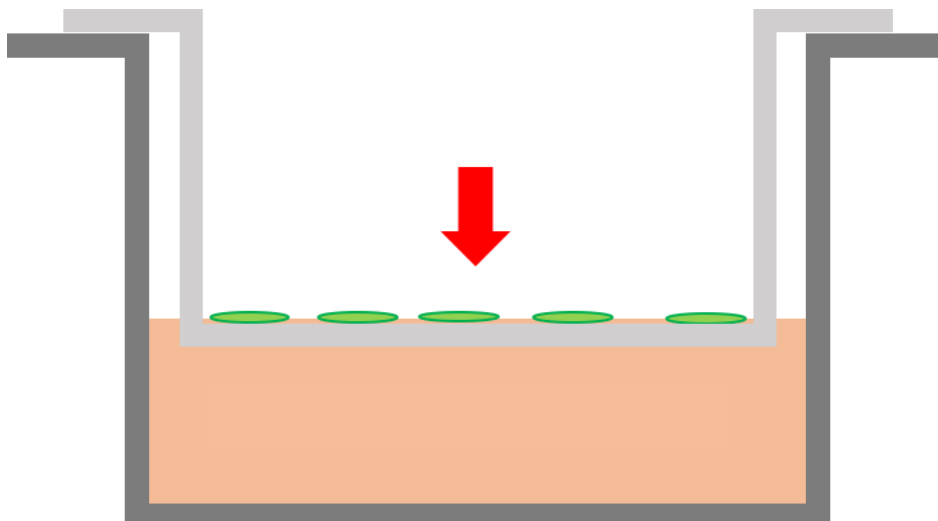
Figure 4.1: Air-liquid interface cell insert. Schematic representation of cells upon the air-liquid interface (ALI). The standard cell well is shown as dark grey, with the insert represented as the dark grey, which the cells, green, attach to.

Conditions for inducing necrosis and apoptosis were derived from the literature and confirmed for this cell line [157, 158]. Cells were seeded at 1 x 10^5 cells/cm^2 and incubated at 37˚C, 5% CO_2 overnight for at least 90% confluency the following morning. Necrosis was induced using 0.01% (v/v) Triton X-100 (TX100, Sigma) for 1 hr in serum free media (SFM) or 5 mM H_2O_2 in DMEM (Sigma) for 4 hr. Apoptosis was induced using 100 µM H_2O_2 for 4 hr. Cell death was confirmed by staining with Calcein AM (Invitrogen) and propidium iodide (Sigma), or Apoptosis/Necrosis Detection Kit (Abcam). For each experimental data set collected (biological replicate), two technical replicates were completed each for untreated, healthy controls, and treated samples. This imaging set-up was repeated for each of the different trauma types applied. A total of 18 repeats were collected across the three different trauma protocols, creating 72 (18 x 4) insert measurements of 36 healthy and 36 traumatised cell cultures.

4.2.2 Cell Staining

To confirm the apoptosis or necrosis of the cells following treatment, cells were stained with culture medium containing 2 µg/ml Calcein AM and 2 µg/ml propidium Iodide, or the Apoptosis/Necrosis Detection Kit according to manufacturer's protocol. Cells were visualised using an ImageXpress Pico cell imager (Molecular Devices). Figure 4.2 shows an example of the staining images collected for both the Triton X-100 and 5 mM H_2O_2 Apoptosis/Necrosis Detection Kit. The green CAM stain highlights the live cells, while the red PI stain the necrotic. Theses stains, along with those for apoptosis, confirmed the correct levels of chemical trauma were applied for the desired cellular health outcome. This further highlights the importance of an objective method for classification, with only estimates of the

quantification of cellular death possible, along with the importance of non-invasive imaging methods suitable for in vivo techniques, in contrast to the cell staining utilised here.
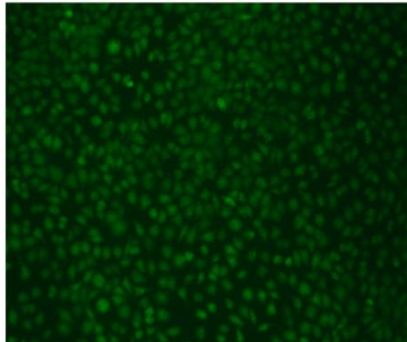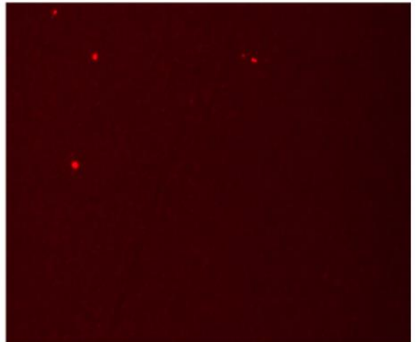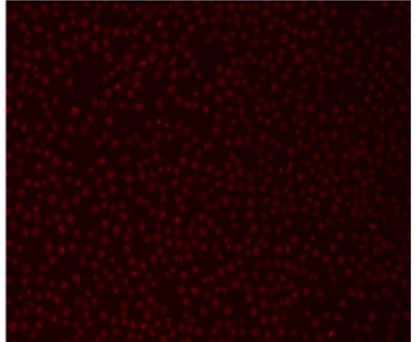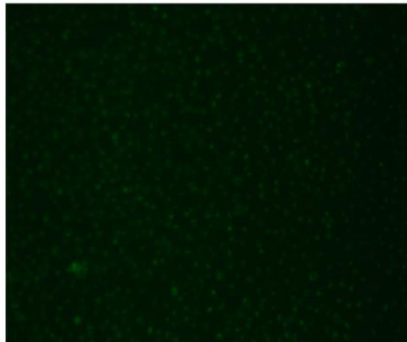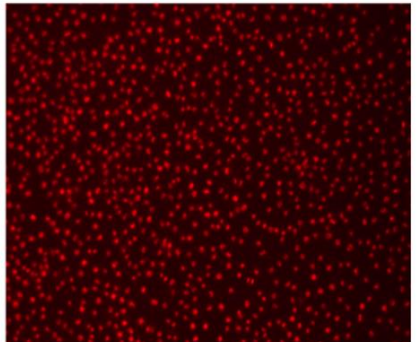
Trauma Agent	CAM stain (Live)	PI Stain (Necrotic)
Control		
Triton X-100		
5mM H$_2$O$_2$		

Figure 4.2: Necrotic cell staining. Confirmation of cellular trauma was achieved through the staining of treated cells. Necrotic staining was achieved using an Apoptosis/Necrosis Detection Kit (Abcam), with CAM stain (green) and PI stain (red) for the live/necrotic cells, respectively. These staining images show both the Triton X-100 and higher concentration of H2O2 produced >99% necrosis within the culture.

4.2.3 Negative Contrast Imaging (NCI) System Set-up

Hyperspectral images of the 12-well plates for the trauma study were collected using a prototype NCI device [96]. This NCI device, developed by M-Squared Lasers (Glasgow, UK), is a reflectance imaging device that collects hyperspectral images from illumination in both the SWIR/MWIR and has been used to identify spectral differences between wound biopsies, with seven human samples being imaged to predict their wound healing outcome [94].

Preliminary data was collected from the NCI, to identify image quality and characteristics. One clear issue was a spatial distortion present within all collected images, independent of system zoom or wavelength. This distortion originates from the hysteresis of the galvanometer actuated mirror at its turning points. This distortion was corrected in collaboration with M-Squared and is outlined in Appendix A.2. Alongside this correction, the placements of the external optical components were optimised for the imaging of cell culture systems.

Figure 4.3 shows the optimised system set-up for imaging of the cell inserts. The NCI device (1) outputs light at discrete wavelengths which then propagates to a gold coated steering mirror (2). This mirror reflects the light into the custom-built imaging housing (3), which maintains the sterile environment for the cell culture. The housing has a built-in calcium fluoride (CaF_2) viewing window (4), which is transparent within the wavelength region used for this study. Preliminary testing of reflectance phantoms within the custom-built housing was performed to assess the effects of any stray light and ensure the correct alignment of the gold-coated steering mirror and CaF_2 viewing window.
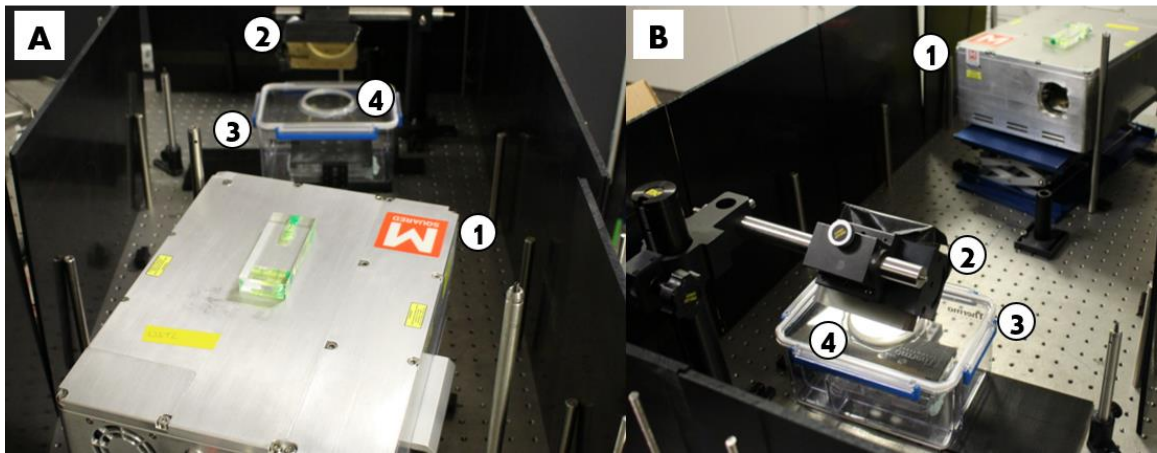
Figure 4.3: Negative Contrast Imaging (NCI) system set up. Images A and B show the set up used for collecting the hyperspectral images of the 12-well plates containing the cellular inserts. (1) Main NCI device (2) Gold coated steering mirror (3) Custom built imaging box (4) Calcium fluoride window.

A schematic representation of the same set up is shown in Figure 4.4, including the inner workings of the NCI, used to collect the hyperspectral data for each sample. All elements housed within the NCI device are contained by the dashed box, and a full technical description has been previously published [94]. The Intracavity Optical Parametric Oscillator (ICOPO) provides with illumination in the MWIR range used for this study (1). The outgoing beam is directed using an internal gold coated steering mirror (2) towards the two galvanometer mirrors controlling the y-axis (3) and x-axis (4) before leaving the NCI housing. The beam then propagates towards the external gold coated steering mirror (5) which directs the beam vertically towards the sample. The custom-built sterile chamber (6) contains a CaF_2 IR transparent optical window (7) allowing the transmission of the beam to the sample (8). The reflected light then travels back to the NCI system via the external steering mirror (5) and is directed towards the detection optics with the two galvanometers (4) and

(3) internally. A CaF$_2$ focusing lens (9) is then used before the reflectance signal is collected by a Zn doped MCT detector (10).
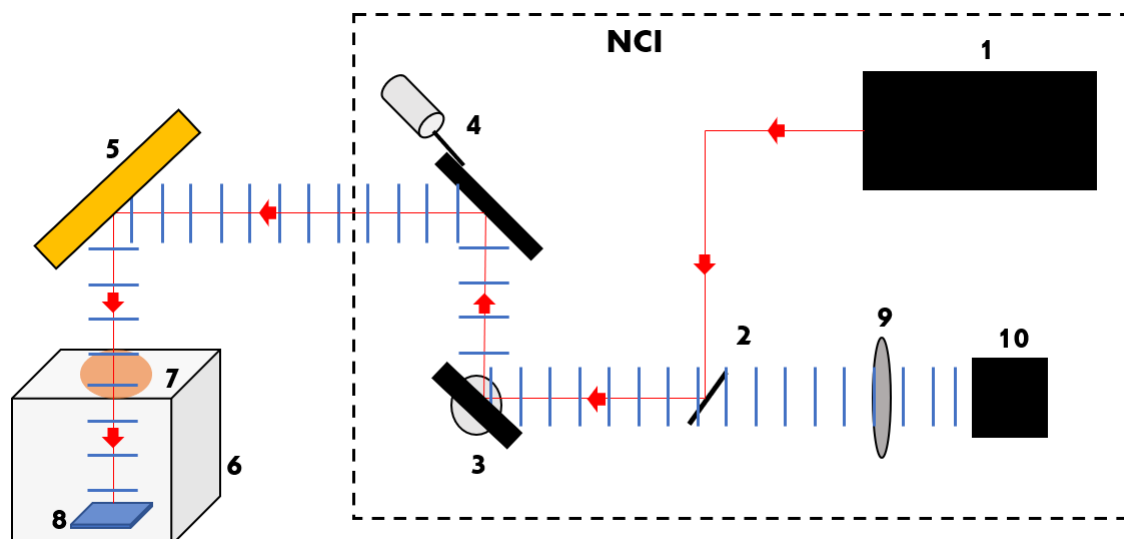
Figure 4.4: Schematic Negative Contrast Imaging (NCI) system set up. (1) The Intracavity Optical Parametric Oscillator (ICOPO) provides the IR illumination for measurements. The (2) gold coated steering mirror, (3) y-axis galvanometer mirror and (4) x-axis galvanometer mirror are also housed in the NCI system. (5) External gold coated steering mirror, (6) custom built transport chamber, (7) Calcium Fluoride (CaF2) viewing window all allow for the imaging of the (8) sample, within a sterile environment. The reflected light then retraces its path before passing through a (9) CaF2 focusing lens and onto the (10) MCT detector.

Images were collected using the NCIs built-in spectroscopy mode. The image resolution was selected at the highest possible resolution, 512 × 512 pixels, with the largest system magnification generating a field of view of 550 × 550 mm, resulting in a pixel size of 0.93 mm. Within imaging mode, the range and spectral resolution can be controlled, with 2500–3500 nm at 10 nm chosen respectively giving a total of 101 wavelengths. These settings, along with the raster scan speed of the NCI, resulted in a total imaging time of <7 seconds per image, including data transfer. These spectral images were then combined to produce a 3D data hypercube for analysis.

4.2.4 Image Analysis

Image analysis and the resulting ML applications were all performed using MATLAB. The data was grouped to form a 3D hypercube with x and y dimensions of each image corresponding to the first two dimensions (512 × 512), and the wavelength corresponding to the third (101). Each 3D data hypercube (512 × 512 × 101) was analysed individually to extract the spectrum for each of the 4 different inserts in the NCI field-of-view. Example images are shown in Figure 4.5 as taken at 2500, 2800 and 3450 nm to highlight the differences between the healthy (Blue) and traumatised (Red) 'Raw' spectra, with the standard deviation shown, representing a sample from the 101 images which make up the hypercube for each sample. For each insert, a region of interest (ROI) based on a-priori knowledge for the location of the well was drawn with specific attention to ensure exclusion of the region of internal reflection from the source within each well and contains all pixels within and on the dashed lines. This can be observed in the images as the area of saturation in the right-hand side of each of the 4 inserts, creating a 'C' shape area for each ROI. This region was first outlined using the 2500 nm image to identify the bounds of the cell inserts, which was clearly visible at this wavelength. The exclusion region was then identified using images at the higher wavelengths and systematically checked at different wavelengths to ensure no internal reflection is part of each insert ROI.

84
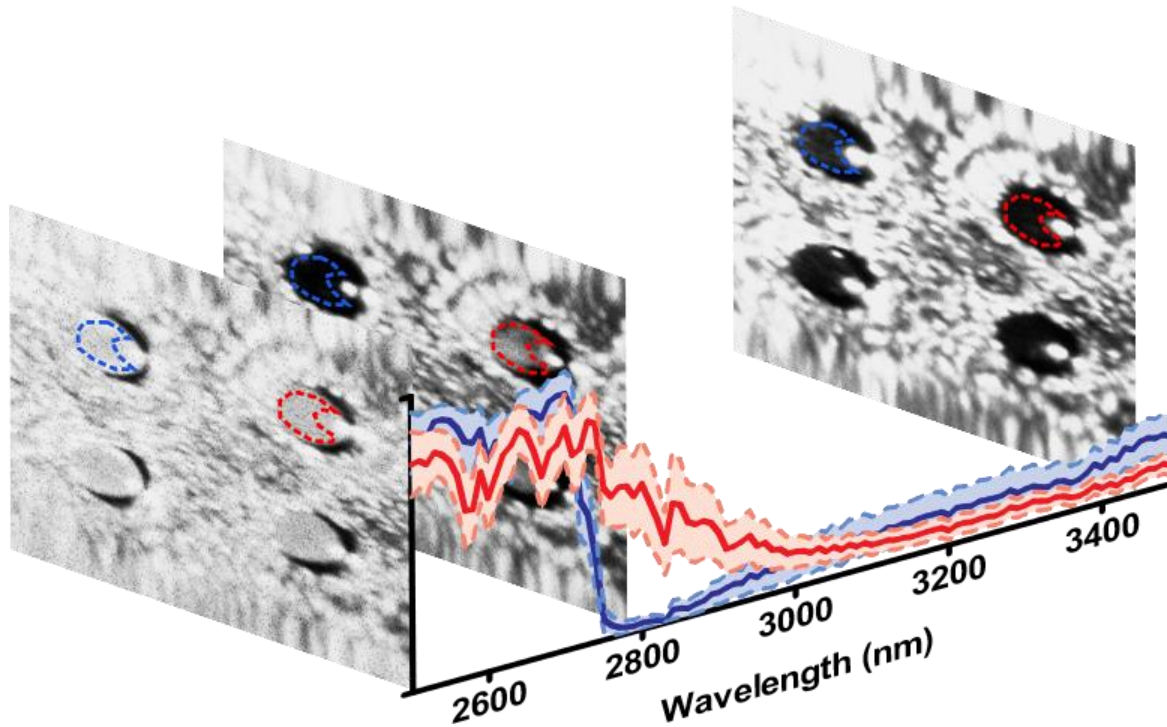
Figure 4.5: 3D Hyperspectral data cube. Visual representation of three example images from the NCI imager forming a 3D hypercube. The corresponding 'Raw' spectra of the mean of each ROI is also shown. The blue spectrum represents a healthy sample, and the red a traumatised sample treated with Triton X. A region of interest is obtained for each insert to collect the spectra from each sample, removing the spectral contribution of the internal reflection saturating the detector. This can be observed in the right-hand side of each well within the images.

These ROIs are then propagated throughout the hypercube for each data set, to resample the full spectra from each insert, within all 18 repeat measurements for the three different trauma protocols, which were then analysed by combining the 72 (18 × 4 inserts) individual ROI spectra to generate the large data-set containing all the combined 36 healthy and 36 traumatised samples.

4.2.5 Machine learning for cellular health detection

Once the spectra for each sample had been obtained, the next step was to assess different pre- and post-processing methods for the measured and re-sampled raw data. Using the knowledge gained from data processing in Chapter 3, a variety of different methods were applied, which are next outlined.

Data Pre-processing

Three different pre-processing methods have been used in this study, which were combined to generate four additional data-types, alongside the conventionally used raw ROI mean. The first involved utilisation of the 'smoothts' function within MATLAB to smooth the spectra for each data set. This function was chosen due to its ability to control the size and characteristics of the smoothing function, as compared to other available smoothing functions. A 5-point window size was used along with a gaussian smoothing function with a 0.5 standard deviation, which was applied to each spectrum from the ROI of the corresponding insert. Each smooth spectral point, $R_{S(\lambda)}$, was calculated as follows,

$$R_{S(\lambda)} = \sum_{\lambda-2}^{\lambda+2} R_{(\lambda)} \cdot \hat{G}, \qquad (4.1)$$

where, $R_{(\lambda)}$ is the raw reflectance data at wavelength λ and $\hat{G}$ is the normalised gaussian function in 1D, with a window size 5, standard deviation of 0.5, as implemented within the 'smoothts' MATLAB function. These window parameters were chosen to reduce the noise within each spectra, whilst maintaining the dominant spectral features.

The second method applied was a simple background correction, which allows for the consideration of any spectral contributions from both the cell trauma method as well as the cell inserts. A supplementary data set was also collected for the three different trauma types and healthy controls. For each of these, the treatment media was applied to the standard four inserts set up, with no cells seeded. The same spectra, using the NCI, were collected and the spectra of each of the four inserts were then averaged (mean) to generate the background spectra for subtraction. Each spectra from the inserts containing live cells were then simply matched with

the corresponding media background spectra, which was then subtracted for each wavelength to generate the background subtracted data-type, $R_{BG(\lambda)}$.

$$R_{BG(\lambda)} = R_{(\lambda)} - M_{(\lambda)} \qquad\qquad (4.2)$$

where, $R_{(\lambda)}$ is the raw reflectance data and $M_{(\lambda)}$ is the reflectance data from the corresponding media only spectrum from the same trauma method at wavelength λ. As the cell insert preparation protocol is independent of the trauma method, removal of the background will highlight the differences between the healthy and traumatised sample spectra only and should remove any contributions from the cell trauma method or cell culture plastics/insert. Each of these three data-types are shown in Figure 4.6 A for comparison, showing a single traumatised spectrum.
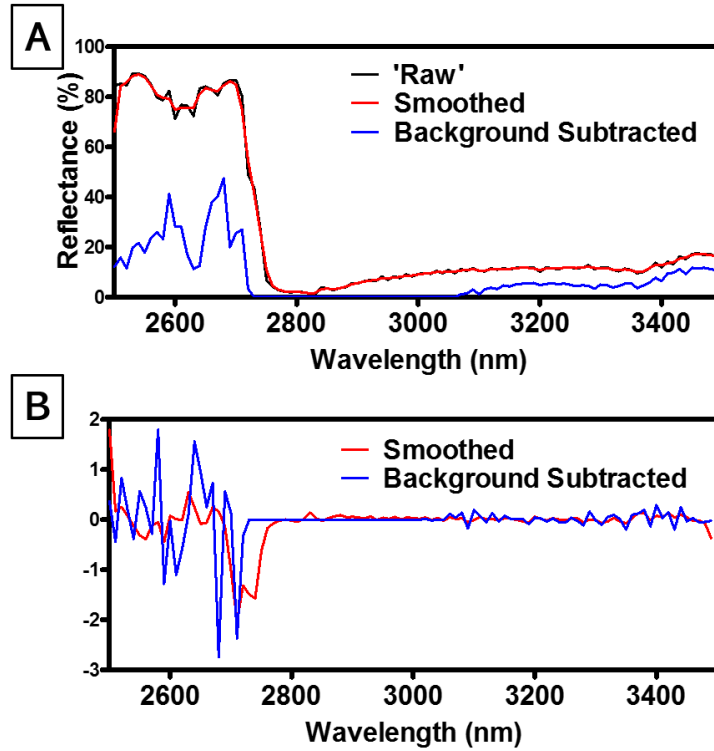
Figure 4.6: Pre-processing data-type visualisation. A: Spectral comparison between the 'Raw', smoothed and background subtracted data-types for a single traumatised spectrum. B: Spectral derivative comparison for both the smooth and background subtracted data sets shown in A.

The final pre-processing applied was to calculate the spectral derivate of each data set. Derivative spectroscopy methods have been used since the 1950s, becoming more common place in the 1970s with the increased computational power available at the time. These methods are now common place in a variety of disciplines to eliminate any background signals and for resolving overlapping spectral features [159]. While these methods can be shown to amplify noise, derivative- based methods consider the direct relationship between the nearest neighbour wavelength measurements and hence can account for any spectrally independent systematic noise [160, 161]. This includes the field of wound healing, where derivative spectral methods have been utilised in Fourier Transform Infrared Spectroscopy for the classification of the spectral patterns for burn wound healing [162]. The spectral derivative, $R_{SD(\lambda)}$ can be calculated as show in Equation 4.3 below,

$$R_{SD(\lambda)} = \frac{dR}{d\lambda} = \frac{R_{(\lambda+1)} - R_{(\lambda)}}{(\lambda+1) - \lambda},$$ *(4. 3)*

where $R_{(\lambda)}$ is the reflectance spectral value at a given wavelength λ. This method was applied to both the smoothed and BG subtracted data, generating the four additional data-types mentioned, which along with the raw ROI mean data, make up all the data-types tested for this study. An example of the 1st derivative of the smoothed and background subtracted spectra example are shown in Figure 4.6 B.

Post Processing

Each of the five data-types outlined above, also shown in Table 4.1 , were also subjected to two different post processing steps, clustering, and PCA-clustering, which have been described fully in Chapter 3. The popular k-means clustering algorithm, first described in the late 1960s [163], has been used to separate the data into 'healthy' and 'traumatised' clusters, which was then compared to the ground truth labels. For this study, two clusters (k=2) were considered to represent the 'healthy' and 'traumatised' groups. The k-means clustering was applied to each of the five different pre-processed data-types to generate the clustering labels needed for their comparison. Due to the initial random assignment of the initial k cluster centres, the results can be subject to variation. Therefore, the k-means process was repeated 5000 times, producing a ≤1% variation in the clustering frequency, which was then defined as the number of times the modal clustering arrangement was reached divided by the total number of k-means repeats.

Pre-Processing Data-type	Post-Processing Data-type	
	k-means	PCA and k-means
'Raw'	98.5	98.2
Smoothed	93.0	99.3
Background Subtracted	100.0	100
Spectral Derivate of Smoothed	47.6	34.7
Spectral Derivative of Background Subtracted	52.1	39.6

Table 4.1: Clustering frequency results for each of the pre- and post-processing data type.

The second and final post processing method applied was using PCA [164]. This dimensionality reduction technique was applied to each of the five different pre-processed data-types, reducing the original N-dimensional data set, N = 101, to that in which has M dimensions, representing ≥95% of the variance, such that M<<N. When the dimensionality of this data is high, these metrics can be affected by the sparsity of the data across all dimensions, resulting in poor clustering, an attribute of the 'curse of dimensionality'. The use of PCA in wound healing hyperspectral imaging has been shown for the prediction of healing in diabetic foot ulcers, along with a threshold value for oxygenation or given principal components as a classification tool [111]. Research into clustering within high dimensional data has shown that, in general, reducing the number of dimensions improves the clustering using simple distance metrics, such as the cosine distance used in this study, but there is no general 'one size fits all' rule which can be applied to all data sets [165]. Therefore, both the full dimensional data sets, and those reduced by PCA were

analysed to determine the optimal procedure to correctly cluster the two different cellular health states. A full breakdown on the data collection process is shown in Figure 4.7.
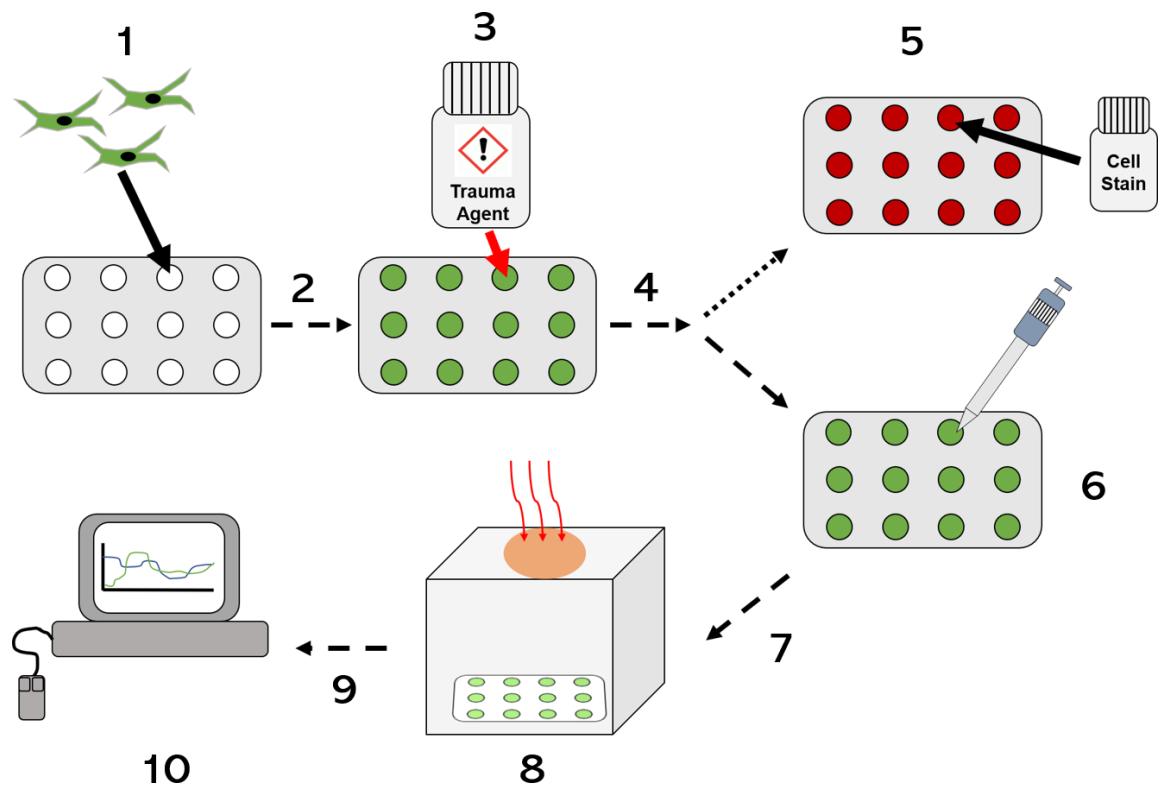
Figure 4.7: Data collection workflow. (1) HDFa cells are seeded onto 12-well plate inserts. (2) Cultured overnight until >90% confluent. (3) Treated with cell trauma inducing agent. (4) Incubated for 1-4 hours dependent upon cell trauma agent. (5) Cell staining to confirm apoptosis/necrosis levels. (6) Reduction of growth medium to 0.5 mL for imaging preparation. (7) Transfer to imaging box for NCI data collection. (8) Image collection using NCI SWIR/MWIR detector. (9) Images analysed to produce cell spectral data. (10) Pre- and post-process spectral analysis.

4.3 Results

To compare the clustering results of each of the different data-types, two additional metrics were used alongside the clustering frequency. Using the known status of each sample class, healthy or traumatised, two metrics for quantifiably comparing the clustering results were created. These are called Trauma Clustering Index (TCI) and Healthy Clustering Index (HCI) are defined as follows:

91

$$TCI = \frac{\#\,True\;Trauma\;Sample}{\#\,False\;Healthy\;Sample + \#\,True\;Trauma\;Sample} \qquad (4.4)$$

$$HCI = \frac{\#\,True\;Healthy\;Sample}{\#\,True\;Healthy\;Sample + \#\,False\;Trauma\;Sample}. \qquad (4.5)$$

Here, a true trauma sample result is one in which a traumatised sample is clustered with a majority of other samples which also contain the trauma label, while a true healthy sample is one where a healthy sample is clustered with a majority of other samples containing the 'healthy' label. These two metrics were chosen to provide additional information about the accuracy of the binary clustering algorithm used within this study, by quantifying the algorithms' ability to cluster spectra of the same class in the same clusters. Taking a combination of both TCI and HCI, an estimation of the accuracy of the clustering using the previously known labels can be made. This accuracy is defined as the mean of the two metrics. An ideal medical diagnostic test will be 100% accurate, i.e., all healthy patients will be identified as healthy, and all diseased as diseased, with no incorrect diagnosis. An accuracy of 100% is highly unlikely, requiring careful consideration of any given tests reported accuracy value. By considering the TCI and HCI of this diagnostic tool individually, a quantification for the number of false positives and negatives has been shown. This is important for this diagnostics tool, as the treatment, or lack of, to an incorrectly diagnosed diseased state can have detrimental effects on a patient's outcome.

Figure 4.8 shows the results for each of the five different data-types being processed directly by the k-means algorithm. Here, the raw mean, smoothed and BG subtracted all exhibit clustering frequencies of >90%, however show low scores, <25%, for either TCI or HCI. The spectral derivate of the smoothed data showed an improvement upon the three previous datatypes, with all three metrics above 40%, although the TCI is still below 50%. The most promising result comes for the spectral

derivate of the BG subtracted data set. Here, both the TCI and HCI were >94%, while the clustering accuracy was above 50%.
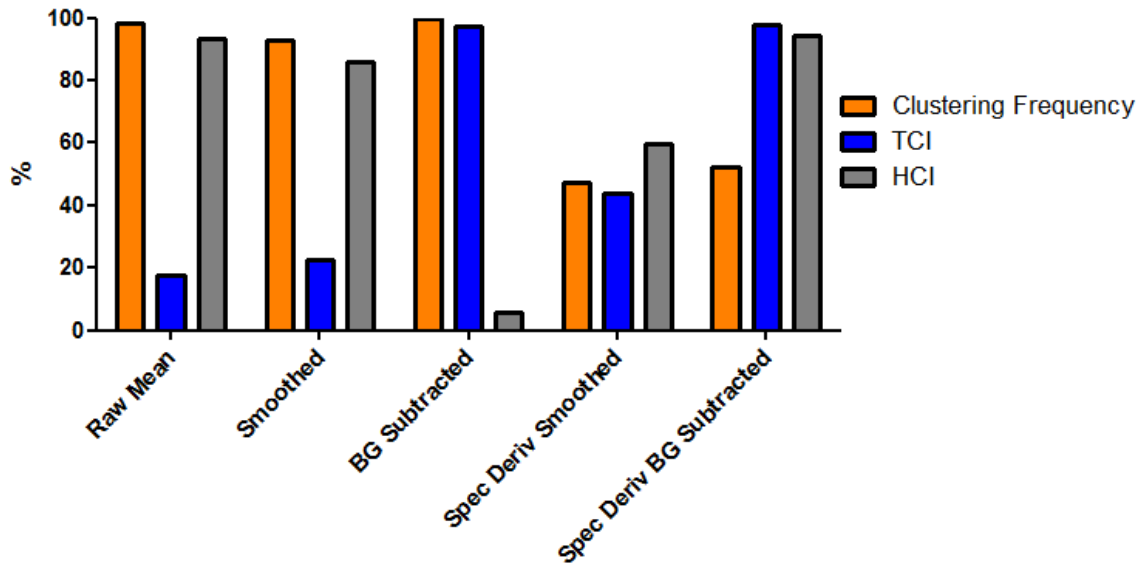
Figure 4.8: Non-PCA data analysis. Three different metrics, clustering frequency (Orange), TCI (Blue) and HCI (Grey) were used to quantitatively compare different data-types obtained from the raw hyperspectral images.

This clustering was repeated for each of the five different data-types following the application of dimensional reduction, through the implementation of PCA. The number of principal components (PCs) for each data set was chosen such that >95% of the variance within the data set was represented, resulting in 4–14 PCs being considered, reducing the dimensionality from the original 101 dimensions, representing each of the wavelengths collected. The cumulative variance plots for each of the five different pre-processing types are shown in Figure 4.9, with the 95% threshold represented by a dashed line.
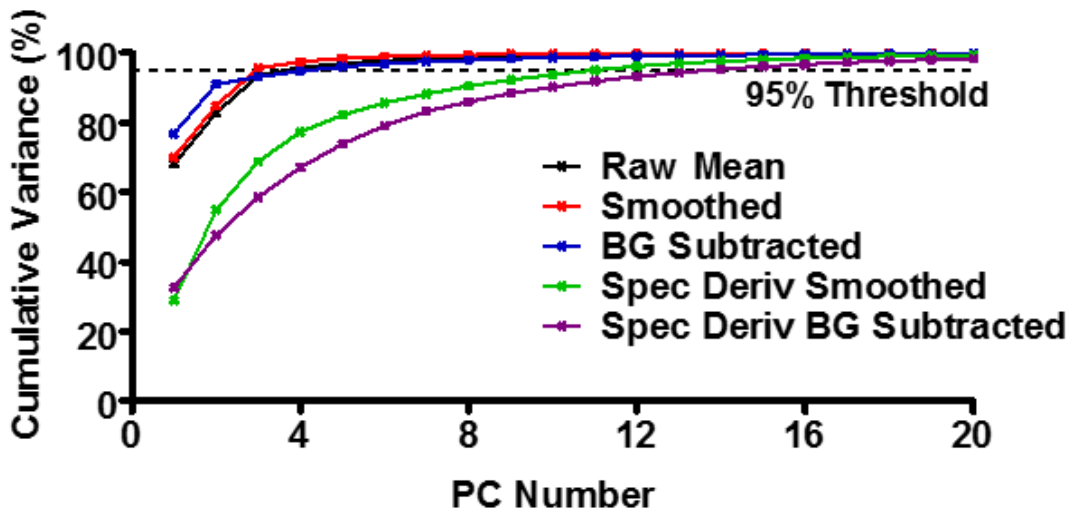
Figure 4.9: PCA cumulative variance. For the five different pre-processing data-types, the plot of the principal components (PC) against the cumulative variance is shown. Each data-type was represented by the PC number which incorporated >95% of the variance in the PCA and k-means study.

For each of the PCA reduced data sets, the results are shown in Figure 4.10. Again, the five different data-types were compared using the clustering frequency, TCI, and HCI. Similar results were observed for the first three data-types; raw mean, smoothed and BG subtracted. These showed a high clustering frequency of >90%, along with a low, <20%, TCI and HCI. An improvement was seen with both the spectral derivative data-types. The spectral derivative of the smoothed data provided both a TCI and HCI of ~50%, while the clustering frequency was observed to be half of that seen in the non-PCA equivalent. As with the non-PCA result, the data set with the highest values for both TCI and HCI were found to be the spectral derivative of the BG subtracted data. Both values were >90%, although were slightly lower (0.3–1.1%) than the non-PCA data set, and the clustering accuracy was greatly reduced to <40%.
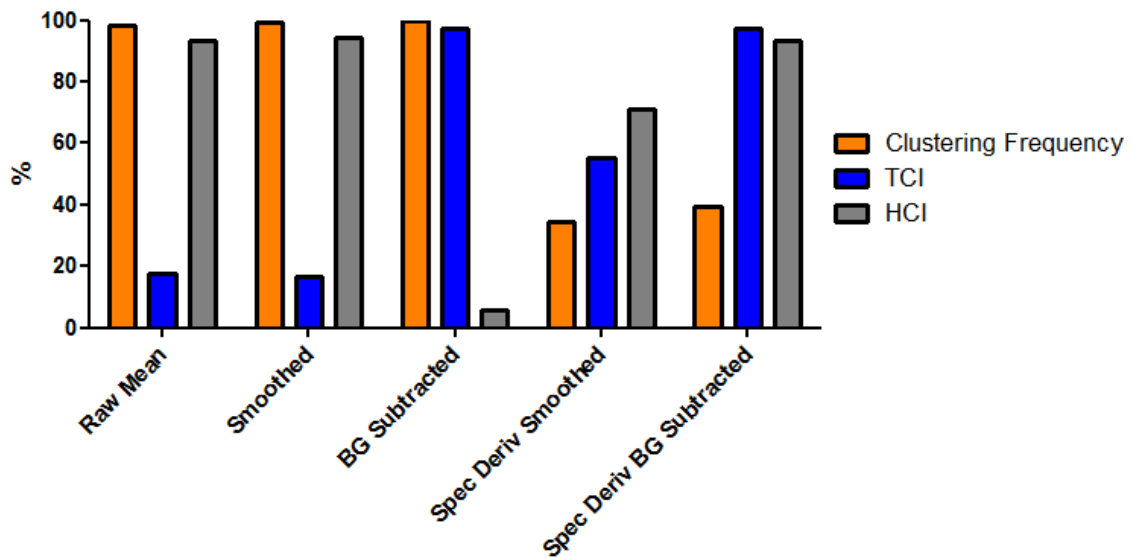
Figure 4.10: PCA Data Analysis. Three different metrics, clustering frequency (Orange), TCI (Blue) and HCI (Grey) were used to quantitatively compare different data-types obtained from the raw hyperspectral images, following PCA dimensional reduction, with >95% of the data variance retained.

4.4 Discussion

4.4.1 Algorithm

The spectral derivative of the background subtracted data has been shown to be an effective and reliable tool for diagnosing healthy and traumatised cellular samples. Any binary diagnostic test, such as one to define if a sample is healthy or not, can have its accuracy quantified using both TCI and HCI. For example, a test which has a low TCI and a high HCI, while accurate in labelling healthy samples correctly, the inability to identify traumatised samples would render the test unsuitable as a diagnostic tool. This outcome was observed in raw mean and smoothed data-types of the clustered (Figure 4.8) and PCA-clustered (Figure 4.10), with the full results shown within Tables 4.1-4.3 for the clustering frequency, TCI, and HCI respectively.

95

Pre-Processing Data-type	Post-Processing Data-type	
	k-means	PCA and k-means
'Raw'	17.8	17.8
Smoothed	22.5	16.9
Background Subtracted	97.2	97.2
Spectral Derivate of Smoothed	43.9	55.3
Spectral Derivative of Background Subtracted	97.8	97.6

Table 4.2: TCI results for each of the pre- and post-processing data type.

The opposite of this was seen in the background subtracted data, with high TCI but low HCI. While accurate at identifying those cells which are traumatised, it is poor at confirming cells which are healthy. In a clinical setting, this would translate to the potential treatment of healthy samples, wasting resources and time, or in wound debridement, to the unnecessary removal of healthy tissue which can cause additional problems in the wound healing process and in the patient's future.

A significant improvement was seen in both spectral derivative data-types. The spectral derivative process adds to the complexity of the data by considering the changes in the reflectance spectra between neighbouring wavelengths. Through this simple step, additional bands in the data can be detected, and suitable spectral features enhanced. A previous study has looked at the effects of smoothing and spectral analysis up the exploration of subtle spectral differences [166]. However, the algorithms developed and optimised were modified for use with remote sensing

data, therefore this study considers a more traditional spectroscopic method via hyperspectral image analysis. The outcomes of both this study and that of Tsai et al highlights the importance of additional post-processing spectral analysis to improve upon the identification of key spectral features [166].

Pre-Processing Data-type	Post-Processing Data-type	
	k-means	PCA and k-means
'Raw'	93.2	93.2
Smoothed	85.8	94.2
Background Subtracted	5.6	5.6
Spectral Derivate of Smoothed	59.7	71.3
Spectral Derivative of Background Subtracted	94.4	93.3

Table 4.3: HCI results for each of the pre- and post-processing data type.

The first spectral derivative data-type to discuss is the smoothed data. Although exhibiting a lower value for clustering frequency in both the non-PCA and PCA post-processing types, at ~50%, this is still a definitive clustering, with the 72 samples offering many possible clustering outcomes. Again, the TCI and HCI were around 50% for the two post-processing types. Despite this improvement, for a binary diagnostic test with an even distribution of healthy and traumatised samples, a 50% TCI and HCI would be achieved through a random assignment of 'healthy' and 'traumatised' clustering labels with a $p = 0.5$, $q = 1-p$ probability respectively.

The final data-type tested was the spectral derivative of the background subtracted data. The raw background subtracted data exhibited a high clustering frequency and TCI, but the lowest HCI, ~6% for both post-processing types. Despite this, the spectral derivative of this data-type showed a significant improvement with the values for both TCI and HCI of >90% across all 5000 k-means clustering repeats. For the modal cluster, observed at a frequency of 52% and 38% for non-PCA and PCA respectively, all traumatised samples were correctly labelled while ≤3 of the healthy samples were incorrectly labelled as 'traumatised'. In terms of a diagnostic test for wound healing, this method would provide an accurate and reliable measure for determining the status of cellular health.

For the data reduction method as applied in this study, PCA, the accuracy of the cell health clustering was comparable to the non-PCA data equivalents. Although the data dimensionality was reduced to as low as 3, compared to the full 101 wavelengths for the full data, different data reduction methods could also be investigated in future studies, with the aim of increased clustering accuracy and improved cluster grouping as represented by the silhouette score. Partial least squares (PLS) is an additional dimensionality reductions methodology that considers the correlation between both the dependant and independent variables, unlike PCA which only considers the independent variables [167]. Such methods have also been further developed with modified versions for analysis of Raman spectroscopy, with improved classification shown [168]. Dimensionality reduction could also be explored further through the use of autoencoders, which also consider non-linear contributions, although these require additional computation due to its neural network design [42].

These results also highlight the methods ability to determine the state of the cellular health, independent of the trauma methods applied. Of the three different trauma methods used for this study, Triton X and H_2O_2, at the higher concentration of 5 mM, both induced necrosis of the cells. This form of cell death, which is not programmed and is unregulated, is different to apoptosis, or controlled cell death, which was induced with the lower H_2O_2 concentration of 100 μM. Despite these two different mechanisms, the imaging method and analysis can diagnose the healthy and traumatised samples. While the accuracy of the clustering algorithm through TCI and HCI calculations provides one metric for quantifiable comparison between data types, it is also possible to further assess the quality of each formed cluster. Silhouette cluster analysis is a method in which a data point is compared to every other within its cluster and a score from -1 to 1 is calculated for each point. A high score suggests a data point is closely matched with the other points within its own cluster, and a mean score can then be calculated for each cluster to quantify the quality of each formed cluster. With the TCI and HCI being the highest for both spectral derivative data types, the mean silhouette score for points within each cluster is shown in Figure 4.11 (A) for the non-PCA and Figure 4.11 (B) for the PCA results.
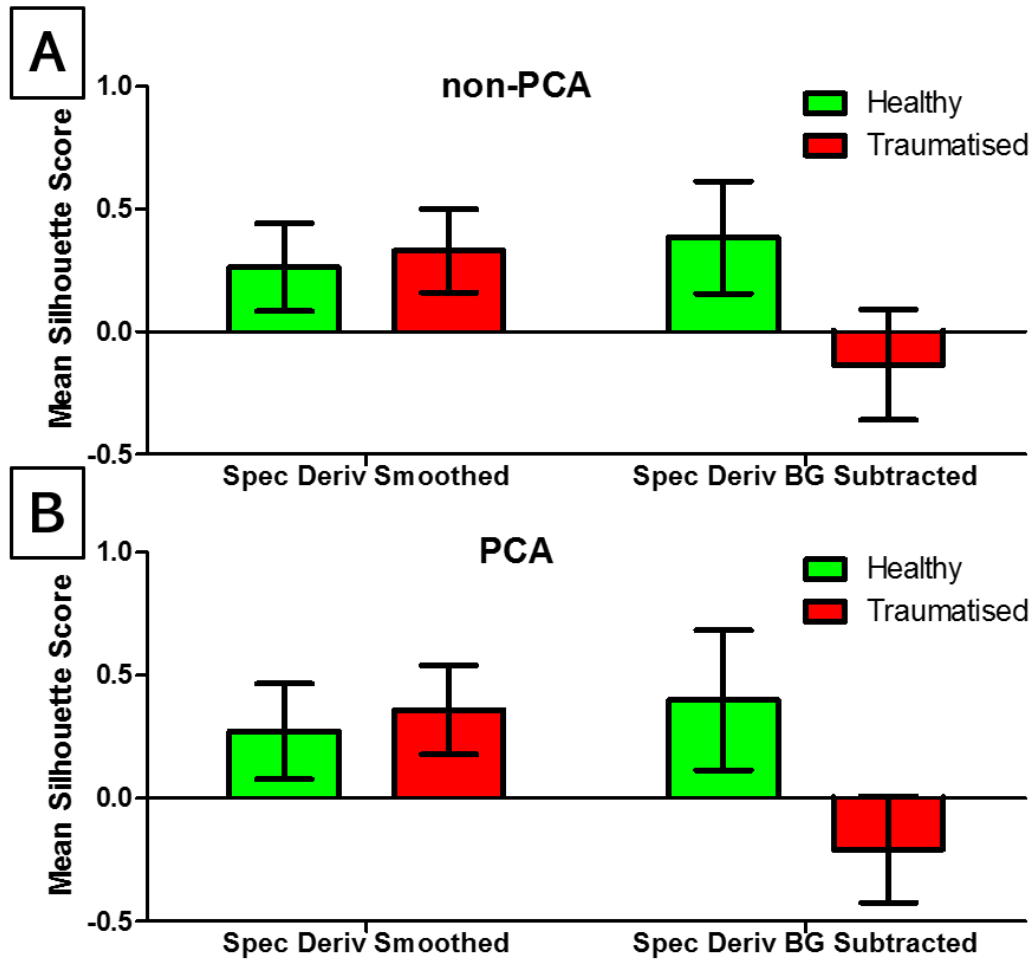
Figure 4.11: Silhouette cluster analysis. Mean data point silhouette score for each point within the healthy and traumatised cluster for (A) non-PCA and (B) PCA spectral derivative data types.

The positive mean silhouette score for both of the spectral (the non-PCA and PCA) of the healthy samples suggests the formation of good clusters for each of the different methods, with this also being observed in the spectral derivative smoothed data for the traumatised cluster. However, the data type with the highest TCI and HCI, >93% for both non-PCA and PCA, exhibits scores of <0 for the traumatised cluster, could demonstrate that the formed clusters are either weak or artificial and that k-means clustering may not be the most suitable method as applied in this work. This may be due to the formation too few clusters and further work should investigate alternative clustering methods, such as hierarchical clustering, in order

to determine the optimum number of clusters within each data set and confirm the reliability of the clustering algorithms [169, 170].

As seen in previous literature, the differences between both healthy and traumatised cells were detectable within the IR spectral region. The upper band of this study, 3000–3500 nm, has been investigated through the use of FTIR spectroscopy [147, 149], with differences attributed to the changes in cellular proteins and lipids during the apoptotic and necrotic processes. However, the sensitivity of a FTIR spectrometer is much greater than the NCI used here, and differences between the sample preparation must also be considered. Specialised sample preparation steps, including the drying and fixation of the cell monolayer have to be taken when using FTIR spectroscopy, which can affect the resultant spectra [144]. In this study, the cells were imaged within aqueous media and grown upon liquid-air interface inserts, allowing reflectance measurements to be taken without transmittance through the cell media solution. Although this provided a different method for imaging and spectral collection, differences between the healthy and traumatised samples were detectable, and accurate clustering of the two different cell health states was achieved. A comparison between a healthy and traumatised sample is shown in Figure 4.12, presenting the spectral derivative of the background subtracted data. This highlights a few key considerations and findings from this study. Firstly, as detailed above, the region between 3000–3500 nm has been considered with FTIR spectroscopy. For both the healthy and traumatised samples, this region is flat, due to the lower sensitivity of the NCI device, compared to that of an FTIR. However, a visual difference is observed from 3350–3500 nm, which has been shown to represent changes in lipid and protein conformational changes [147, 149]. Second,

the 2500–2700 nm contains the largest proportion of the spectral derivative information over the entire imaging range. Previous studies have considered >3000 nm [149], along with limited investigation in the SWIR region incorporating 1000–2000 nm [150]. This study highlights a new region of investigation in live cell spectra, meriting further work within this spectral region.
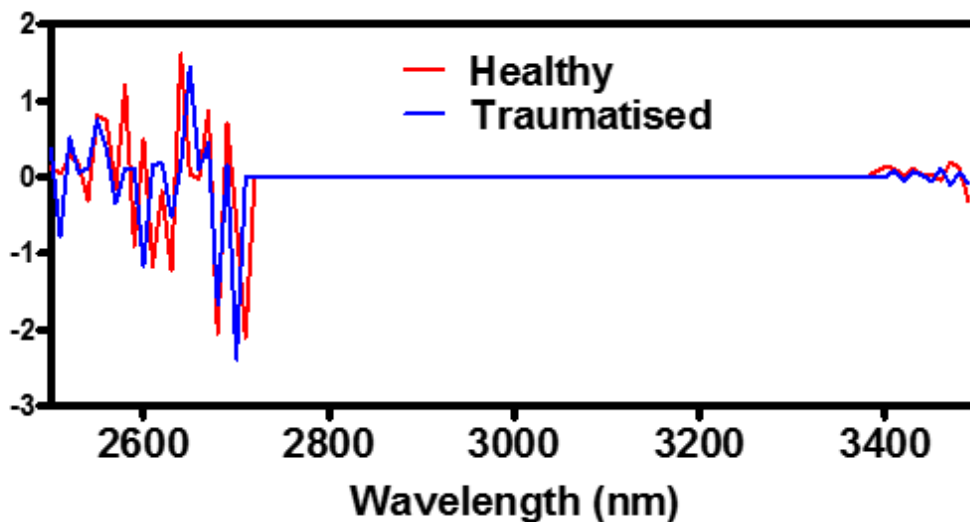
Figure 4.12: Healthy and traumatised derivative spectra. Comparison between a representative healthy and traumatised cell spectra of the spectral derivative background subtracted pre-processing type.

Finally, the differences between the two spectra shown in Figure 4.12 are subtle, which makes them difficult to differentiate visually. The use of ML has shown the ability to separate these results with a high level of accuracy, correctly classifying >93% of the samples. The TCI and HCI can be combined to produce a single 'accuracy' metric for any given medical test. Due to the equal measurements of both healthy and traumatised samples, this metric is calculated by simply taking the mean of both values for each post-processing datatype. The resulting accuracy of both tests was above 95%, with the PCA before k-means observing the lower of the two tests at 95.5%, compared to the simpler k-means only accuracy of 96.1%. This

study, conducted across the SWIR/MWIR spectral regions, draws a focus to investigating additional IR regions to aid in the diagnostics process. Current wound healing diagnostic procedures rely upon visual inspection by trained clinicians, which introduces increased subjectivity and varying results of accuracy [2]. The introduction of clinical imaging and ML diagnostic tools beyond the visible-NIR range will aid in this process, although further study into more complex cellular or tissue models will be required. Whilst this study has highlighted the existence of differences between healthy and traumatised cell culture samples, no information on the specific biological constituents that give rise to these differences has been shown.

4.4.2 Sample Size

An increase in the number of samples tested, which was limited to 72 samples for the presented study, along with a thorough investigation into the biological changes that are occurring at the cellular level will further highlight the individual spectral contributions. A benefit of this presented method is to investigate the whole spectral range to identify any differences present, which is the only requirement for a diagnostic clustering purpose, with future work focussing upon each spectral contribution. Furthermore, a larger sample size would allow for the testing of further clustering and classification methods, with the aim of producing a binary classifier to clinically assess cellular health. However, for an increased sample size, further modifications to the NCI for increased imaging time should be considered. The current image capture and file transfer time is <7 s per wavelength. For the 101 wavelength sweeps performed for this study, this represents over 10 minutes of acquisition time per hypercube. Whilst this was suitable for controlled experiments

of cell cultures, use of the NCI for real-time medical imaging would require significant improvements. This could be improved by both advancing the raster scanning optics of the image acquisition, alongside improvements to the image transfer system, which is currently performed using a separate laptop via an ethernet data transfer. Adaptions to the inbuilt image acquisition system would improve this time, alongside improvement to the imaging capturing software. The current system is operated using a Graphical User Interface (GUI) which is optimised for a single wavelength acquisition. Live image viewing is updated in real time, with a series of parameters, such as resolution and wavelength easily alterable. The wavelength sweep mode is less developed, with improvements such as whole image analysis for live spectral viewing, pre-saved imaging parameters and an extensive library of known spectra being of significant benefit to the system.

4.5 Conclusion

In summary, the use of a SWIR/MWIR hyperspectral imaging device, along with machine learning algorithms, has been shown to differentiate and diagnose the spectral differences between healthy and traumatised cell cultures. Human dermal fibroblast cells were imaged using an NCI imaging device, with hyperspectral images collected between 2500–3500 nm with a 10 nm resolution. Spectral information for both healthy and traumatised samples, dosed with trauma inducing agents, were analysed using a variety of different pre- and postprocessing methods. k-means clustering was applied to these different data-types, with the aim of correctly identifying the cellular health of each sample. The raw, background subtracted and smoothed data-types, although showing >85% for one of either TCI or HCI, were unable to accurately diagnose the cellular health of each sample. This

accuracy was greatly improved to >95% for both the full data set and the dimensionally reduced set corresponding to the spectral derivative of the same background subtracted spectra, however the formed traumatised clusters were found to be weak (as compared to healthy) suggesting that k-means clustering as applied within this work may not be best suited to differentiate diseased cells from healthy cells. Although tested on a small number of samples, <100, the ability for simple pre- and post-processing machine learning algorithms demonstrates the future for clinical diagnostics of wounds and subsequent wound healing procedure. These methods are not only applicable to wound relevant spectra, but for all spectral analysis problems where subtle spectral differences are undetectable using simple observation or classical techniques. This work has highlighted the ability to gain additional information for wound healing diagnosis by considering a broad range of imaging wavelengths. With the limitations of the NCI, as described previously, combined with benefits from additional spectral information from a broad spectral range, the remaining results chapters will consider a different imaging modality, focused in the NIR-SWIR range, Spatial Frequency Domain Imaging.

Chapter 5

5 Applications of Compressive Sensing in SFDI Analysis

Whilst Chapters 3-4 focused upon SWIR/MWIR based imaging modalities, through the use of advanced spectral analysis and a novel Negative Contrast Imaging device, this work also highlighted the merit of using further wavelengths for additional information to aid in wound assessment. As discussed in Chapter 2, many imaging modalities used within wound diagnostics and assessment are based within the NIR range. These methods utilise the optical properties of haemoglobin and water to gain further information about the tissue's health. Of these methods, SFDI has been chosen due to both its versatility in adaptations for specific imaging requirements, along with its accessibility through both open-source methodologies and low set up costs [171]. Section 2.2.6 discusses the use of SFDI in the field of wound healing, where it is regularly applied to wounds such as burns and diabetic foot ulcers [84, 124]. This method provides non-invasive imaging within the NIR-SWIR range at high speeds (< 10 s), compared to the NCI, whilst also providing optical property depth information, such as wound tissue depth, from a given sample, which can be aid in the wound healing process [172]. Additionally, no sample preparations are required for SFDI capture, providing a suitable in-situ methodology for both *in-vivo* and *in-vitro* applications. SFDI can be used to rapidly and repeatedly assess wounds for both healing progression and effects of treatment, providing a quantitative assessment tool.

Although a brief introduction to SFDI has been provided in section 2.2.6, this chapter will provide a more thorough introduction to SFDI, before presenting a series of new image collection and processing methodologies, through the application of CS algorithms for data reduction applications. This work has been published in the Journal of Biomedical Optics under the title *'Applications of compressive sensing in spatial frequency domain imaging'* [173].

5.1 Introduction

Spatial frequency domain imaging (SFDI) is a form of diffuse optical imaging, traditionally performed within the visible/near-infrared (VIS/NIR) range [174]. This method projects spatially modulated light in the form of sinusoidal patterns onto a sample of interest to produce maps of absorption, μ_a, and reduced scattering, μ'_s, via images collected from two different spatial frequencies and three phases. If collected at more than one wavelength, tissue constituent maps can be derived for properties including oxy- and deoxy-haemoglobin, oxygen saturation, lipid content, and water [175].

Advances to SFDI have focused mainly upon the instrumentation and data acquisition. The wavelengths used by the system can be optimized for the samples of interest and have been extended beyond the VIS/NIR range [176, 177]. Multiple wavelengths can be imaged simultaneously using more than one monochrome camera or with temporally modulated illumination, both reducing the imaging time required [175, 178]. While these methods still use the two spatial frequencies and three phases, the single snapshot of optical property (SSOP) method requires only one illumination image at a non-zero spatial frequency, by performing the initial

image analysis directly in the frequency domain, increasing the acquisition rate by six-fold as a form of data acquisition improvement [179].

Both instrumentation and data acquisition improvements have been demonstrated previously with the application of CS [180], where the detection optics are changed to a single-pixel detector and a DMD to display the random pattern for each measurement, along with multiple LED illumination, to determine the tissue optical properties. This application to SFDI, named cs-SFDI, was used to measure the optical properties of a simple tissue-mimicking phantom with a cylindrical anomaly and compared to those obtained from a traditional SFDI measurement. The aim of this study was to reduce the number of measurements required to obtain the raw SFDI images, while also collecting three different illumination wavelengths simultaneously, working toward multi- and hyperspectral SFDI, without the use of expensive hyperspectral cameras [181]. The raw images for each wavelength were reconstructed using the denoising-based approximate message passing CS algorithm and analysed using the traditional pixel-by-pixel SFDI procedure to obtain optical property maps for both μ_a, and μ'_s. These maps were compared to those collected using a conventional camera-based SFDI method for two regions of interest, corresponding to the central anomaly and background of the tissue-mimicking phantom. The percentage difference between the recovered optical properties for these two SFDI methods was <10% for an ~90% reduction in measurements, with only 400 measurements required compared to the full 4096 pixels for the camera-based SFDI. This lower measurement number is a form of data reduction, reducing the data size required to collect multiple wavelength measurements and the full image field of view.

Whilst this highlights a novel image acquisition process for SFDI, the study is limited by the low heterogeneity of the tissue-mimicking phantom. This increases the sparsity of the data set and hence reduces the number of patterns required to reconstruct an accurate image. The next step for the cs-SFDI method is to consider an increased heterogenic sample. The heterogeneity is defined as the increased variation of the spatial distribution and the corresponding contrast of the optical properties for both absorption and reduced scattering. This is performed using biological samples imaged with clinical SFDI measurements, to determine any possible data reduction and reduced measurements for the pixel-by-pixel detection for a reduced sparse sample. The parameter recovery algorithm is also performed in a pixel-wise manner; therefore, CS applications may also be tested here.

CS has also been used for further biomedical imaging modalities, DOT and bioluminescent imaging through the use of single-pixel detectors to reduce the number of measurements [182, 183]. A multiple view DOT/fluorescence molecular tomography system, which has two DMDs for illumination and acquisition, uses structured illumination and compressive detection to collect data that has good agreement with the traditional CCD method [184]. Within the field of compressive fluorescence lifetime imaging, different compressive basis patterns have been assessed, including Fourier and Hadamard, and CS has been used for time-resolved hyperspectral imaging [185, 186].

The aim of this chapter is to apply and test CS methods to both the SFDI image acquisition and analysis stage for the purposes of data reduction, improved computation time while maintaining accuracy on a realistic dataset. The cs-SFDI methodology has been simulated using the AppSFDI data set [187], consisting of

an increased heterogenic sample to validate this method, with the results showing that an increased number of measurements are required to accurately obtain optical property maps, although a reduction in data is still possible. Additionally, the parameter recovery algorithm has also been performed within the compressed state, and optical property maps were obtained for the App SFDI data set with an error of <10% for a data reduction of up to 80%. Overall, these methods show that the use of CS within multi stages of the SFDI imaging modality can greatly reduce the data required to accurately obtain optical property maps.

5.2 Methods

5.2.1 Spatial Frequency Domain Imaging

SFDI has been used for both research and clinical imaging for over 10 years [79]. The theoretical background, instrumentation, data acquisition methods, and processing steps have been thoroughly described previously [174]. In SFDI, spatially modulated light patterns are projected onto a region of interest in the VIS/NIR range. The illumination consists of sinusoidal incoherent monochromatic light patterns at specific frequencies and three different phases. The diffused backscattered light is collected and processed to determine the reflectance at each specific wavelength and spatial frequency. This is then further separated into absorption, μ_a, and reduced scattering, μ'_s, using a light propagation model, including Monte Carlo simulations or analytical solutions. A breakdown of the three key steps is shown within Figure 5.1 (a).
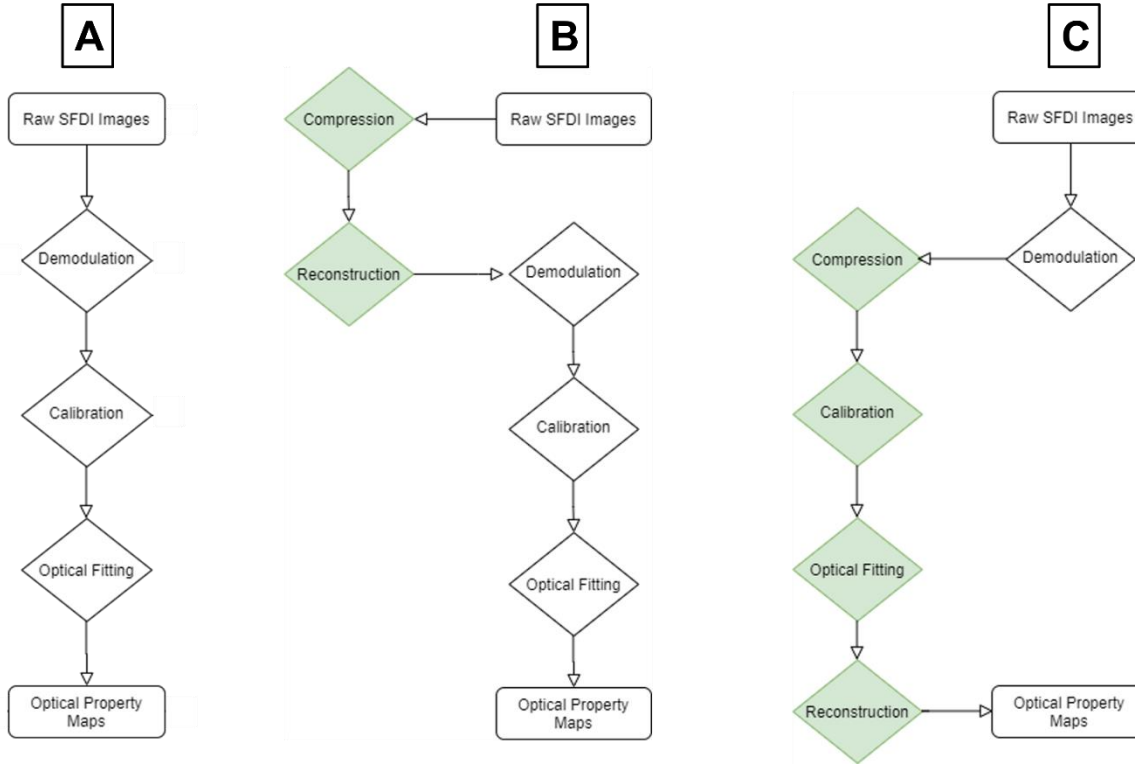
Figure 5.1: SFDI analysis workflows. (a) Traditional three-stage workflow. (b) cs-SFDI based workflow, here, raw images are compressed and reconstructed to simulate single-pixel detection, before following the traditional workflow. (c) CS-based parameter recovery algorithm, here, the demodulated images are compressed before both calibration and optical fitting are performed in the compressed space before image reconstruction to generate the optical property maps.

To obtain the optical property maps of both μ_a and μ'_s, data from at least two different spatial frequencies are required. It has been shown that low frequencies are sensitive to changes in μ_a while higher frequencies are sensitive to μ'_s [79]. Therefore, it is common for SFDI measurements to be taken at spatial frequencies of 0 and 0.2 mm^{-1}, as optimized in a previous study [174]. These two frequencies allow for the DC and AC demodulated images to be collected from the three different phase measurements, using Equations 5.1 and 5.2, respectively:

$$DC(x,y) = \frac{1}{3} \cdot \{I(x,y,\phi_1) + I(x,y,\phi_2) + I(x,y,\phi_3)\} \tag{5.1}$$

$$AC(x,y) = \frac{\sqrt{2}}{3} \cdot \left\{ \begin{array}{c} [I(x,y,\phi_1) - I(x,y,\phi_2)]^2 + [I(x,y,\phi_2) - I(x,y,\phi_3)]^2 \\ + [I(x,y,\phi_3) - I(x,y,\phi_1)]^2 \end{array} \right\}^{1/2}, \tag{5.2}$$

where the three phase values, ϕ, are 0, $2/3\pi$, and $4/3\pi$. These demodulated images then undergo a calibration against phantom images. These phantom images, of a set of known optical properties, are used alongside a forward model to correct for any instrument response using Equation 5.3:

$$I_{CALIB}(x, y, f_x) = Pred(f_x)\frac{Samp_{DEMOD}(x,y,f_x)}{Phan_{DEMOD}(x,y,f_x)},\qquad(5.3)$$

where $Pred(f_x)$ is the model reflectance from the photon propagation model, resulting in the pair of calibrated images from the two different spatial frequencies. $Samp_{DEMOD}$ and $Phan_{DEMOD}$ correspond to the sample and calibration phantom demodulated image respectively. With a set of calibrated images, a variety of methods can be used to determine the samples optical properties using the inverse model, including least-square methods and look-up tables, calculated from Monte Carlo simulations.

5.2.2 Compressive Sensing

Consider a 2D image of N pixels, which can be represented as a $N \times 1$ vector, x. This vector can be represented as a combination of its orthonormal basis,

$$x = \sum_{i=1}^{N} \Psi_i s_i = \Psi s,\qquad(5.4)$$

where Ψ is the transform operator and s an $N \times 1$ vector of weight coefficients.

Compressive sensing theory states that the signal, x, can be reconstructed using $M \ll N$ patterns, with the sensing matrix $\Phi_{M \times N}$ via the measurement vector,

$$y = \Phi x = \Phi \Psi s,\qquad(5.5)$$

where y is the reconstructed image. This sensing matrix is composed of 1's and 0's (Fig. 2), in the form of a Bernoulli distribution to generate random patterns of N pixels per pattern, although other patterns such as Hadamard, wavelet, and speckle

patterns can be used, and the data are then represented in the basis where the signal is most sparse [182].
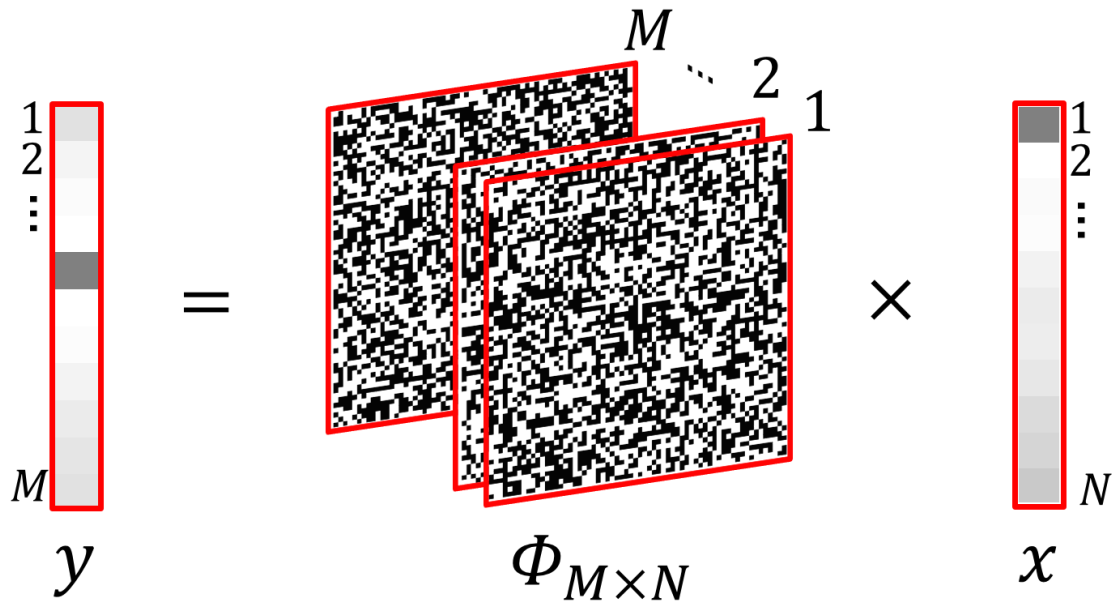
Figure 5.2: Compressive sensing visualisation. Representation of Equation 5.5. The measurement vector y is calculated by multiplying the sensing matrix, $\Phi_{M \times N}$, by the image vector x, reducing the dimensionality of the data to $M \ll N$ values.

Within this sparse space, the image vector x is represented as a linear combination of K basis vectors, where $K \ll N$. These bases included discrete Fourier transform, wavelet, and discrete cosine transform, which are used in common image compression applications such as JPEG-2000, with the discrete cosine transform used for this study.

With the measurement vector and basis for representation defined, the final step is the reconstruction to recover the image x. Several different minimisation methods can be used including l_2-norm, l_0-norm and l_1-norm reconstruction algorithms. l_2-norm is not suitable in seeking K-sparse solutions, instead almost always finding a nonsparse $\hat{s}$ solution, while the l_0-norm is both numerically unstable and NP-

complete, hence difficult to minimise [188]. Therefore, to then reconstruct the original signal x, a solution to the l_1-norm minimisation problem is required:

$$\hat{s} = min \sum_j \left\|s_j\right\|_1 \ such \ that \ \Phi\Psi s = y \qquad (5.6)$$

using the sensing matrix and transform operator as discussed previous, with the full image then reconstructed using,

$$\hat{x} = \Phi\hat{s}. \qquad (5.7)$$

5.2.3 cs-SFDI

Previous cs-SFDI applications have been based upon modifications to the detection side of equipment setup. The image detection camera is replaced with a DMD to display the sensing matrix patterns, with the reflected light from the DMD focused upon the single-pixel photodetector. The measurement matrix is therefore collected directly and the images for each of the frequencies and phases are reconstructed before the traditional analysis process of demodulation, calibration and optical fitting are performed to generate the optical property maps.

To test this methodology upon an increased heterogenic sample, an open source data set from the University of Strasbourg was utilized [187]. AppSFDI is a software package for analysis of SFDI images and contains a sample data set of images from both a tissue mimicking phantom and a biological sample of interest. To simulate the cs-SFDI detection for these images, each image was converted to the signal matrix x from Equation 5.4 and multiplied by the full sensing matrix Φ, resulting in a measurement vector, y, for each image within the AppSFDI data set.

The raw images were then reconstructed using l_1-minimisation and Equation 5.7. As with the previous study, these reconstructed images were then processed using

the traditional analysis procedure, performed as a pixel-by-pixel calculation, outlined in Figure 5.1(b). The resulting optical property maps from an increasing number of patterns used, were compared to those that were collected using the non-compression-based method shown in Figure 5.1(a).

5.2.4 cs-Based Parameter Recovery Algorithm

While the cs-SFDI method addresses the issue of pixel-wise detection, the analysis procedure is also performed in a pixel-by-pixel manner, and hence, CS methods can also be applied to these steps. Figure 5.1(c) shows a compression-based analysis procedure, with both the calibration and parameter recovery performed within the compressed state. During the demodulation step (Equations 5.1 and 5.2), the pixel-by-pixel calculation is no longer linear, making the application of CS non-trivial, although additional demodulation methodologies or CS for non-linear applications are areas for future study [189]. Therefore, for this study, the use of previously demodulated images was chosen to demonstrate the application of CS for the linear stages of the image analysis and parameter recovery.

In this process, the demodulated images from the two spatial frequencies used within the AppSFDI data set, 0 and 0.2 mm^{-1}, are compressed using Equation 5.5 forming the two measurement vectors. These vectors are then normalized to the number of "on" pixels within each pattern of the sensing matrix Φ. This process is repeated for the phantom images before both the calibration, using Equation 5.3, and the optical fitting is performed. The normalization is then reversed before the optical maps of μ_a and μ'_s are reconstructed using the same procedure as outlined in the cs-SFDI method. Once again, these maps are compared to the non-compressed method for a variety of pattern numbers.

116

5.2.5 App SFDI Data Set

The field of SFDI has been proactive in moving toward open source methodologies, with Open SFDI providing full details of an open hardware system, while AppSFDI has produced software and MATLAB code to analyse SFDI images for a variety of methods [171, 187]. Within the AppSFDI software package, a typical data set of images is provided for testing and validating analysis methods and algorithms, with these images used for this study. The use of open access images for analysis comparison is common within other fields, such as hyperspectral imaging for remote sensing, with data sets such as Indian Pines and Salinas valley [190]. A variety of different algorithms have been applied to these data sets over the past 25 years and can be easily compared due to the same test data across many publications. This was the motivation for using the AppSFDI data, which although contains only the one sample (back of the hand) and one phantom for calibration, comparisons can still be made with any future advanced analysis method.

5.2.6 Error Calculations

In order to quantify the error between each different compression-based reconstruction method, the Root Mean Squared (RMS) error between the non-compressed and reconstructed optical property maps was calculated using the following equation:

$$RMS = \sqrt{\frac{\sum(\bar{A}-\bar{B})^2}{N}} * 100, \qquad (5\ 8)$$

where $\bar{A}$ and $\bar{B}$ are the reconstructed and non-compressed original optical property maps of absorption or reduced scattering respectively. Each of these images is

normalised against the maximum pixel values for the non-compressed image. Similarly, the RMS error on an individual pixel basis can be calculated via:

$$RMS\_Pixel = \sqrt{(\overline{A_i} - \overline{B_i})^2} * 100, \qquad (5.9)$$

where $\overline{A_i}$ and $\overline{B_i}$ are each reconstructed and non-compressed optical property map pixel respectively, which are again normalised against the maximum values for the non-compressed image.

5.3 Results

The cs-SFDI application, where each of the raw images from within the AppSFDI data set was compressed and reconstructed, was applied to a varying number of patterns. Each resized 64 by 64 pixel image requires 4096 individual pixel values to create the full image within the traditional imaging modality. A full sensing matrix is therefore represented by 4096 patterns, and a reduction in measurements is performed using less patterns, i.e., 2048 patterns is a 50% reduction in measurements. The cs-SFDI process was performed upon the AppSFDI data for 820-3686 patterns, representing up to a 90% reduction in measurements required, at 10% reduction intervals. Figure 5.3 shows the optical property maps for a selection of pattern numbers along with a ground truth obtained through the traditional SFDI analysis process.

Absorption μ_a **(mm^{-1})**   **Reduced Scattering** μ_s' **(mm^{-1})**

Uncompressed   **Uncompressed**

410 Patterns   **410 Patterns**

1229 Patterns   **1229 Patterns**

2048 Patterns   **2048 Patterns**

2867 Patterns   **2867 Patterns**

3686 Patterns   **3686 Patterns**

0.01   0.03   0.05   0.5   1   1.5

Figure 5.3: cs-SFDI image panel. Comparison between the original data and reconstructed images for increasing pattern numbers.

119

Full RMS values for both μ_a and μ'_s are shown in Figure 5.4. As expected, an increase in the number of patterns used reduces the RMS error, while a greater number of patterns are needed due to the increased heterogeneity than that observed in previous studies [180].
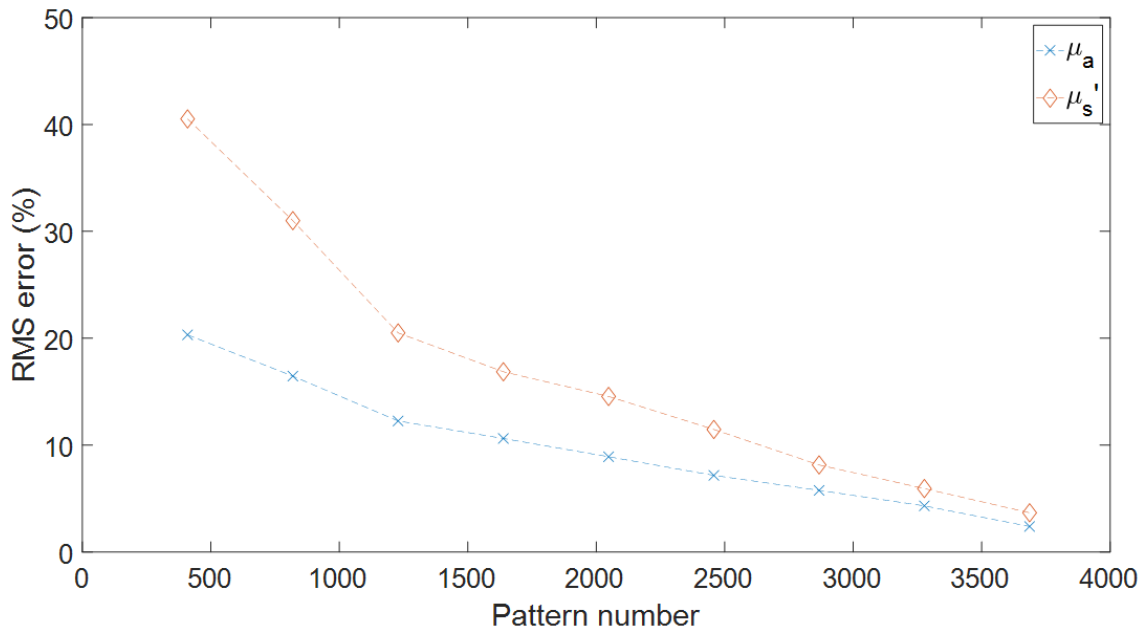
Figure 5.4: cs-SFDI RMS error results. RMS error for each optical property map obtained using the cs-SFDI algorithm, compared to the non-compression based ground truth results.

While the cs-SFDI method has been previously tested with more homogenous two-tone tissue-mimicking phantoms, the parameter recovery algorithm CS method has not been previously studied for SFDI. Phantom measurements can be simulated using the analytical model from Cuccia and colleagues [174] as used in the calibration step, to generate the demodulated DC and AC images from the 0 and 0.2 mm^{-1} spatial frequencies used within the AppSFDI data. These simulated data sets are also 64 by 64 pixels in size and contain three different optical property anomalies. The background pixel values have optical properties of $\mu_a = 0.01$ mm^{-1} and $\mu'_s = 1$ mm^{-1} with an anomaly varying each of μ_a and μ'_s, and the final anomaly

varying both (Figure 5.5). The optical properties of the anomalies were increased by 50% compared to the background, and an unchanged phantom of purely background values was generated for the calibration step of the SFDI analysis procedure.
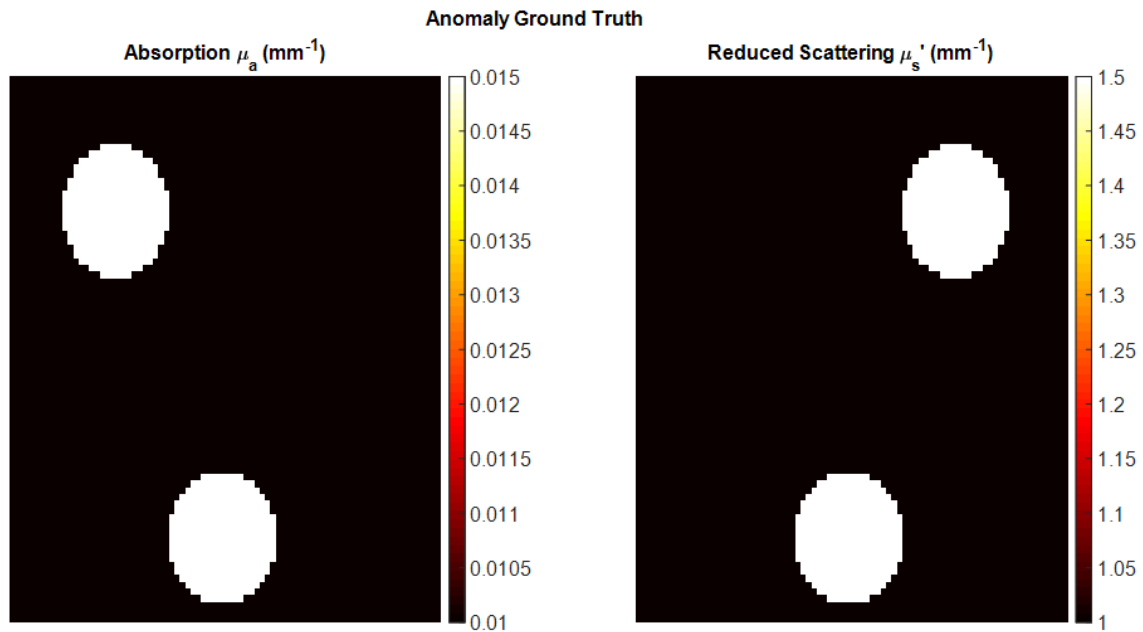
Figure 5.5: Analytical anomaly ground truth maps for the CS parameter recovery phantom test.

These images were then compressed using the same pattern numbers, following the analysis workflow shown in Figure 5.1. The resulting reconstructed images and RMS errors are shown in Figure 5.6 and Figure 5.7, respectively.
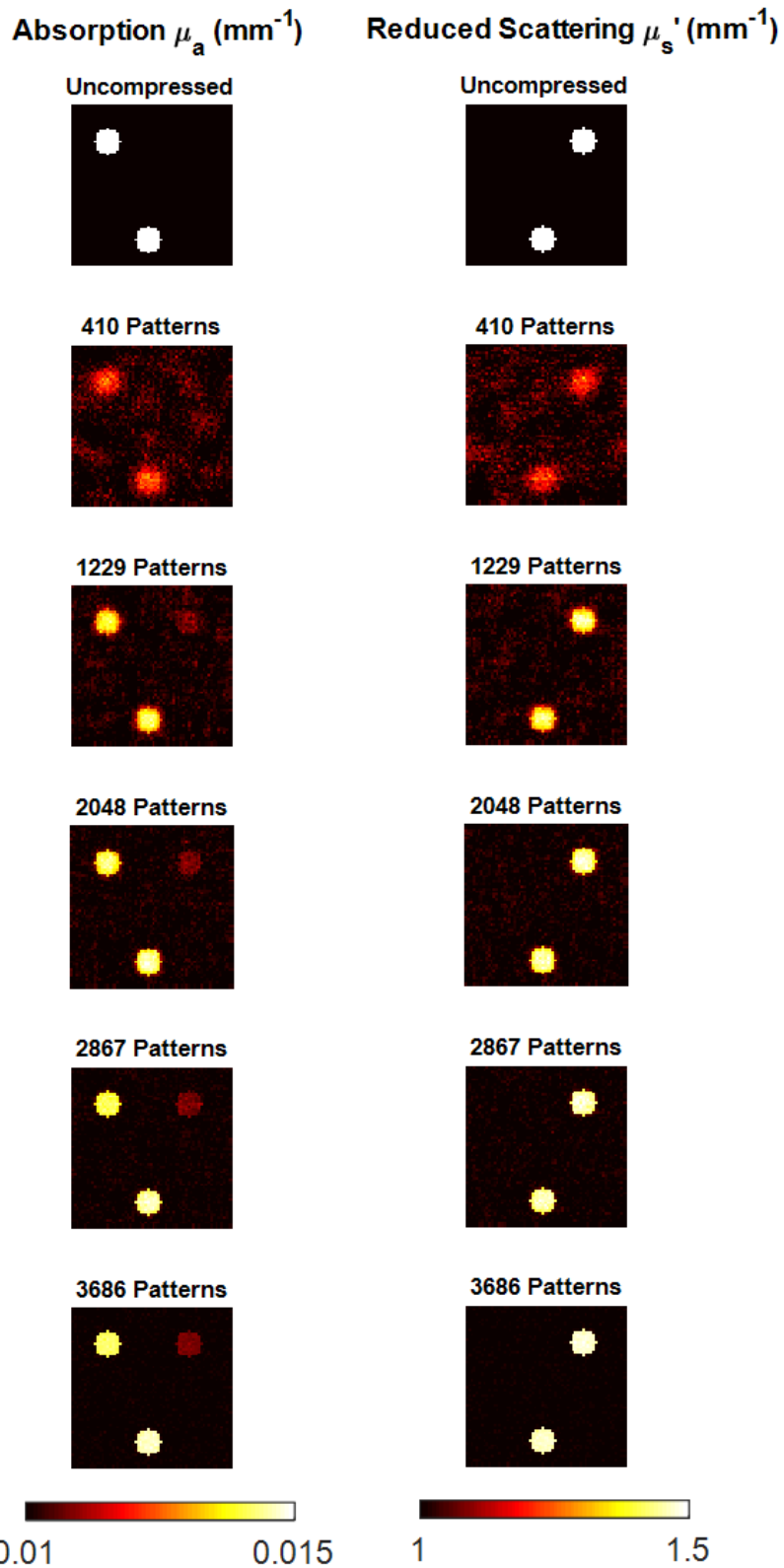
Figure 5.6: Simulated data CS parameter recovery algorithm image panel. Comparison between the original data and reconstructed images for increasing pattern numbers.
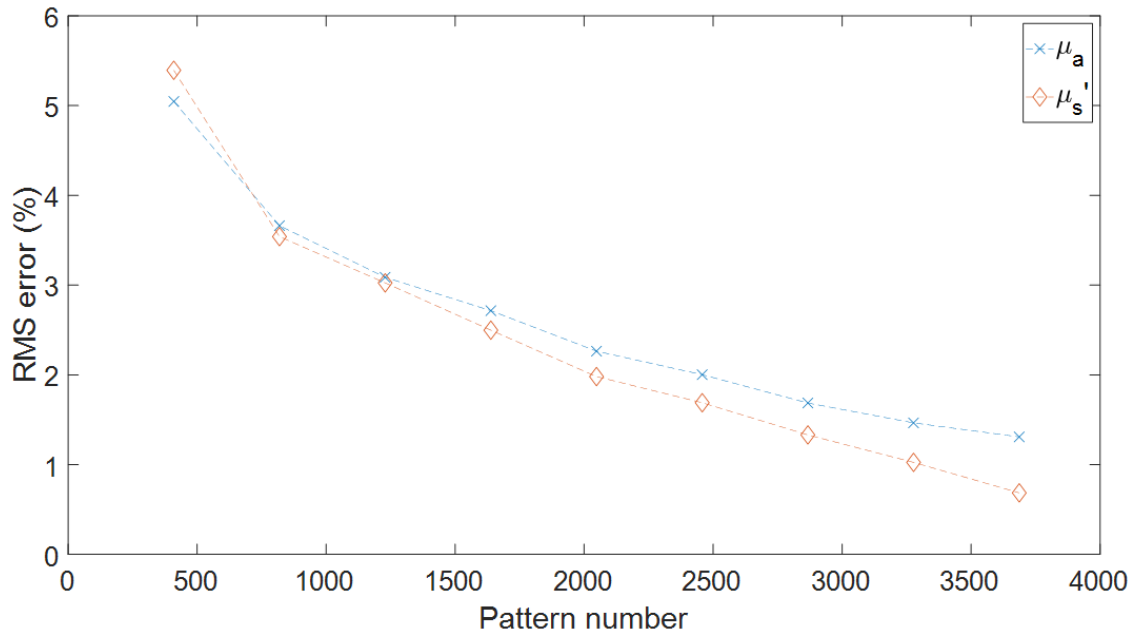
Figure 5.7: Simulated data CS parameter recovery algorithm RMS error results. RMS error for each optical property map obtained using the data CS parameter recovery algorithm, compared to the non-compression based ground truth results.

The CS-based parameter recovery algorithm was then tested further using the AppSFDI data once again. As with the other applications, pattern numbers were chosen to represent a data reduction of up to 90%, in 10% steps. A sample of the reconstructed images for both μ_a and μ'_s are shown in Figure 5.8, and the resulting RMS error for the different pattern numbers in Figure 5.9.

Absorption μ_a **(mm^{-1})**

Reduced Scattering μ_s' **(mm^{-1})**

Uncompressed

Uncompressed

410 Patterns

410 Patterns

1229 Patterns

1229 Patterns

2048 Patterns

2048 Patterns

2867 Patterns

2867 Patterns

3686 Patterns

3686 Patterns

0.01 0.03 0.05

0.5 1 1.5

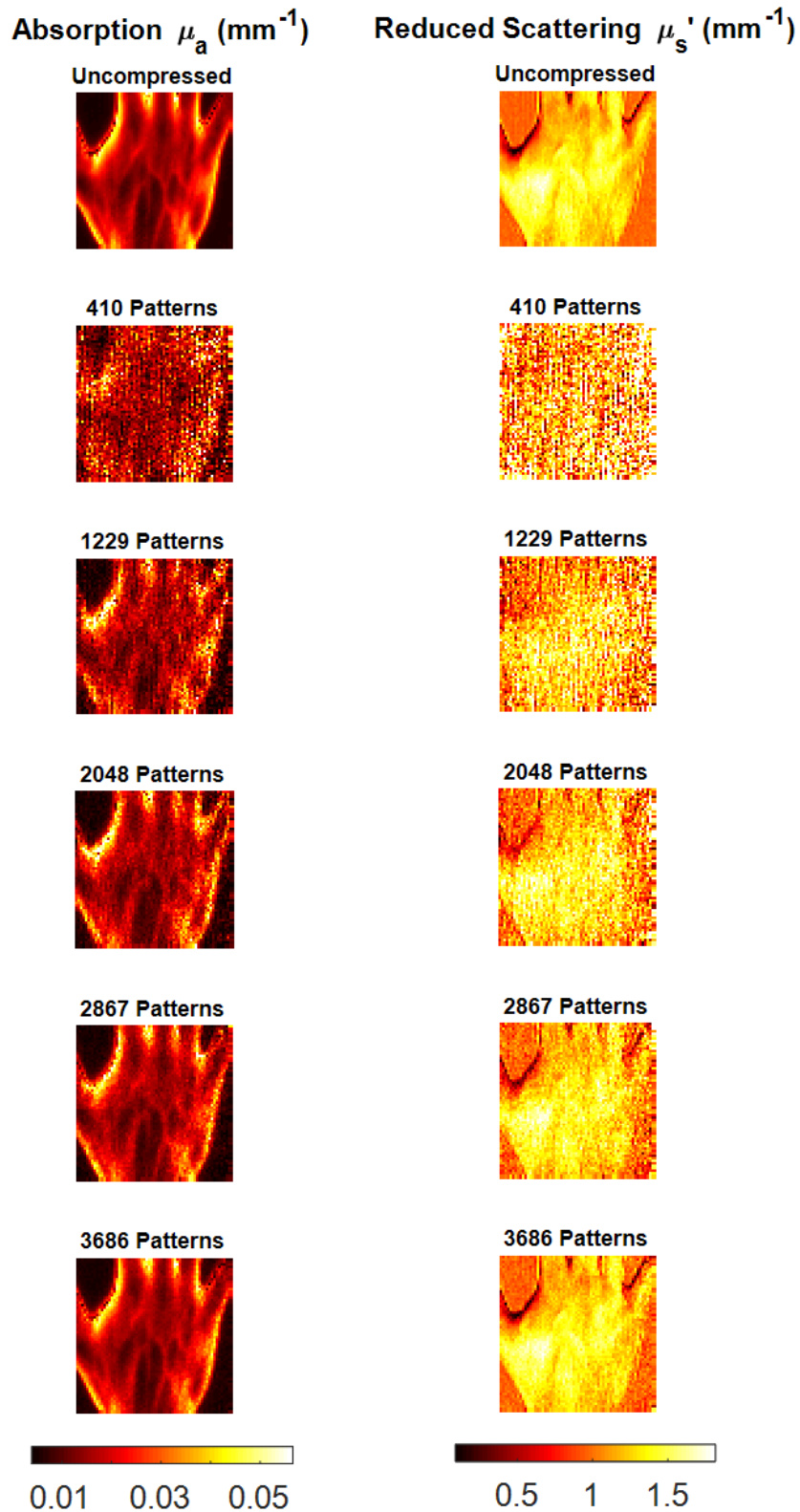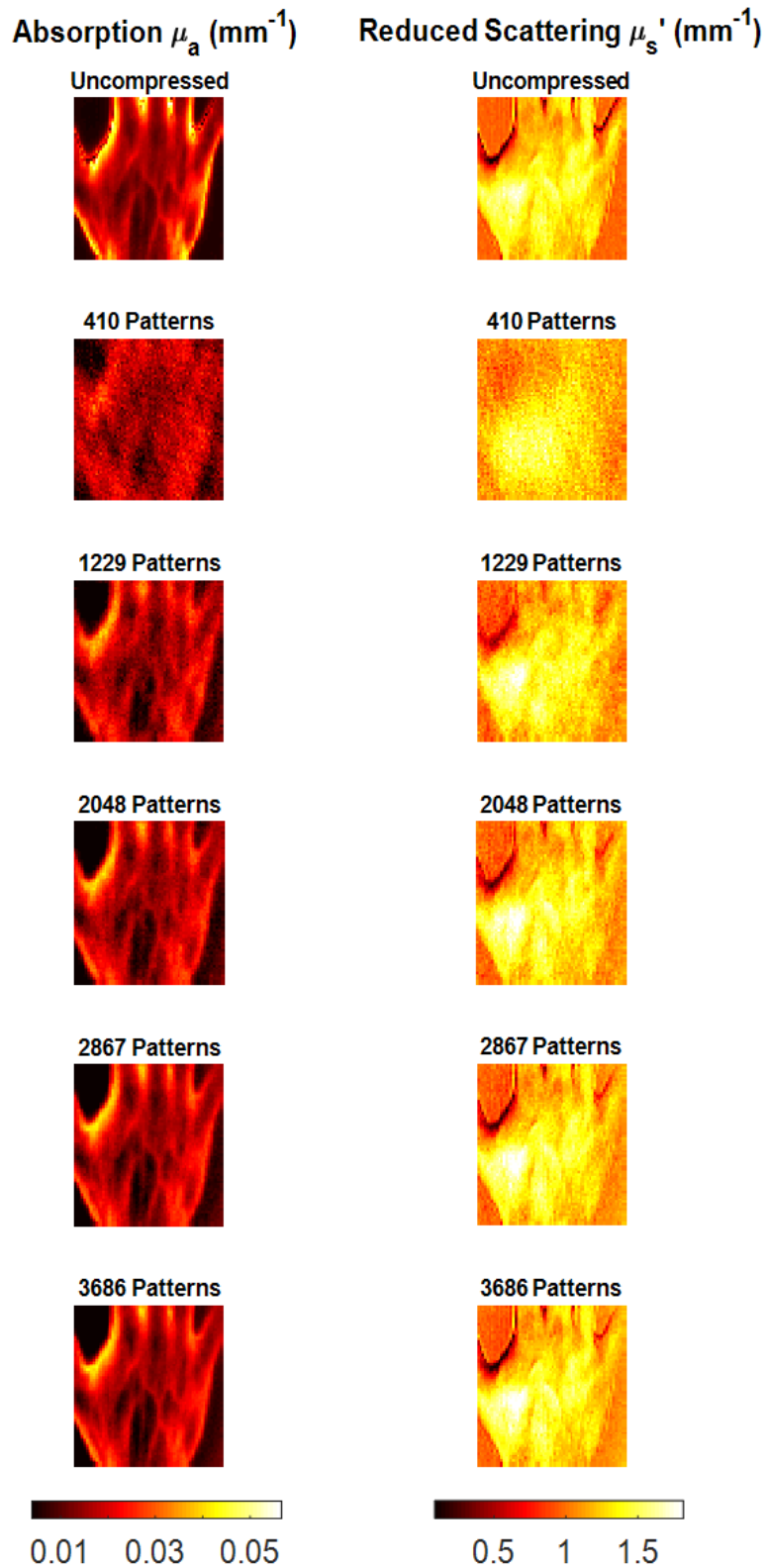*Figure 5.8: AppSFDI CS parameter recovery algorithm image panel. Comparison between the original data and reconstructed images for increasing pattern numbers.*
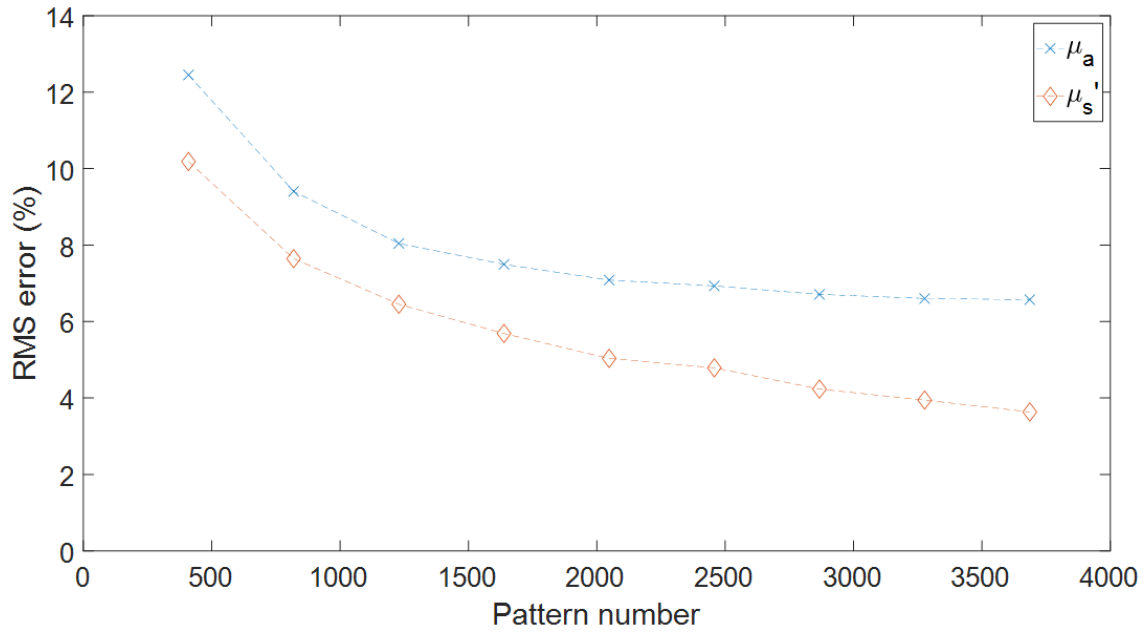
Figure 5.9: AppSFDI CS based parameter recovery algorithm RMS errors. RMS error for each optical property map for the cs based parameter recovery algorithm, compared to the non-compression-based ground truth results.

5.4 Discussion

Through the application of CS methodology to the SFDI process, the number of measurements required to accurately reconstruct optical property maps can be reduced. For the cs-SFDI algorithms, where the collection of compressed data is simulated for comparison to previous studies [180], the RMS error for both absorption and reduced scattering (Figure 5.4) is <15% for 2048 and <10% for 2867 patterns, representing a data reduction of 50% and 30%, respectively. While the original study showed a data reduction of 90% still obtained the optical properties within 10% error, this was taken using a simple two-tone phantom, which will have a much greater sparsity than the hand sample used in this study. Therefore, the number of patterns required, and hence, the level of data reduction achieved will always be lower with a data set that contains greater sparsity. However, this does

not represent the complex samples that are imaged using SFDI both within research and clinical settings, such as burn wounds or pressure ulcers [81] [84].

While the cs-SFDI application, with the data collected directly in the compressed state, addresses data reduction for the raw images, these images are still reconstructed to full size and each pixel is analysed to produce the optical property maps. The CS-based parameter recovery algorithm applies CS to the analysis stage, reducing the number of calculations required to obtain these maps. Phantom simulations were performed using the analytical solution to the diffusion approximation, as developed by Cuccia *et.al* [174]. As the same solution is used for the parameter recovery algorithm, any resulting RMS error is from the compression algorithm only. For all patterns tested the RMS error was below 6% for both μ_a and μ'_s, while each of the anomalies was clear (Figure 5.6) for even the lowest pattern number tested, 410, representing a data reduction of 90%. While this demonstrates a further application of CS to SFDI, and a novel methodology for obtaining the optical property maps, as with the cs-SFDI technique, however, the heterogeneity of the sample is low compared to research and clinical applications of SFDI. The AppSFDI data set was again used, with the hand sample showing an increased heterogeneity and analysed using the procedure shown in Figure 5.1(c).

Although an RMS error of <15% is observed for the lowest pattern number tested, 410, it is clear from Figure 5.8 that the sample is not distinguishable and any regions of interest, such as the veins on the surface of the hand, cannot be resolved. However, an RMS error of <10% is calculated for all subsequent pattern numbers, and the features of the hand sample are visible from 1229 patterns as shown in Figure 5.9 These maps were calculated using a 70% reduction in parameter

recovery calculations, producing a significant data reduction compared to the full uncompressed analysis procedure. Additional data reduction methods have been previously applied in the form of pixel binning [191]. Such pixel binning method could also be applied in conjunction with the CS algorithms used within this work, although maintaining original single-pixel values for reconstructions preserves the resolution and contrast of the original images, validating the contribution of CS for data reduction purposes as compared to other methodologies.

A pixel-wise RMS map calculated using Equation 5.9, for both absorption and reduced scattering, demonstrates the locations upon the hand sample corresponding to the greatest error (Figure 5.10). The pixels with the highest error, >40%, align with the edge regions of the hand and background, where the greatest variance in optical property values occur. Within traditional SFDI image reconstruction, edge detection errors are common due to the challenges faced by surface curvature and discontinuity errors related to model-based assumptions of the technique, which can be addressed through the use of profilometry correction methods [78]. However, for this study, the ground truth values and corresponding error calculations are performed against the recovered images as determined from traditional methods and not the tissue ground truth values themselves. Therefore, the edge errors observed are due to a caveat of the l1-norm minimization by which the edges and boundaries of the largest optical property gradients are oversmoothed, producing the larger error compared to the ground truth maps.

Absorption   **Reduced Scattering**
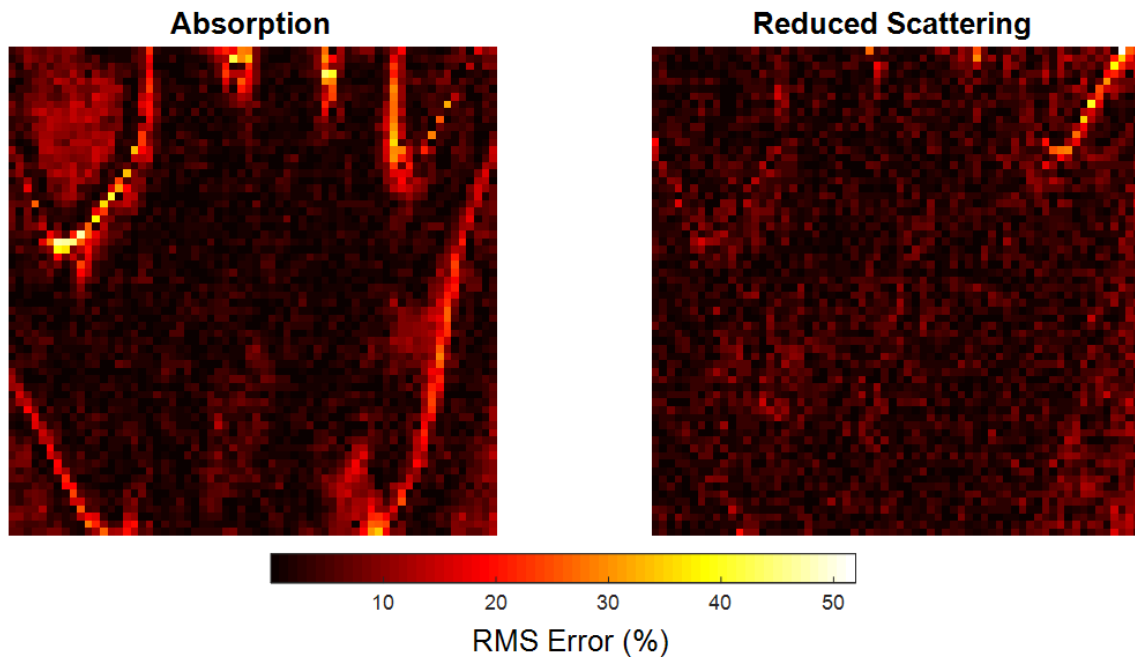
RMS Error (%)

Figure 5.10: Pixel-wise RMS error for 50% measurement reduction using the CS parameter recovery algorithm.

Additional reconstruction algorithms, such as total variation regularization are known to produce sharper images due to the improved boundary preservation, although are more computationally difficult and will be considered in future studies [183]. The AppSFDI data set only contains images of a single wavelength, therefore limiting the possible benefit of CS approaches. From optical property maps at multiple wavelengths, quantitative maps of tissue properties such as oxy- and deoxyhaemoglobin can be produced, therefore, SFDI is most commonly used for two or more wavelengths. Traditionally, this has required illumination using multiple sources, each of an individual wavelength, increasing the number of measurements required, and hence the number of pixel-wise analysis calculations. Commercial systems, such as the Reflect RS™ from Modulim, contain nine different LEDs, and other systems contain multiple wavelengths based on previously optimized values for obtaining different tissue property maps [176]. While it is possible to obtain these maps for only two wavelengths, the wavelength optimization performed is highly

dependent on the assumed tissues properties, and therefore limited in the range of biological samples they can accurately obtain. Therefore, with the use of additional wavelengths, the number of calculations required to fit for both μ_a and μ'_s at each individual pixel and wavelength increases, and hence the data size. The application of the CS-based parameter recovery algorithm would reduce the number of calculations required by up to 70% as previously stated, which would also propagate across each wavelength used.

5.5 Conclusion

While CS has been applied to SFDI previously, this study has highlighted an additional application during the parameter recovery stage alongside the use of the cs-SFDI algorithm on increased heterogenic data, as seen within clinical applications. It has shown that the number of measurements required, while still maintaining an optical property error of <10% can be observed with as much as a 90% data reduction during the parameter recovery stage. Due to the increased heterogenicity, and hence, sparsity of the sample the cs-SFDI application to the image acquisition stage only provides a data reduction of 30%, however, current advanced imaging methods, such as SSOP, already greatly reduce the data required during the initial image acquisition. Overall, these CS-based SFDI methods provide a novel application toward data reduction and merit further investigation upon physical samples working toward multi- and hyperspectral SFDI systems.

The limitation of accurate edge detection for SFDI parameter recover has been briefly mentioned within this chapter. This issue is described further in the subsequent and final results chapter, in which further SFDI improvements are investigated, through the use pixel dependent modelling tools.

Chapter 6

6 Numerical Methods for FEM based SFDI simulations

Chapter 5 introduced the concept of applying compressive sensing methodologies to improve spatial frequency domain imaging. This work demonstrated the application of data reduction techniques throughout the SFDI processing timeline; however, these methods still rely upon either diffusion approximation or Monte Carlo based inverse solver methods for parameter recovery. Whilst these methods provide accurate results for homogenous samples, when considering both sample geometry and optical properties, increased recovery errors are obtained for heterogenous models. Conventionally, both forward modelling and optical property recovery are performed using pixel-independent models, calculated via analytical solutions or Monte-Carlo based look up tables, both assuming a homogenous medium. The resulting recovered maps are limited for samples of high heterogeneity where the homogenous assumption is not valid. Here, a full raw image SFDI modelling tool is presented for heterogeneous samples, providing a mechanism towards a pixel dependent SFDI image modelling and parameter recovery system. As discussed in previous chapters, the complex nature of the wound healing produces a complex environment of varying biological and chemical processes. This then creates heterogeneity across a wound bed, therefore reducing the ability of methods, such as SFDI, to accurately identify the optical properties across the whole wound. Improved detection at the wound boundary will allow for a more accurate

removal of apoptotic/necrotic tissue, whilst reducing the amount of heathy tissue also removed.

This chapter presents the pixel-independent models currently used, whilst further highlighting their limitations. A pixel-dependent approach for forward modelling is described, through the adaption of NIRFAST, an existing FEM based NIR modelling tool. This work has been published in Photonics titled *'A pixel dependent Finite Element model for spatial frequency domain imaging using NIRFAST'* [192].

6.1 Introduction

The field of SFDI has advanced through improved instrumentation, such as single snapshot optical properties methodologies, and analysis procedures including compressive sensing applications [79, 173, 193]. Further details of these advancements are discussed in section 5.1. Current forward models for SFDI simulation have been limited, with no tools available for the prediction and modelling of complex heterogeneous samples, although Monte-Carlo based models have addressed patterned illumination for other applications [194, 195].

Both the analytical model initially developed for SFDI and Monte Carlo simulations are based upon a pixel-independent methodology, with each pixel analysed in isolation, to extract the optical properties in a pixel wise manner. This limits the accurate analysis of complex and heterogeneous samples, with errors increasing at boundaries of varying optical properties. This is of particular importance in many biological applications, such as wound debridement surgeries, where the accurate localization of healthy and necrotic tissues for removal affects the overall healing outcome. Excessive healthy tissue removal can cause prolonged healing along with

excessive scarring, whilst the failure to remove all damaged or necrotic tissue can be fatal. The single pixel modelling methodologies have been developed through dual layer inverse modelling, demonstrating improved parameter recovery through heterogeneous sample adaptations [196]. However, the modelling is still limited by the laterally independent nature of the full sample parameter recovery, which is again concentrated at the boundaries of varying optical properties and underlying heterogeneity.

Heterogeneous modelling tools have been developed for other imaging modalities, such as diffuse optical tomography. NIRFAST is a near-infrared FEM based MATLAB tool for the numerical modelling and image reconstruction within biological tissues [43]. NIRFAST has been utilized for both forward modelling, to optimize system design, along with inverse modelling for parameter recovery, and optimized for additional imaging modalities [183, 197, 198]. The FEM nature of NIRFAST allows for modelling of complex geometries alongside heterogeneous optical properties in a customizable manner.

In this work, NIRFAST has been modified to implement and introduce pixel-dependent forward modelling for SFDI applications. The customizability of the FEM meshes ensures accurate modelling of the spatial light patterns within the model, initially validated using homogenous samples, before moving towards a complex heterogeneous model of varying optical properties. This demonstrates the first of its kind SFDI forward modelling tool, outlining the first step towards pixel dependent SFDI for both forward modelling and increased accuracy for optical property parameter recovery.

6.2 Theory

6.2.1 SFDI

The underlying theory of SFDI is explained in full elsewhere, with a comprehensive review published in 2019 [1,6], therefore only a brief outline is given here. The initial equations for demodulation and calibration are shown in Chapter 5 (Equations 5.1-5.3), which generate a series of calibration images of a sample/region of interest. Once obtained, the final stage to calculate the optical property maps of the sample is through model-data fitting. A variety of methods can be used to determine the samples optical properties using the inverse model, including least-square methods and look up tables, however all these methods are based on a single pixel process, fitting individual pixels, one at a time through each 2D image. These models are typically the same models as those used for the calibration step, Equation 5.3.

In both the application of forward models for SFDI light propagation prediction and use of inverse solvers for optical property calculation, this pixel independent method creates increased error when applied to heterogeneous samples. Using the current approach, each pixel is assumed as a semi-infinite medium, and therefore the optical properties geometry or reflectance values from neighbouring pixels are not considered. Optically varying depth properties have recently been considered in a two-layered inverse model [196, 199], however most sophisticated methods are still based upon a Monte-Carlo semi-infinite homogenous medium to develop a look up table, which have been optimized for real-time image acquisition and analysis [200].

All reported approaches to date model illumination directly within the spatial frequency domain, with the analytical solution modelling the source intensity as:

$$q_o(z) = P_o\mu_s' exp(-\mu_{tr}z), \tag{6.1}$$

where P_o is the incident optical power, μ_{tr} is the transport coefficient which is equal to $\mu_a + \mu_s'$, where μ_a is the absorption, μ_s' is the reduced scatter and $q_o(z)$ is the depth dependent illumination source. This source intensity is dependent on both the depth within the sample and its optical properties, and is used alongside the frequency dependent spatial component to generate the plane wave source:

$$q = q_o(z)\cos(kx + \varphi), \tag{6.2}$$

where $k = 2\pi f$ for any given spatial frequency. However, in real world SFDI, the illumination source must be applied differently, as it is not possible to produce a negative illumination value. For an experimental setup, Equation 6.3 describes the illumination as used within real world SFDI, producing spatially modulated patterns which are constant in the y-direction:

$$S = \frac{S_0}{2}[1 + M_0 \cos(2\pi f_x x + \varphi)], \tag{6.3}$$

where S_0 is the illumination intensity and M_0 is the modulation depth.

6.2.2 NIRFAST

To represent SFDI within NIRFAST, customized meshes for the finite element model (FEM) have been developed and optimized for the forward modelling of a spatially varying illumination pattern, to ensure both numerical accuracy as well as an accurate representation of the illumination pattern, Equation 6.3. Each FEM mesh is made up of a series of nodal points (vertices) of varying densities to ensure an accurate demodulation process. To model the characteristic illumination patterns, a modification to Equation 6.3 was developed to account for the depth and optical property dependability of the analytical solution, Equation 6.4. Specifically, the source for each [x, y] coordinate is placed at the nearest node to a depth of $1/\mu_s'$ for

each point (z axis) within the illumination area. A series of detectors are modelled upon the reflectance surface to directly extract the resulting fluence, producing the 2D images of spatially modulated light models for demodulation, calibration and optical property recovery steps detailed previously.

6.3 Methods and Results

Development towards the spatial modulated light models was preformed through a step-by-step validation, from spatially resolved spectroscopy (SRS) models to the full 3D FEM with spatially varying structured illumination. Each step is explained with results provided in the following sub sections.

6.3.1 SRS semi-infinite model

The first step is to consider a simple SRS model using NIRFAST semi-infinite analytical model, validated against an existing analytical solution from virtual photonics (VP). This validation data is derived from the virtual photonics modelling software, in which the reflectance at given distance, $R(\rho)$ from a single isotropic point source located at a depth of l^*, the transport mean free path:

$$l^* = \frac{1}{\mu_{tr}} = \frac{1}{(\mu_a + \mu_s')}.$$

(6.4)

This solution is formed from the linear superposition of the infinite medium Greens function [201]. Detectors are located at a resolution of 0.2 mm to a maximum source detector separation of 100 mm. This configuration is repeated for the NIRFAST semi-infinite analytical model, which is performed using an analytical solution described previously [202]. The diffuse reflectance is plotted against the source-detector separation distance for a series of l^* values with a constant $\mu_s'/\mu_a = 100$ in Figure 6.1.

136
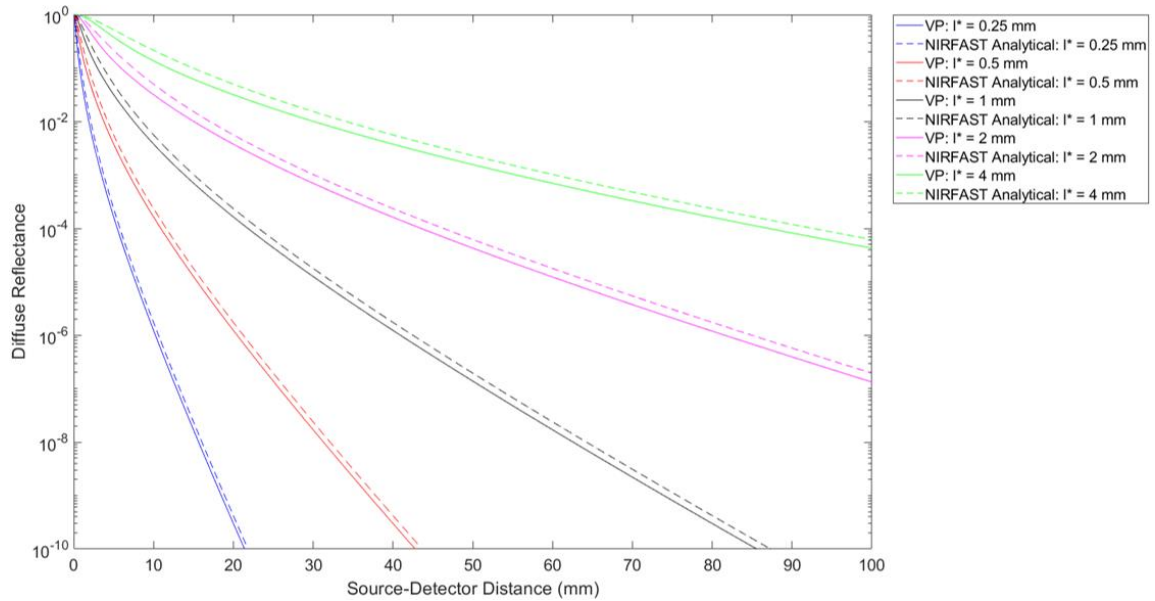
Figure 6.1: SRS model comparison. Diffuse reflectance versus source-detector separation distance for varying l* values, validating the NIRFAST semi-infinite analytical model against the virtual photonics solution. These reflectance plots are normalized to the nearest source-detector distance.

As seen from Figure 6.1 the validity of the NIRFAST analytical solution for SRS is comparable to VP solutions, for a series of varying optical properties. Limited divergence in observed between the two models, particularly for high l* due to empirical differences between the source modelling, which represents models of low scatter. Specifically, NIRFAST models the source as a point source at one scattering distance within the medium whereas the VP models the source as an exponentially decaying source which is also a function of the scattering coefficient.

6.3.2 SRS FEM model

With a validated NIRFAST analytical model, the next step is to consider the FEM capabilities of NIRFAST through the modelling of an SRS simulation. As with section 6.3.1, simulations of a point source within the FEM mesh were performed using an optimized two-resolution setup. This mesh contains two different regions, fine and coarse, to accurately model the light propagation and detector locations, whilst

generating a mesh that is computationally efficient. A central fine region is defined

ranging from -25 to 25 mm in both the x and y direction, with a resolution of 0.2 mm.

This region extends to a depth of 3 mm, with a decreasing resolution. The coarse

region continues to a depth of 50 mm, with a minimum z-resolution of 5 mm. This

coarse region also extends into the x and y dimensions to 50 mm, with a resolution

of 5 mm. This creates a total mesh size of ~500,000 nodes, corresponding to

~3,000,000 linear tetrahedral elements. Due to mesh size limitations, the source is

located at a modified depth value of $1/\mu_s'$, to ensure the sources are located at a

predefined nodal value, whist the detectors are limited to a maximum source-

detector distance of 25 mm.
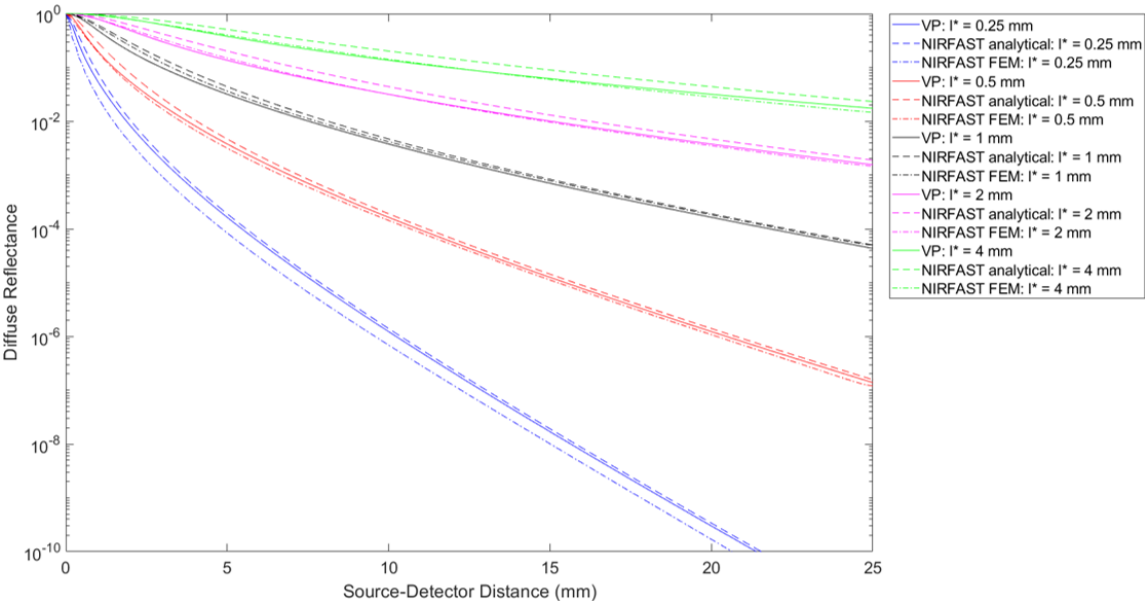
Figure 6.2: SRS FEM model comparison. Diffuse reflectance versus source-detector separation distance for varying l values, comparing the pre-validated virtual photonics (VP) solution and NIRFAST analytical solution, to the NIRFAST FEM based SRS models. These reflectance plots are normalized to the zero source-detector distance.*

As shown in Figure 6.2, the FEM based SRS models show good qualitative

comparison against both the NIRFAST analytical solution and VP. Again, the

models show a strong correlation across the range of source-detector separation

distances between all three models, with the small discrepancies expected across different model assumptions, particularly regarding the source-depth modelling. The NIRFAST FEM model shows a better agreement with the VP model, which can be attributed to the boundary conditions utilized within NIRFAST, which is of a mixed-type boundary condition [197].

6.3.3 Structured Illumination

The major advantage of SFDI is its ability to image directly within the spatial frequency domain. Whilst the simulations of SRS data have qualitatively validated the use of NIRFAST, the aim of this work is to develop a direct spatial frequency domain modelling tool, working towards complex geometries and heterogeneous simulations. The illumination follows the sinusoidal Equation 6.3 above, with physical systems utilizing a DMD to project these patterns upon a sample of interest. However, a combination of these illumination patterns, and the illumination depth dependency of the numerical solution is required for accurate parameter recovery, as outlined in section 6.2.1. Alongside this, the resolution, particularly in the direction of the spatially varying patterns, of the FEM mesh for simulations must also be optimized to ensure accurate demodulation whilst also maintaining a suitable mesh size for computational simulations. The line profiles for a three phases illumination at f_x= 0.2mm^{-1} along with its associated demodulation are shown in Figure 6.3. The AC demodulation has less than 0.2% variation across the centre on the image, representing an accurate demodulation.
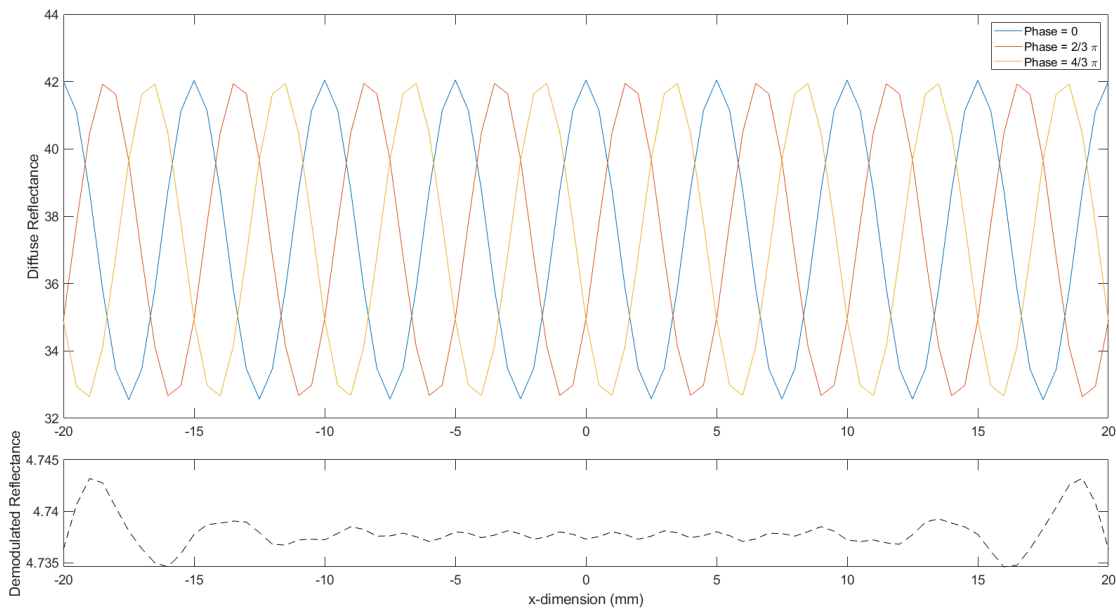
Figure 6.3: AC pattern and demodulation line profiles. Line profiles across the centre on the white bounding box for the three phases at f_x = 0.2 mm-1 alongside the AC demodulated profile of the same region. Here the AC demodulation exhibits less than 0.2% variation across the full profile.

The calculated fluence for a forward model of homogenous optical properties are shown in Figure 6.4. Both measurements are modelled at a zero-phase value, with spatial frequencies of 0 mm^{-1} and 0.2 mm^{-1} and normalized to the maximum fluence of the zero-frequency model. The optimized FEM mesh is 100 mm by 100 mm by 20 mm (x,y,z) with an illumination area of 80 mm by 80 mm (x,y). The detectors have a resolution of 0.5 mm and a field of view (FoV) of 20 mm by 20 mm (x,y), represented by the white bounding box in Figure 6.4. This structured illumination mesh contains a finer resolution area for accurate illumination and a coarse outer region, optimized for computational performance, creating a structure with over 900,000 nodes and ~5,000,000 linear tetrahedral elements, which is applied in all subsequent simulations.

140

$f_x = 0$ $f_x = 0.2$
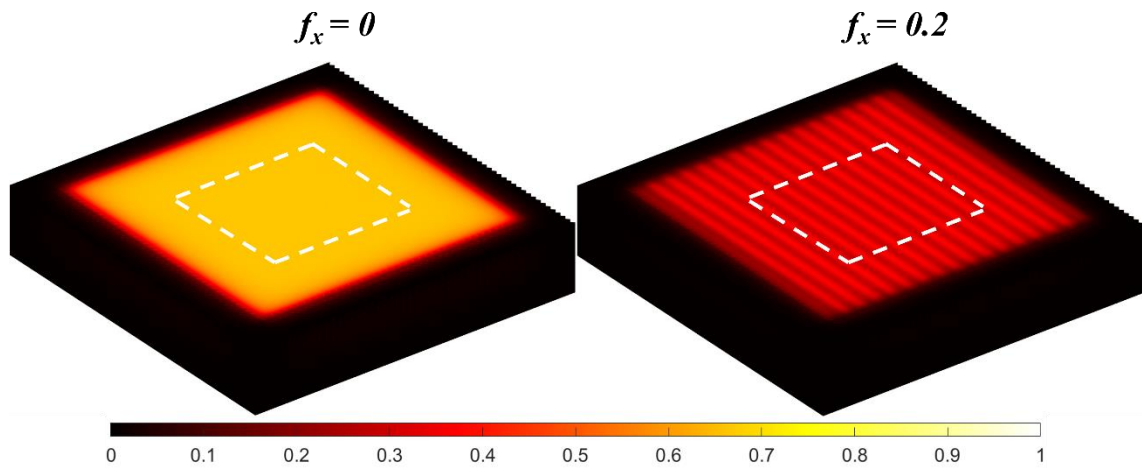
Figure 6.4: FEM model surface fluence. Normalized surface fluence from both a zero spatial frequency illumination and an illumination of $f_x = 0.2$ mm^{-1} and zero phase. The field of view for the detected 2D images is shown by the white bounding box.

The model mesh can also be shown in its tetrahedral element form with the green circle representing the model source location for a given depth value of $1/\mu'_s$, and the blue crosses representing the source locations (Figure 6.5).
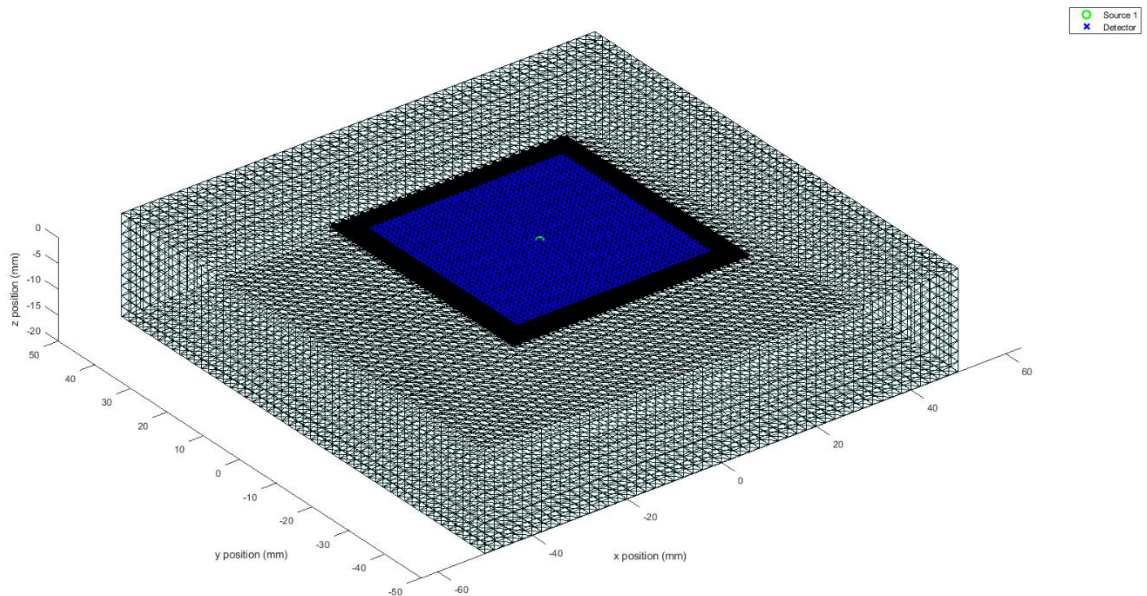
Figure 6.5: Tetrahedral meshing Mesh used for structured illumination modelling for SFDI direct in the spatial frequency domain. Tetrahedral mesh elements are created in two distinct regions, coarse and fine, with the model source (Green circle) and detector (Blue cross) locations shown across the large mesh model.

Homogenous Slab

The first forward models of structured illumination were performed using homogenous slabs. Simulations of varying bulk absorption were analysed using the full SFDI analysis procedure, with a calibration model used with fixed optical properties of $\mu_a = 0.01$ mm^{-1} and $\mu_s' = 1$ mm^{-1}. For each simulation, only the absorption coefficient was varied from -25% to +25%, in 5% increments, and compared to the calibration model, with the recovered absorption value reported from the centre of the image. An outline of the full procedure is shown below:

1. Generate the 3D mesh of desired optical properties and model the structured illumination as described previously.

2. Extract the model fluence from the mesh surface within the white bounding box of Figure 6.4 to obtain the SFDI 2D images, I(x,y).

3. Demodulate to obtain the resulting demodulated images (AC/DC) for all frequencies of illumination using Equations 5.1 and 5.2.

4. Calibrate using Equation 5.3 and a phantom simulation of known optical properties.

5. Extract the optical properties using the pixel-independent model from Cuccia *et.al* [174]. The central nodal value from the bounding box surface is used for comparison.

These recovered parameters were then compared to the modelled ground truth optical properties, and percentage errors quantified using the following equation:

$$Error = \frac{Recovered - Ground\ Truth}{Ground\ Truth} * 100. \qquad (6.5)$$

The parameters recovered show <2% error across the full range of optical properties tested, with both the values and the recovery error shown in Figure 5.

These initial models have demonstrated the validity of NIRFAST as compared to existing homogeneous SFDI modelling tools. The following sections consider increased heterogeneity through a series of simulations, highlighting the limitations of current SFDI modelling tools, providing further evidence for the need for pixel dependent approaches, for which the forward models as developed within NIRFAST provides.
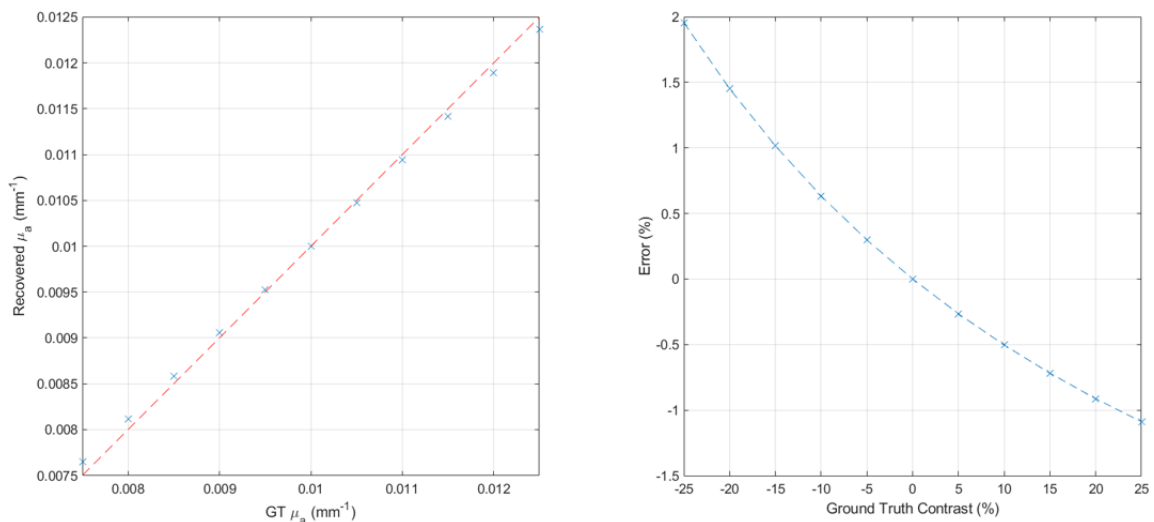
Figure 6.6: Homogenous slab simulation results. The recovered absorption is compared to the mesh ground truth alongside the parameter recovery error for each simulation, determined using Equation 6.5.

Heterogenous Anomaly Slabs

The second set of models applied a series of varying anomalies within the FEM mesh. Specifically, three variations of anomalies were simulated, of varying radius, depth as well as a tri-anomaly model as outlined in Figure 6.7.
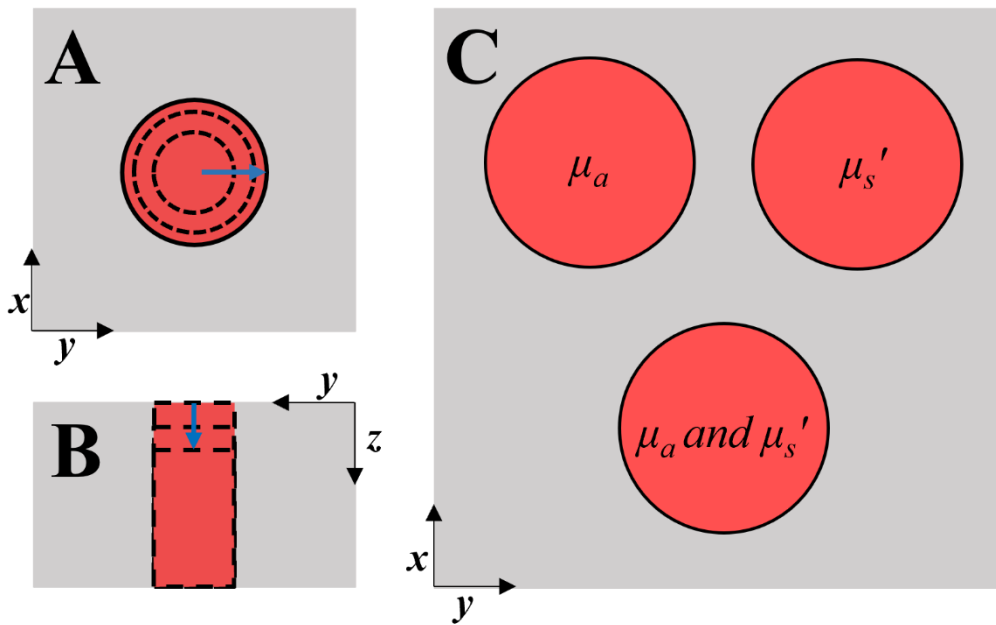
Figure 6.7: Anomaly slab models. A: Varying radii cylindrical anomaly model for a range of absorption values. B: Varying depth cylindrical anomaly model for a range of absorption values. C: Tri-anomaly model containing three fixed-radii cylindrical anomalies varying different optical properties.

To determine the accuracy of detecting different anomaly sizes, a cylindrical anomaly of varying absorption was placed within the centre of the FEM mesh, corresponding to the centre of the obtained 2D surface reflectance image (Figure 6.7 A). The same homogenous calibration model was used for each of the simulations, and the radii of the anomaly model was increased from 2 mm up to a maximum of 14 mm with 2 mm increments. The reduced scattering value was maintained at a value of 1 mm^{-1} whilst the absorption values were varied for up to a 50% increase as compared to the calibration phantom to a maximum value of 0.015 mm^{-1} with a step size of 0.001 mm^{-1}. The data calibration and demodulation, as outlined above, were applied and the recovered absorption values using the semi-infinite model were calculated. The resulting recovery errors for all anomalies tested are shown in Figure 6.8 A, with the central pixel value of the recovered anomaly compared to the anomaly ground truth.
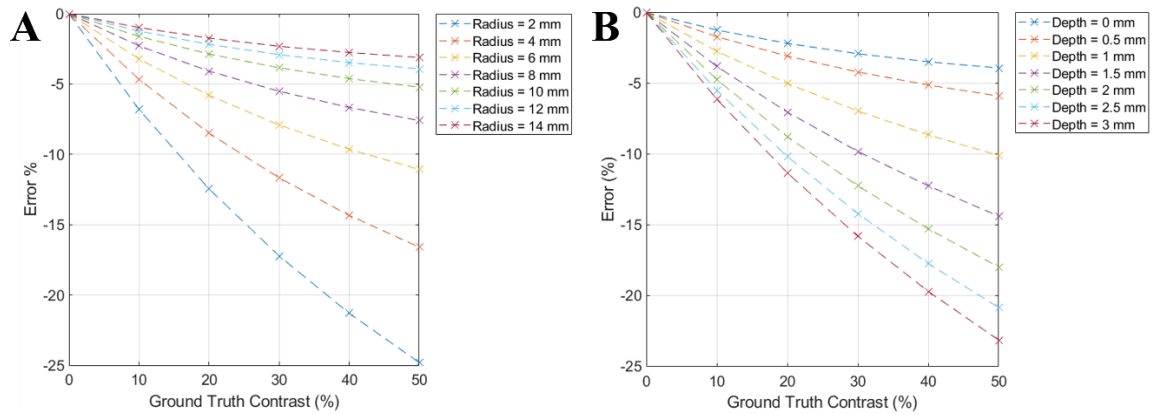
Figure 6.8: Single anomaly simulation results. A: Recovery errors for a centrally located anomaly of vary radii, with a range of absorption values simulated. B: Recovery errors for a centrally located anomaly of varying depths, with the same range of absorption values simulated. The recovery errors are determined using Equation 6.5.

The largest errors occur when either the absorption value is at its maximum or the anomaly size is at its minimum. The largest recovery error is obtained for the combination of these two points, at less than 25%, underpredicting the ground truth value. For radii greater than 6 mm, the recovery error for the full range of optical properties is <10% and <5% for anomalies larger than 10 mm.

Using the results from the radii models, the depth testing simulations were performed using the same range of optical properties for an anomaly of 12 mm radius. The anomaly was lowered into the model, depicted in Figure 6.7 B, to a maximum depth of 3 mm in 0.5 mm steps. The recovery errors, determined using Equation 6.5, are shown in Figure 6.8 B, again with the largest errors observed for the 50% increase in absorption. The parameter recovery accuracy also reduces as the anomaly is lowered into the mesh, with a maximum error of approximately 23%.

The final set of forward simulations for the structured illumination consisted of a tri-anomaly model, depicted in Figure 6 C. Three cylindrical anomalies, each 7 mm in radius, were placed equidistant from the model centre, each with varying different

optical properties. As with the previous models, the optical properties of each anomaly were increased in 5% increments to a maximum of 25%, compared to the calibration model values. The results for all three anomaly recovery errors, taken from each anomaly centre from the 2D reflectance image, are shown in Figure 6.9. As expected, the absorption only anomaly (Figure 6.9) follows the same trend as the radii example shown in Figure 6.8 A, with errors increasing to a maximum of 6% for the largest absorption value.
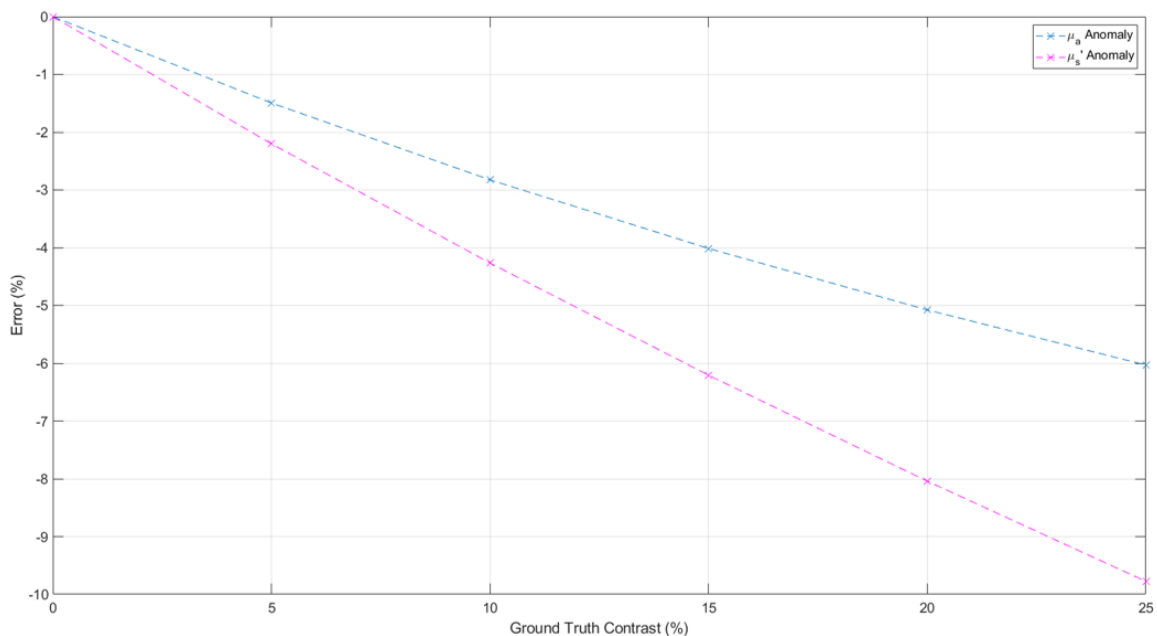
Figure 6.9: Tri-anomaly model, single optical property variation simulation results. Recovery errors for absorption only and reduced scattering only anomalies. The recovery errors are determined using Equation 6.5, for the full range of optical properties simulated, to a maximum of 25% increase compared to background and calibration phantom values.

The tri-anomaly models represent the first in which the reduced scattering value was also varied. The optical properties were recovered using the same method, and the reduced scattering recovery error calculated using Equation 6.5, with the results shown in Figure 6.9 for the scattering only anomaly. Here, the error remains <10% across all values of reduced scattering simulated.

Finally, the third anomaly from this model varied both of μa and μs' simultaneously across the same range. The recovered values for both parameters are shown in Figure 6.10, with the reduced scattering recovery error maintaining a similar trend to the scattering only anomaly results shown in Figure 6.9, with an underprediction of μs' by up to 10% for the largest variation when compared to the calibration phantom.
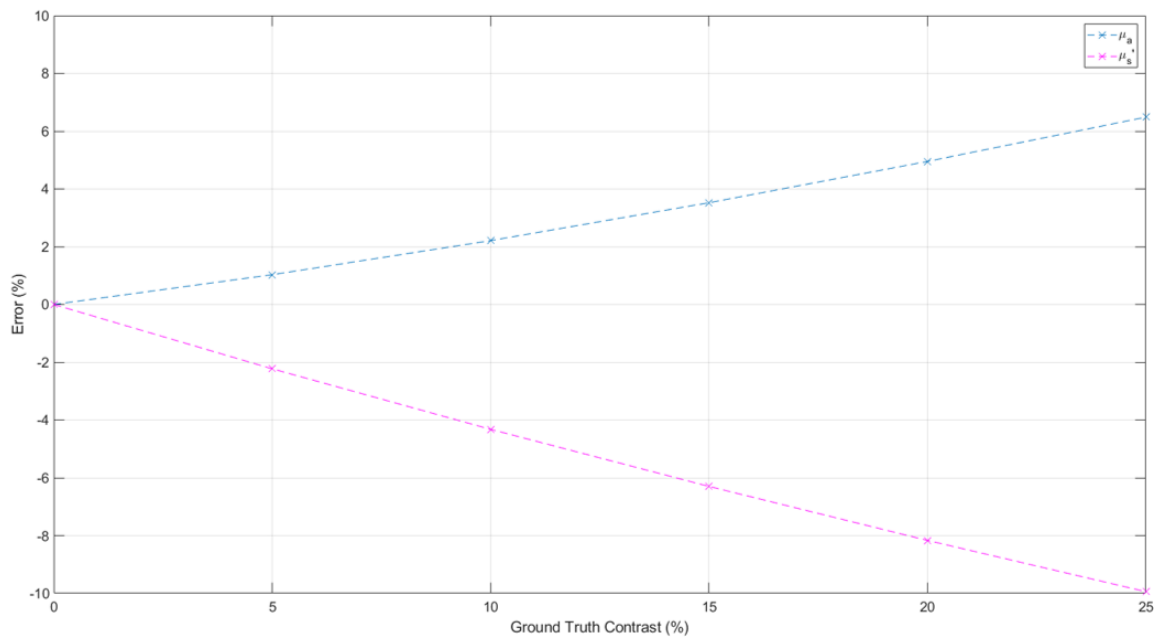
Figure 6.10: Tri-anomaly model, single simultaneous property variation simulation results. Recovered parameter errors for both absorption and reduced scattering, determined using Equation 6.5.

The recovered absorption errors were similar in magnitude to the absorption only anomaly (Figure 6.9) however the sign of the error is now positive, corresponding to an overprediction of ground truth value, with the largest error <7%. This is indicative of cross talk between the different optical properties, which can be further demonstrated by considering the qualitative results from the tri-anomaly model. Figure 6.11 outlines the full SFDI analysis procedure for a representative simulation, for an increase of optical properties by 25%.

147
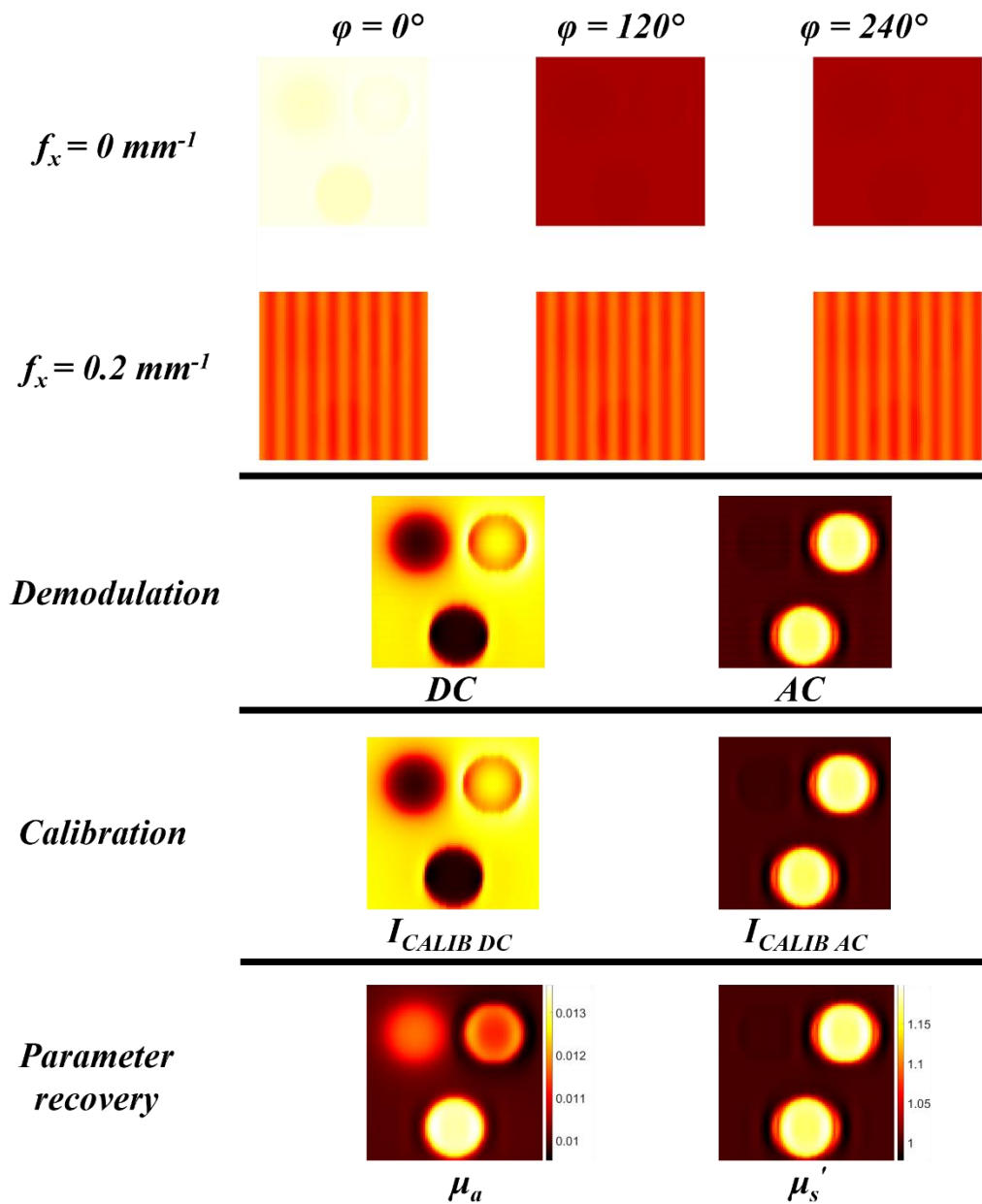
Figure 6.11: Tri-anomaly model full analysis. Analysis procedure for SFDI from the raw images of the tri-anomaly model (Figure 6.7 C) with a 25% increase in optical property values. Raw images from two spatial frequencies and three phases are shown, alongside the demodulated and calibrated results. Finally, the recovered optical property maps for both absorption and reduced scattering are also shown.

6.4 Discussion

NIRFAST, an existing FEM based light propagation modelling tool, has been adapted for the forward simulation of SFDI models for pixel-dependent

heterogeneous modelling. Prior to running simulations of structured illumination, SRS validation was performed between existing analytical solutions and NIRAST semi-infinite solutions (Figure 6.2). This was followed by further validation of NIRFAST through the simulation of an FEM based SRS model.

Whilst the validation of NIRFAST using SRS data is a key step towards full SFDI forward modelling, the aim of this work was to perform direct frequency domain modelling upon complex heterogeneous samples, towards pixel-dependent simulations. Optimization of the FEM mesh, to ensure both accurate modelling of the characteristic spatially modulated light and accurate demodulation alongside computational efficiency, was performed to reduce the recovery error for both absorption and reduced scattering parameters for direct SFDI simulations.

The first series of simulations performed using the optimized mesh considered homogenous optical properties, with the computation time for each of the reflectance data-set (each phase and frequency) at ~1 second utilizing Tesla V100 16 Gb graphics processing unit (GPU). These properties were varied by ±25% compared to a calibration phantom. Across this range, a recovery error of less than 2% was observed, further validating NIRFAST as a SFDI modelling tool. The recovered optical properties are determined at the centre of each image, however, due to the homogenous properties of the mesh, the pixel-dependent recovery algorithm still recovers the parameters with limited errors. This is due to the model beginning to represent the semi-infinite solution due to the large mesh geometry.

To test the full capabilities of NIRFAST as a SFDI forward modelling tool, heterogeneity was introduced through the addition of cylindrical anomalies of

varying optical properties (Figure 6.7). The first set of simulations placed this anomaly at the centre of the mesh, with increasing radii in 2 mm steps from 2-14 mm, whilst also varying the absorption coefficient up to 50%, compared to both the calibration phantom and the remaining background mesh. The largest error, <25%, was observed for the smallest radii anomaly at the largest optical property variation. However, for anomalies of radii greater than 6 mm, recovery errors were less than 10%, while for the largest anomalies these errors fall below 5% across the full range of absorption values tested. Limited improvements were observed between the 12 mm and 14 mm anomaly; therefore the 12 mm radii anomaly was chosen for the depth sensitivity simulations.

For the depth varying simulations, the 12 mm radii anomaly was lowered within the mesh in 0.5 mm steps, from the surface down to a depth of 3 mm. As expected, the recovery error increased as a function of depth, and a similar trend was observed when the absorption parameters were increased, with a maximum recovery error of approximately 23%. However, even the smallest variation in absorption was detectable at the maximum depth, although, due to the laterally homogenous recover algorithm, the ability to determine different optical properties within a single pixel is limited. This has been addressed in previous studies, with two layered Monte-Carlo simulations, but does not address the lateral variations of the heterogeneous models simulated.

These single anomaly models only considered variations to the mesh absorption parameter, with the reduced scattering value maintained at 1 mm^{-1}, the same as the calibration value. To simulate variations for both absorption and reduced scattering parameters, a tri-anomaly model was developed, containing three different

cylindrical anomalies, placed equidistant from the mesh centre, each varying different combinations of μ_a and μ_s' (Figure 6.6 C). The optical properties were again varied up to a 25% increase compared to the calibration phantom and mesh background values, with the recovery errors shown in Figure 6.10 and Figure 6.11 for all three anomalies. The absorption only anomaly follows a similar trend to the radii testing results in Figure 6.8 A, whilst the scattering only anomaly also recovered the optical properties across the full range of variation, with a less than 10% error.

For the final tri-anomaly model, both μ_a and μ_s' were varied simultaneously, with incremental increases of 5%, up to a maximum of 25% compared to the calibration phantom and mesh background values. The recovery errors for the reduced scattering parameter follow a similar trend to the reduced scattering only anomaly. Whilst the absorption errors are of similar magnitude, they are reversed in sign compared to the absorption only anomaly, with an overprediction now observed, compared to the ground truth mesh values. As the location of the source illumination is dependent upon the scattering value, recovered properties are affected when this is varied. The range of scattering values used for this study, along with the resolution of the optimized mesh, resulted in the source locations being the same for all simulations, at a depth of 1 mm into the mesh. However, this effects the recovered values, as the inverse model used has a fully dependent source depth, as shown in Equation 6.1. This results in the different recovery values when the reduced scattering is also altered, producing a cross talk between the two parameters.

The cross talk is further observed in the qualitative analysis shown in Figure 6.11. The obtained optical property maps show a close match for the scattering anomalies; however, a false anomaly is detected within the absorption map,

compared to the ground truth shown in Figure 6.7 C. Despite this, the qualitative maps highlight the issue of pixel-independent simulations and recovery. Whilst the ground truths have a hard boundary between the two different optical properties of the anomaly and background mesh, the simulated reflectance produces a gradient across this region, due to the lateral interactions within the FEM simulation. This produces the recovered anomaly boundary limitations also observed within current clinical SFDI applications.

6.5 Conclusion

The use of a NIRFAST SFDI forward model allows for the simulation of arbitrary shaped models, along with both complex geometries and varying optical properties. Initial validation has been performed against existing homogenous SFDI models using spatially resolved spectroscopy methods before further validation in the spatial frequency domain using homogenous FEM models. With a fully verified modelling tool, heterogeneity was introduced through a serious of cylindrical anomalies of varying optical properties, demonstrating the ability to produce pixel-independent forward models, whilst also highlighting the limitations of current pixel dependent SFDI inverse solvers. Further work is needed to adapt NIRFAST as a full SFDI inverse solver for parameter recovery, which would improve the recovered anomaly boundary error detection. Specifically with the availability of a verified forward solver, it is aimed to extend this model to the creation of a mapping function (also known as the Jacobian) that will allow the recovery of spatially varying optical properties from SFDI measurements directly. The use of alternative models such as Monte Carlo are also possible to extend the accuracy of the light propagation, but it should be noted that such approaches will increase the computational complexity and

further work in establishing an efficient and accurate model based on these are needed. This work represents a key step towards the goal of pixel-dependent SFDI modelling and parameter recovery.

Chapter 7

7 Conclusions and Future Work

7.1 General Conclusions

Point-of-care wound healing assessment methods suffer from two major issues: subjectivity from the parameters considered, along with the reliance upon the knowledge and experience of highly trained professionals to assess each individual wound throughout its healing process. Parameters such as wound area, smell and discharge are used as gold standard metrics, with limited conformity in assessment parameters or gradings across different wound types [2, 19]. These issues are further compounded when considering a military battlefield setting, where wounds are often more severe and access to continual medical care is limited.

Optical imaging techniques offer a solution to these issues and whilst different methods, ranging from simple RGB photography to advanced spectroscopic methods such as Raman and OCT, still possess limitations [47, 85, 92]. The aim of this work was to advance point-of-care wound assessment methodologies through research into hyperspectral imaging modalities within the infrared region. Two different modalities were considered in this work, Negative Contrast Imaging using a non-commercially available SWIR/MWIR device and Spatial Frequency Domain Imaging, which is focused within the NIR range, although it can be applied into both the visible and SWIR. These modalities fulfil the requirements for improved wound assessment through the quantification of tissue parameters such as absorption and reduced scattering coefficients, combating the subjectivity of current methods. They

are also deployable in varying environments, due to no reliance of either wound preparation or the need for specialised equipment. Wounds can be assessed regularly throughout the course of the wound healing timeline via a non-invasive process, with the ability to record optical maps of the quantified parameters for continued assessment from varying medical professionals.

An introduction to the biology of wound healing is provided in Chapter 1, highlighting the complexity of the wound healing process and the many stages in which they can deviate from a normal healing process [203], hence the need for regular observation and assessment. This chapter also reviewed the challenges associated with wound healing within the military environment, from the complexities of blast injuries to the patient care pathway for injured personal [23]. This chapter outlined both the medical and operational requirements for any wound assessment tool, which can be addressed through optical imaging modalities.

Chapter 2 introduces the key aspects of biomedical imaging, giving a theoretical grounding for the remainder of the chapter, which reviews existing imaging modalities for wound assessment. A range of methods were critically assessed, with areas for advancement identified. Namely, the need for robust modalities which offer both quantitative information across a range of wound healing parameters, alongside complimentary image analysis tools, based upon computational methods, with the aim of removing the subjectivity of existing gold standard methods, which are still based upon visual observation [2].

The first of the computational tools was developed in Chapter 3, which considers samples analysed using FTIR spectroscopy for a previous study undertaken at Dstl

[94]. Wound biopsies from seven different donors were previously imaged using FTIR to obtain spectral data within the 2.4-15.4 µm wavelength range. Visually, two of the three wounds, which experienced regular healing, were identifiable in a focused spectral region around 3125 nm, however the third healed wound was indistinguishable from those that experienced non-regular healing. Intelligent data analysis methods, in the form of k-means clustering alongside dimensional reduction via PCA, were applied to separate the seven samples into either regular/unregular healing or the three different observed wound healing pathologies. For the two-class clustering, the same outcome occurred with only the same two of three healed samples correctly identifiable. However, when the three-cluster model was applied to the PCA data across the full spectral ranged measured, the three healed samples were separable, demonstrating that additional spectral information aides the clustering process, offering an improvement upon visual inspection. Whilst the sample number was limited, these methods were taken forward and applied in Chapter 4.

Additional wound biopsy samples were unavailable for further study, therefore a different approach for wounded samples was taken. Cell culture of human epidermal fibroblasts, the main cell type present in the skins connective tissue, were grown for trauma modelling, *in vitro*. Two different levels of trauma were introduced through chemical assays to represent wound samples, which were compared to healthy cell cultures for a binary diagnosis. The NCI was used to image the cell cultures at a 10 nm resolution across a broad 2500-3500 nm range, incorporating the region which separated the wound biopsies from Chapter 3.

Both k-means clustering and PCA were performed on the raw spectral data, as well as additional pre-processing methods such as smoothing and spectral derivatives, generating a series of different data types for clustering analysis. Whilst the majority of these data types showed either a high TCI or HCI, the highest performing data type was the background subtracted spectral derivative data set. Both the TCI and HCI were >95% for separation of the healthy and traumatised cell cultures, demonstrating the ability of the NCI, along with intelligent spectral analysis methods, to accurately diagnose healthy and traumatised cell cultures. However, further analysis of the cluster qualities found the trauma cluster observed a low score, meaning a weak cluster. This is likely due to both the different trauma methods applied, inducing either apoptosis or necrosis, alongside the relatively low sample number. Despite this, the work highlights the ability to gain additional information from a broader spectral range when analysed with computational tools, separating spectral data with undetectable differences when analysed through visual observation or classic analysis methods. This constitutes a key step towards non-subjective methodologies for wound assessment.

Whilst both the computational tools and sample methods were advanced in Chapters 3 and 4, the imaging modalities were not altered or optimised. The FTIR requires liquid nitrogen for detector cooling [162], making it unsuitable for versatile deployment and the NCI is a non-commercial prototype device [94], where additional advancements are required beyond the scope of this PhD, before meriting further study. With this in mind, alongside the demonstration that additional spectral information, from a broad range of IR wavelengths, aids in improving diagnostics, the remainder of the work focused upon the second imaging modality, SFDI.

SFDI is a low cost, versatile and non-invasive method which utilises spatially modulated light projections to extract both the absorption and reduced scattering coefficients within the visible-SWIR range for a sample of interest [79]. Reflectance images for multi-spectral imaging are obtained and processed in a pixel-wise manner to produce optical property maps to aid in wound diagnosis. Due to the pixel wise nature of the analysis procedure, two main areas of improvement were identified for investigation. The first of these, presented in Chapter 5, aimed to reduce the number of measurements required to obtain raw SFDI images non-homogenous samples through the application of CS. Additionally, CS was applied to the image analysis stage to reduce the number of individual pixel measurements required to obtain optical property maps.

Using an open-source data set from AppSFDI [187], containing SFDI data of a human hand, CS image acquisition was simulated with up to 30% data reduction observed whilst maintaining <10% error in recovered optical property maps. Whilst this produces a lower data reduction than a previous study [180], this represents the first application to a clinically relevant data set, which contains a lower level of sparsity, therefore a reduced data reduction is expected. During the analysis phase, following demodulation of the acquired sample images, optical property maps were determined using a pixel-wise methodology. CS was also applied to these steps of the analysis process, with a data reduction of up to 90% observed whilst still maintaining <10% recovery error. A pixel-wise RMS error map highlighted the areas of highest recover error, corresponding to the areas of greatest optical property gradient and the boundaries of the hand sample. Whilst this is in part due to the

recovery CS algorithm, the pixel wise analysis procedure of SFDI also contributes to these boundary errors.

Traditional SFDI optical parameter recovery rely upon pixel-independent inverse solver methods based upon either the diffusion approximation or Monte Carlo look up tables [174]. Whilst suitable for homogenous samples, increased heterogeneity from varying optical parameter values of neighbouring pixels introduces boundary errors. Moreover, these same tools are utilised for forward modelling, limiting their applications for clinical applications. An approach for pixel-independent forward modelling is described in Chapter 6, through the adaptation of NIRFAST, an existing FEM based modelling tool [43]. Initially, forward models of homogenous samples were simulated to verify the methodology, with parameters recovered using a current pixel dependent SFDI inverse solver. This was followed by simulations of models containing both complex geometries and varying optical properties, demonstrating the ability of NIRFAST to produce pixel-independent forward modelling.

7.2 Future Work

Two main imaging modalities have been investigated during this PhD, with the NCI device utilised for live cell culture imaging, generating spectral data for intelligent data analysis methods along with SFDI, in which compressive sensing methods and pixel dependent forward modelling were applied to open-source data and theoretical models respectively. Future work for both modalities can be split into three separate areas, wound samples, hardware modifications and algorithm developments, which will be discussed below. However, a combination of both areas will build upon the

foundation provided by this PhD, working towards improved wound diagnosis methods.

7.2.1 Wound samples

Chapter 3 introduced the intelligent spectral analysis methods for spectral data, which were then applied to cell cultures for binary diagnosis in Chapter 4. These methods were designed to counteract the main limitation of this work, a small sample number of wound biopsies. Whilst additional information was extracted from this limited data set, and as additional samples were not accessible during this work, this should be a focus for future work. Not only can these samples be imaged and analysed using the NCI, the methods for advancing the field of SFDI require physical samples for further validation, which any fixed biopsy sample would provide. In addition, samples from *ex vivo* porcine blast models would provide a further validation data type for both imaging modalities [204].

These models would increase the complexity of the biology imaged, providing grounds for further investigation into the individual biological constituents that generate the spectral differences between healthy and traumatised or wounded samples and cell cultures. This could be achieved through further cell culture studies, varying the cell types in single cell models, such as keratinocytes, neutrophils, and macrophages. Complex cell cultures, consisting of multiple cell types could then be developed, building towards tissue engineered skin cell models [205].

7.2.2 Hardware modifications

To optimise the use of further wound samples, improvements to system hardware could be implemented. As discussed in section 4.4.2, improvements to the NCI, including advanced detection for improved image resolution alongside faster image acquisition would allow the NCI to be used *in situ* for further clinical applications. Improvements to the system GUI could also provide real time imaging, improving user experience for varying medical professionals in the long term.

Due to the open source nature of SFDI [171], implementation of a physical SFDI system would provide experimental validation to the work shown in Chapters 5 and 6. The system can also be modified for additional wavelengths, to work towards multi- and hyperspectral SFDI imaging across the NIR/SWIR range.

7.2.3 Algorithms

The final area for further investigation would be improving existing algorithms and assessing further analysis methods. Due to the low sample numbers, classification methods were not explored for spectral analysis in Chapters 3 and 4. However, with a larger data set, training, testing, and validation subsets can be utilised for classification methods alongside the implementation of Neural Networks. These methods, as discussed in section 2.3, often require sample sizes into the 100s for classifiers, with neural networks also using 1000s and above, although an exact rule is not specified [206, 207]. As for the data labels, for both the wound biopsy and cell spectra studies on Chapters 3 and 4, the *a priori* labels already exist in the form of the wound healing outcome or applied trauma treatment.

Additional, more sophisticated, clustering and data reduction methodologies could also be implemented. Kernel PCA is a method in which PCA is applied in a nonlinear way, resulting in the construction of nonlinear mappings in order to maximise the variance. Further clustering algorithms, such as k-means++ and fuzzy c-means also merit further study as they are also used in wound healing spectral analysis [104, 116].

Within the SFDI work, the compressive sensing methodologies could be applied to the full SFDI process, acquiring compressed images, demodulating within the compressed state then obtaining optical property maps. This requires further study into the demodulation method and could improve upon the data reduction already observed during this work. The major area of focus however comes from the pixel-independent methods developed within NIRFAST. By extending the model to the creation of mapping functions, parameter recovery for inverse modelling could create improved SFDI optical property maps for samples of both complex geometry and increased heterogeneity, as seen in clinical wound applications.

Appendix

A.1 Bates-Jenson Wound Assessment Tool

BATES-JENSEN WOUND ASSESSMENT TOOL
Instructions for use

<u>General Guidelines:</u>

Fill out the attached rating sheet to assess a wound's status after reading the definitions and methods of assessment described below. Evaluate once a week and whenever a change occurs in the wound. Rate according to each item by picking the response that best describes the wound and entering that score in the item score column for the appropriate date. When you have rated the wound on all items, determine the total score by adding together the 13-item scores. The HIGHER the total score, the more severe the wound status. Plot total score on the Wound Status Continuum to determine progress.

<u>Specific Instructions:</u>
1. **Size:** Use ruler to measure the longest and widest aspect of the wound surface in centimeters; multiply length x width.

2. **Depth:** Pick the depth, thickness, most appropriate to the wound using these additional descriptions:
   1 = tissues damaged but no break in skin surface.
   2 = superficial, abrasion, blister or shallow crater. Even with, &/or elevated above skin surface (e.g., hyperplasia).
   3 = deep crater with or without undermining of adjacent tissue.
   4 = visualization of tissue layers not possible due to necrosis.
   5 = supporting structures include tendon, joint capsule.

3. **Edges:** Use this guide:
Indistinct, diffuse	=	unable to clearly distinguish wound outline.
Attached	=	even or flush with wound base, <u>no</u> sides or walls present; flat.
Not attached	=	sides or walls <u>are</u> present; floor or base of wound is deeper than edge.
Rolled under, thickened	=	soft to firm and flexible to touch.
Hyperkeratosis	=	callous-like tissue formation around wound & at edges.
Fibrotic, scarred	=	hard, rigid to touch.

4. **Undermining:** Assess by inserting a cotton tipped applicator under the wound edge; advance it as far as it will go without using undue force; raise the tip of the applicator so it may be seen or felt on the surface of the skin; mark the surface with a pen; measure the distance from the mark on the skin to the edge of the wound. Continue process around the wound. Then use a transparent metric measuring guide with concentric circles divided into 4 (25%) pie-shaped quadrants to help determine percent of wound involved.

5. **Necrotic Tissue Type:** Pick the type of necrotic tissue that is <u>predominant</u> in the wound according to color, consistency and adherence using this guide:
White/gray non-viable tissue	=	may appear prior to wound opening; skin surface is white or gray.
Non-adherent, yellow slough	=	thin, mucinous substance; scattered throughout wound bed; easily separated from wound tissue.
Loosely adherent, yellow slough	=	thick, stringy, clumps of debris; attached to wound tissue.
Adherent, soft, black eschar	=	soggy tissue; strongly attached to tissue in center or base of wound.
Firmly adherent, hard/black eschar	=	firm, crusty tissue; strongly attached to wound base <u>and</u> edges (like a hard scab).

© 2001 Barbara Bates-Jensen

6. **Necrotic Tissue Amount**: Use a transparent metric measuring guide with concentric circles divided into 4 (25%) pie-shaped quadrants to help determine percent of wound involved.

7. **Exudate Type**: Some dressings interact with wound drainage to produce a gel or trap liquid. Before assessing exudate type, gently cleanse wound with normal saline or water. Pick the exudate type that is <u>predominant</u> in the wound according to color and consistency, using this guide:

Bloody	=	thin, bright red
Serosanguineous	=	thin, watery pale red to pink
Serous	=	thin, watery, clear
Purulent	=	thin or thick, opaque tan to yellow
Foul purulent	=	thick, opaque yellow to green with offensive odor

8. **Exudate Amount**: Use a transparent metric measuring guide with concentric circles divided into 4 (25%) pie-shaped quadrants to determine percent of dressing involved with exudate. Use this guide:

None	=	wound tissues dry.
Scant	=	wound tissues moist; no measurable exudate.
Small	=	wound tissues wet; moisture evenly distributed in wound; drainage involves $\leq$ 25% dressing.
Moderate	=	wound tissues saturated; drainage may or may not be evenly distributed in wound; drainage involves > 25% to $\leq$ 75% dressing.
Large	=	wound tissues bathed in fluid; drainage freely expressed; may or may not be evenly distributed in wound; drainage involves > 75% of dressing.

9. **Skin Color Surrounding Wound**: Assess tissues within 4cm of wound edge. Dark-skinned persons show the colors "bright red" and "dark red" as a deepening of normal ethnic skin color or a purple hue. As healing occurs in dark-skinned persons, the new skin is pink and may never darken.

10. **Peripheral Tissue Edema & Induration**: Assess tissues within 4cm of wound edge. Non-pitting edema appears as skin that is shiny and taut. Identify pitting edema by firmly pressing a finger down into the tissues and waiting for 5 seconds, on release of pressure, tissues fail to resume previous position and an indentation appears. Induration is abnormal firmness of tissues with margins. Assess by gently pinching the tissues. Induration results in an inability to pinch the tissues. Use a transparent metric measuring guide to determine how far edema or induration extends beyond wound.

11. **Granulation Tissue**: Granulation tissue is the growth of small blood vessels and connective tissue to fill in full thickness wounds. Tissue is healthy when bright, beefy red, shiny and granular with a velvety appearance. Poor vascular supply appears as pale pink or blanched to dull, dusky red color.

12. **Epithelialization**: Epithelialization is the process of epidermal resurfacing and appears as pink or red skin. In partial thickness wounds it can occur throughout the wound bed as well as from the wound edges. In full thickness wounds it occurs from the edges only. Use a transparent metric measuring guide with concentric circles divided into 4 (25%) pie-shaped quadrants to help determine percent of wound involved and to measure the distance the epithelial tissue extends into the wound.

BATES-JENSEN WOUND ASSESSMENT TOOL   NAME

Complete the rating sheet to assess wound status. Evaluate each item by picking the response that best describes the wound and entering the score in the item score column for the appropriate date.

Location: Anatomic site. Circle, identify right (R) or left (L) and use "X" to mark site on body diagrams:

____	Sacrum & coccyx	____	Lateral ankle
____	Trochanter	____	Medial ankle
____	Ischial tuberosity	____	Heel Other Site
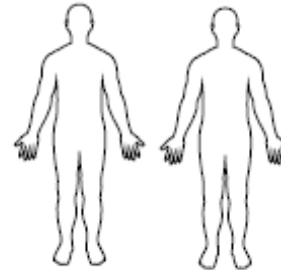
Shape: Overall wound pattern; assess by observing perimeter and depth.

Circle and <u>date</u> appropriate description:

____	Irregular	____	Linear or elongated
____	Round/oval	____	Bowl/boat
____	Square/rectangle	____	Butterfly Other Shape

Item	Assessment	Date Score	Date Score	Date Score
1. Size	1 = Length x width <4 sq cm 2 = Length x width 4--<16 sq cm 3 = Length x width 16.1--<36 sq cm 4 = Length x width 36.1--<80 sq cm 5 = Length x width >80 sq cm			
2. Depth	1 = Non-blanchable erythema on intact skin 2 = Partial thickness skin loss involving epidermis &/or dermis 3 = Full thickness skin loss involving damage or necrosis of subcutaneous tissue; may extend down to but not through underlying fascia; &/or mixed partial & full thickness &/or tissue layers obscured by granulation tissue 4 = Obscured by necrosis 5 = Full thickness skin loss with extensive destruction, tissue necrosis or damage to muscle, bone or supporting structures			
3. Edges	1 = Indistinct, diffuse, none clearly visible 2 = Distinct, outline clearly visible, attached, even with wound base 3 = Well-defined, not attached to wound base 4 = Well-defined, not attached to base, rolled under, thickened 5 = Well-defined, fibrotic, scarred or hyperkeratotic			
4. Under-mining	1 = None present 2 = Undermining < 2 cm in any area 3 = Undermining 2-4 cm involving < 50% wound margins 4 = Undermining 2-4 cm involving > 50% wound margins 5 = Undermining > 4 cm or Tunneling in any area			
5. Necrotic Tissue Type	1 = None visible 2 = White/grey non-viable tissue &/or non-adherent yellow slough 3 = Loosely adherent yellow slough 4 = Adherent, soft, black eschar 5 = Firmly adherent, hard, black eschar			
6. Necrotic Tissue Amount	1 = None visible 2 = < 25% of wound bed covered 3 = 25% to 50% of wound covered 4 = > 50% and < 75% of wound covered 5 = 75% to 100% of wound covered			
7. Exudate Type	1 = None			

Item	Assessment	Date Score	Date Score	Date Score
	2 = Bloody 3 = Serosanguineous: thin, watery, pale red/pink 4 = Serous: thin, watery, clear 5 = Purulent: thin or thick, opaque, tan/yellow, with or without odor			
8. Exudate Amount	1 = None, dry wound 2 = Scant, wound moist but no observable exudate 3 = Small 4 = Moderate 5 = Large			
9. Skin Color Sur-rounding Wound	1 = Pink or normal for ethnic group 2 = Bright red &/or blanches to touch 3 = White or grey pallor or hypopigmented 4 = Dark red or purple &/or non-blanchable 5 = Black or hyperpigmented			
10. Peripheral Tissue Edema	1 = No swelling or edema 2 = Non-pitting edema extends <4 cm around wound 3 = Non-pitting edema extends ≥4 cm around wound 4 = Pitting edema extends < 4 cm around wound 5 = Crepitus and/or pitting edema extends ≥4 cm around wound			
11. Peripheral Tissue Induration	1 = None present 2 = Induration, < 2 cm around wound 3 = Induration 2-4 cm extending < 50% around wound 4 = Induration 2-4 cm extending ≥ 50% around wound 5 = Induration > 4 cm in any area around wound			
12. Granu-lation Tissue	1 = Skin intact or partial thickness wound 2 = Bright, beefy red; 75% to 100% of wound filled &/or tissue overgrowth 3 = Bright, beefy red; < 75% & > 25% of wound filled 4 = Pink, &/or dull, dusky red &/or fills ≤ 25% of wound 5 = No granulation tissue present			
13. Epithe-lializa-tion	1 = 100% wound covered, surface intact 2 = 75% to <100% wound covered &/or epithelial tissue extends >0.5cm into wound bed 3 = 50% to <75% wound covered &/or epithelial tissue extends to <0.5cm into wound bed 4 = 25% to < 50% wound covered 5 = < 25% wound covered			
	TOTAL SCORE			
	SIGNATURE			

WOUND STATUS CONTINUUM

```
◄──┼────┼────┼────┼────┼────┼────┼────┼────┼────┼────┼──►
   1    5   10 13 15  20   25   30   35   40   45   50   55   60
Tissue      Wound                                          Wound
Health      Regeneration                                   Degeneration
```

Plot the total score on the Wound Status Continuum by putting an "X" on the line and the date beneath the line. Plot multiple scores with their dates to see-at-a-glance regeneration or degeneration of the wound.

© 2001Barbara Bates-Jensen

168

A.2 NCI Spatial Distortion Correction

Through initial testing of the NCI imaging capabilities, a spatial distortion issue was identified through imaging of checkerboard patterns. An example of this is shown in Figure 3.14 as the uncorrected image. In discussion with the manufacturer, M Squared Lasers, they passed on a correction code for this known distortion, which applies in the y axis only. This however did not show the desired correction on the initial images collected.

Following further discussion with M Squared Lasers and a visit to their labs in Glasgow, it was found that the aspect ratio of the collected image varied at different zoom levels, and the correction code was only suitable for the value set for the maximum zoom. The aspect ratio was altered for all zoom levels to ensure the correction is accurate. The correction code uses a linear interpolation of a sinusoidal function to adjust the pixels in the y axis.
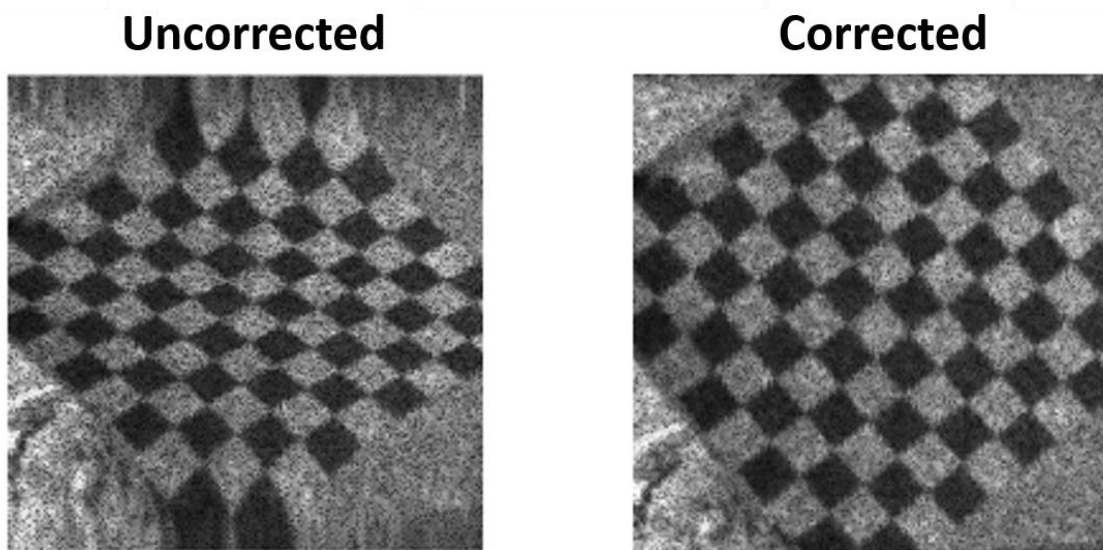
Figure A2.1: NCI image correction. A 1 cm checker-board pattern was imaged to demonstrate the correction code applied to the NCI images for spatial distortion. The image on the left shows the raw image from the device, while the image on the right is the post-processed corrected image.

This correction is built into the NCI imager, with the pseudo code below:

1. Load Images File.

2. Convert image to double format matrix.

3. Identify image dimensions.

4. Generate corrected y-axis image coordinates using sinusoidal function:

$$y = n * [0.5 + 0.5\sin((\tfrac{x}{n-0.5}) * \pi)],$$

   where n is the size of the image in the y-axis, and x is the corresponding x-axis coordinate.

5. Generate meshes for both original and corrected image.

6. Interpolate image to corrected mesh.

7. Convert matrix to image file.

List of References

1. Murray, C.J.L., et al., *Disability-adjusted life years (DALYs) for 291 diseases and injuries in 21 regions, 1990–2010: a systematic analysis for the Global Burden of Disease Study 2010.* The Lancet, 2012. **380**(9859): p. 2197-2223.
2. Benbow, M., *Best practice in wound assessment.* Nurs Stand, 2016. **30**(27): p. 40-7.
3. Sowa, M.G., et al., *Review of near-infrared methods for wound assessment.* 2016. **21**(9): p. 091304.
4. Jayachandran, M., et al., *Critical review of noninvasive optical technologies for wound imaging.* 2016. **5**(8): p. 349-359.
5. Gonzalez, A.C.d.O., et al., *Wound healing - A literature review.* Anais brasileiros de dermatologia, 2016. **91**(5): p. 614-620.
6. Velnar, T., T. Bailey, and V. Smrkolj, *The Wound Healing Process: An Overview of the Cellular and Molecular Mechanisms.* Journal of International Medical Research, 2009. **37**(5): p. 1528-1542.
7. Beldon, P., *Basic science of wound healing.* Surgery (Oxford), 2010. **28**(9): p. 409-412.
8. Aukhil, I.J.P., *Biology of wound healing.* 2000. **22**(1): p. 44-50.
9. Martin, C. and I.J.B.j.o.p.s. Muir, *The role of lymphocytes in wound healing.* 1990. **43**(6): p. 655-662.
10. Schäffer, M. and A. Barbul, *Lymphocyte function in wound healing and following injury.* Br J Surg, 1998. **85**(4): p. 444-60.
11. Mosser, D.M. and J.P.J.N.r.i. Edwards, *Exploring the full spectrum of macrophage activation.* 2008. **8**(12): p. 958.
12. Mercandetti, M. and A.J.E. Cohen, *Wound healing and repair.* 2017. **14**(1): p. 12-20.
13. Pastar, I., et al., *Epithelialization in wound healing: a comprehensive review.* 2014. **3**(7): p. 445-464.
14. Tonnesen, M.G., X. Feng, and R.A. Clark. *Angiogenesis in wound healing*. in *Journal of Investigative Dermatology Symposium Proceedings*. 2000. Elsevier.
15. Hinz, B., *Masters and servants of the force: the role of matrix adhesions in myofibroblast force perception and transmission.* European journal of cell biology, 2006. **85**(3-4): p. 175-181.
16. Rangaraj, A., K. Harding, and D.J.W.u. Leaper, *Role of collagen in wound management.* 2011. **7**(2): p. 54-63.
17. Guest, J.F., et al., *Health economic burden that different wound types impose on the UK's National Health Service.* 2017. **14**(2): p. 322-330.
18. Mathieu, D., J.-C. Linke, and F. Wattel, *Non-healing wounds*, in *Handbook on hyperbaric medicine*. 2006, Springer. p. 401-428.
19. Bates-Jensen, B.M., *Chronic wound assessment.* The Nursing clinics of North America, 1999. **34**(4): p. 799-845, v.
20. Penn-Barwell, J.G., et al., *Improved survival in UK combat casualties from Iraq and Afghanistan: 2003–2012.* 2015. **78**(5): p. 1014-1020.
21. Jeffery, S.L., *The management of combat wounds: the British Military Experience.* Advances in wound care, 2016. **5**(10): p. 464-473.
22. NATO, *Allied Joint Doctrine for Medical Support*. 2020.
23. Spear, A.M., et al., *Regenerative medicine and war: a front-line focus for UK defence.* npj Regenerative Medicine, 2018. **3**(1): p. 13.
24. Jeffery, S., *Wound imaging: from Waterloo to tomorrow*. 2014, MA Healthcare London.

25. Savage, J. and S. Jeffery, *Use of 3D photography in complex-wound assessment.* Journal of wound care, 2013. **22**(3): p. 156-160.

26. Manna, B. and C.A. Morrison, *Wound debridement.* 2018.

27. Dorafshar, A.H., et al., *Guided surgical debridement: staining tissues with methylene blue.* J Burn Care Res, 2010. **31**(5): p. 791-4.

28. Dewachter, P., et al., *Severe anaphylactic shock with methylene blue instillation.* 2005. **101**(1): p. 149-150.

29. Dinc, S., et al., *Methylene blue prevents surgery-induced peritoneal adhesions but impairs the early phase of anastomotic wound healing.* 2006. **49**(5): p. 321.

30. Evriviades, D., et al., *Shaping the military wound: issues surrounding the reconstruction of injured servicemen at the Royal Centre for Defence Medicine.* 2011. **366**(1562): p. 219-230.

31. Gardi, L., *Planck's Constant and the Nature of Light*. 2018.

32. Wilson, B., *Modelling and measurements of light propagation in tissue for diagnostic and therapeutic applications*, in *Laser Systems for Photobiology and Photomedicine*. 1991, Springer. p. 13-27.

33. Young, H.D., et al., *University physics*. Vol. 9. 1996: Addison-Wesley Reading, MA.

34. Mayerhöfer, T.G., S. Pahlow, and J. Popp, *The Bouguer-Beer-Lambert law: Shining light on the obscure.* ChemPhysChem, 2020. **21**(18): p. 2029.

35. Bhatt, M., K.R. Ayyalasomayajula, and P.K. Yalavarthy, *Generalized Beer–Lambert model for near-infrared light propagation in thick biological tissues.* Journal of biomedical optics, 2016. **21**(7): p. 076012.

36. Steelman, Z.A., et al., *Light scattering methods for tissue diagnosis.* Optica, 2019. **6**(4): p. 479-489.

37. Tuchin, V.V. *Tissue optics*. 2015. Society of Photo-Optical Instrumentation Engineers (SPIE).

38. Scholkmann, F., et al., *A review on continuous wave functional near-infrared spectroscopy and imaging instrumentation and methodology.* NeuroImage, 2014. **85**: p. 6-27.

39. Zijlstra, W.G., A. Buursma, and O.W. van Assendelft, *Visible and near infrared absorption spectra of human and animal haemoglobin: determination and application*. 2000: VSP.

40. LaVan, F.B. and T.K. Hunt, *Oxygen and wound healing.* Clinics in plastic surgery, 1990. **17**(3): p. 463-472.

41. Wang, L.V. and H.-i. Wu, *Biomedical optics: principles and imaging*. 2012: John Wiley & Sons.

42. Wang, L., S.L. Jacques, and L. Zheng, *MCML—Monte Carlo modeling of light transport in multi-layered tissues.* Computer methods and programs in biomedicine, 1995. **47**(2): p. 131-146.

43. Dehghani, H., et al., *Near infrared optical tomography using NIRFAST: Algorithm for numerical model and image reconstruction.* Commun Numer Methods Eng, 2008. **25**(6): p. 711-732.

44. Swann, G., *Photography in wound care.* Nursing times, 2000. **96**(45 Suppl): p. 9-15.

45. Langemo, D., et al., *Digital Wound Photography: Points to Practice.* Advances in Skin & Wound Care, 2006. **19**(7).

46. Mukherjee, R., et al., *Automated tissue classification framework for reproducible chronic wound assessment.* 2014. **2014**.

47. Gaur, A., et al., *Efficient wound measurements using RGB and depth images.* 2015. **18**(4): p. 333-358.

48. Silva, R.H., A.M. Machado, and Regeneration, *A computational method for semi-automatic measurement of pressure ulcers.* Wound Repair, 2018. **26**(4): p. 332-339.

49. Goto, T., et al., *Objective evaluation for venous leg ulcer-related nociceptive pain using thermography.* 2014. **1**: p. 23-30.

50.   Lawson, R.N., G. Wlodek, and D. Webster, *Thermographic assessment of burns and frostbite.* Canadian Medical Association Journal, 1961. **84**(20): p. 1129.

51.   Renkielska, A., et al., *Static thermography revisited—an adjunct method for determining the depth of the burn injury.* 2005. **31**(6): p. 768-775.

52.   Ruminski, J., et al., *Thermal parametric imaging in the evaluation of skin burn depth.* 2007. **54**(2): p. 303-312.

53.   Yi, S., et al. *Enhance wound healing monitoring through a thermal imaging based smartphone app*. in *Medical Imaging 2018: Imaging Informatics for Healthcare, Research, and Applications*. 2018. International Society for Optics and Photonics.

54.   Bharara, M., et al., *Wound inflammatory index: a "proof of concept" study to assess wound healing trajectory*. 2010, SAGE Publications.

55.   Bharara, M., et al., *Coming events cast their shadows before: detecting inflammation in the acute diabetic foot and the foot in remission.* 2012. **28**: p. 15-20.

56.   Rathmann, P., et al., *Dynamic infrared thermography (DIRT) for assessment of skin blood perfusion in cranioplasty: a proof of concept for qualitative comparison with the standard indocyanine green video angiography (ICGA).* 2018. **13**(3): p. 479-490.

57.   Deka, G., W.-W. Wu, and F.-J. Kao, *In vivo wound healing diagnosis with second harmonic and fluorescence lifetime imaging.* Journal of biomedical optics, 2012. **18**(6): p. 061222.

58.   Gschwandtner, M.E., et al., *Microcirculation is similar in ischemic and venous ulcers.* 2001. **62**(3): p. 226-235.

59.   DaCosta, R.S., et al., *Point-of-care autofluorescence imaging for real-time sampling and treatment guidance of bioburden in chronic wounds: first-in-human results.* PloS one, 2015. **10**(3): p. e0116623-e0116623.

60.   Farrakhova, D., A. Borodkin, and V. Makarov. *The concept of the portable spectrometer for fast assessment of skin engraftment via exogenous and endogenous fluorophores*. in *Optical Instrument Science, Technology, and Applications*. 2018. International Society for Optics and Photonics.

61.   Albert, H., *A survey of optical imaging techniques for assessing wound healing.* Int. J. Intell. Control. Syst, 2012. **17**: p. 79-85.

62.   Fei, B., *Chapter 3.6 - Hyperspectral imaging in medical applications*, in *Data Handling in Science and Technology*, J.M. Amigo, Editor. 2020, Elsevier. p. 523-565.

63.   Calin, M.A., et al., *Characterization of burns using hyperspectral imaging technique–A preliminary study.* 2015. **41**(1): p. 118-124.

64.   Jolivot, R., F. Marzani, and P. Vabres, *An open system to generate hyperspectral cubes for skin optical reflectance analysis.* 2010.

65.   Nouri, D., et al. *Colour and multispectral imaging for wound healing evaluation in the context of a comparative preclinical study*. in *Medical Imaging 2013: Image Processing*. 2013. International Society for Optics and Photonics.

66.   Moza, R., J.M. DiMaio, and J. Melendez, *Deep-Tissue Dynamic Monitoring of Decubitus Ulcers: Wound Care and Assessment.* IEEE Engineering in Medicine and Biology Magazine, 2010. **29**(2): p. 71-77.

67.   Weingarten, M.S., et al., *Diffuse near-infrared spectroscopy prediction of healing in diabetic foot ulcers: A human study and cost analysis.* 2012. **20**(6): p. 911-917.

68.   Sowa, M.G., et al., *Near infrared spectroscopic assessment of hemodynamic changes in the early post-burn period.* Burns, 2001. **27**(3): p. 241-249.

69.   Landsman, A.S., D. Barnhart, and M. Sowa, *Near-Infrared Spectroscopy Imaging for Assessing Skin and Wound Oxygen Perfusion.* Clinics in Podiatric Medicine and Surgery, 2018. **35**(3): p. 343-355.

70.   Murray, A., A. Herrick, and T.J.R. King, *Laser Doppler imaging: a developing technique for application in the rheumatic diseases.* 2004. **43**(10): p. 1210-1218.

71. Monstrey, S., et al., *Assessment of burn depth and burn wound healing potential.* 2008. **34**(6): p. 761-769.

72. Jan, S.N., et al., *Comparison of Laser Doppler Imaging (LDI) and clinical assessment in differentiating between superficial and deep partial thickness burn wounds.* 2018. **44**(2): p. 405-413.

73. Andersen, C.A., *Noninvasive assessment of lower-extremity hemodynamics in individuals with diabetes mellitus.* Journal of the American Podiatric Medical Association, 2010. **100**(5): p. 406-411.

74. Mayrovitz, H.N., et al., *Heel skin hyperaemia: direct compression versus vascular occlusion.* 2003. **23**(6): p. 354-359.

75. Ghassemi, P., et al., *A polarized multispectral imaging system for quantitative assessment of hypertrophic scars.* 2014. **5**(10): p. 3337-3354.

76. Lal, C., A. Banerjee, and N.U. Sujatha, *Role of contrast and fractality of laser speckle image in assessing flow velocity and scatterer concentration in phantom body fluids.* Journal of biomedical optics, 2013. **18**(11): p. 111419.

77. Ponticorvo, A., et al. *Quantitative assessment of graded burn wounds using a commercial and research grade laser speckle imaging (LSI) system*. in *Photonics in Dermatology and Plastic Surgery*. 2017. International Society for Optics and Photonics.

78. Gioux, S., et al., *Three-dimensional surface profile intensity correction for spatially modulated imaging.* Journal of biomedical optics, 2009. **14**(3): p. 034045.

79. Gioux, S., A. Mazhar, and D.J. Cuccia, *Spatial frequency domain imaging in 2019: principles, applications, and perspectives.* J Biomed Opt, 2019. **24**(7): p. 1-18.

80. Murphy, G.A., et al., *Quantifying dermal microcirculatory changes of neuropathic and neuroischemic diabetic foot ulcers using spatial frequency domain imaging: a shade of things to come?* 2020. **8**(2): p. e001815.

81. Burmeister, D.M., et al., *Utility of spatial frequency domain imaging (SFDI) and laser speckle imaging (LSI) to non-invasively diagnose burn depth in a porcine model.* 2015. **41**(6): p. 1242-1252.

82. Nguyen, J.Q.M., et al., *Spatial frequency domain imaging of burn wounds in a preclinical model of graded burn severity.* 2013. **18**(6): p. 066010.

83. Yafi, A., et al., *Postoperative quantitative assessment of reconstructive tissue status in cutaneous flap model using spatial frequency domain imaging.* 2011. **127**(1): p. 117.

84. Yafi, A., et al., *Quantitative skin assessment using spatial frequency domain imaging (SFDI) in patients with or at high risk for pressure ulcers.* Lasers Surg Med, 2017. **49**(9): p. 827-834.

85. Deegan, A.J., et al., *Optical coherence tomography angiography monitors human cutaneous wound healing over time.* Quantitative imaging in medicine and surgery, 2018. **8**(2): p. 135-150.

86. Song, S., J. Xu, and R.K. Wang, *Long-range and wide field of view optical coherence tomography for in vivo 3D imaging of large volume object based on akinetic programmable swept source.* Biomedical optics express, 2016. **7**(11): p. 4734-4748.

87. Pierce, M.C., et al., *Collagen denaturation can be quantified in burned human skin using polarization-sensitive optical coherence tomography.* 2004. **30**(6): p. 511-517.

88. Kim, K.H., et al., *In vivo imaging of human burn injuries with polarization-sensitive optical coherence tomography.* 2012. **17**(6): p. 066012.

89. Cobb, M.J., et al., *Noninvasive assessment of cutaneous wound healing using ultrahigh-resolution optical coherence tomography.* 2006. **11**(6): p. 064002.

90. Borman, S.A., *Nonlinear Raman spectroscopy.* Analytical Chemistry, 1982. **54**(9): p. 1021A-1026A.

91. Jain, R., et al., *Raman spectroscopy enables noninvasive biochemical characterization and identification of the stage of healing of a wound.* 2014. **86**(8): p. 3764-3772.

92. Zhai, L., et al., *Prediction of steam burns severity using Raman spectroscopy on ex vivo porcine skin.* 2018. **8**(1): p. 6946.

93. Mao, X., *Evaluation of chronic wounds by raman spectroscopy and image processing.* 2012.

94. Howle, C.R., et al. *Monitoring combat wound healing by IR hyperspectral imaging*. in *Optical Biopsy XIV: Toward Real-Time Spectroscopic Imaging and Diagnosis*. 2016. International Society for Optics and Photonics.

95. Clewes, R., et al., *Stand-off spectroscopy for the detection of chemical warfare agents*. SPIE Security + Defence. Vol. 8546. 2012: SPIE.

96. Howle, C.R., et al. *Hazardous liquid detection by active hyperspectral imaging*. in *Optics and Photonics for Counterterrorism and Crime Fighting VII; Optical Materials in Defence Systems Technology VIII; and Quantum-Physics-based Information Security*. 2011. International Society for Optics and Photonics.

97. Héder, M., *From NASA to EU: the evolution of the TRL scale in Public Sector Innovation.* The Innovation Journal, 2017. **22**(2): p. 1-23.

98. Linick, J. *Technology Readiness Level (TRL) vs. Percent Development Cost*. in *2017 International Cost Estimating and Analysis Association Professional Development and Training Workshop, Portland, United States*. 2017.

99. Famili, A., et al., *Data preprocessing and intelligent data analysis.* 1997. **1**(1): p. 3-23.

100. Kumar, K.S., B.E.J.S. Reddy, and I. Processing, *Wound image analysis classifier for efficient tracking of wound healing status.* 2014. **5**(2): p. 15.

101. Kerekes, J.P. and J.E.J.L.L.J. Baum, *Hyperspectral imaging system modeling.* 2003. **14**(1): p. 117-130.

102. Delode, J., et al., *A wound-healing monitoring system.* ITBM-RBM, 2001. **22**(1): p. 49-52.

103. Chakraborty, C., *Chronic wound image analysis by particle swarm optimization technique for tele-wound network.* Journal Wireless Personal Communications, 2017. **96**(3): p. 3655-3671.

104. Dhane, D.M., et al., *Fuzzy spectral clustering for automated delineation of chronic wound region using digital images.* 2017. **89**: p. 551-560.

105. Yadav, M.K., et al., *Segmentation of chronic wound areas by clustering techniques using selected color space.* 2013. **3**(1): p. 22-29.

106. Shenoy, V.N., et al. *Deepwound: Automated postoperative wound assessment and surgical site surveillance through convolutional neural networks*. in *2018 IEEE International Conference on Bioinformatics and Biomedicine (BIBM)*. 2018. IEEE.

107. Baker, M.J., et al., *Using Fourier transform IR spectroscopy to analyze biological materials.* 2014. **9**(8): p. 1771-1791.

108. Rinnan, Å., F. Van Den Berg, and S.B. Engelsen, *Review of the most common pre-processing techniques for near-infrared spectra.* Trends in Analytical Chemistry, 2009. **28**(10): p. 1201-1222.

109. Baker, M.J., et al., *Using Fourier transform IR spectroscopy to analyze biological materials.* Nature Protocols, 2014. **9**: p. 1771.

110. Saiko, G., et al., *Hyperspectral imaging in wound care: A systematic review.* 2020. **17**(6): p. 1840-1856.

111. Yang, Q., et al., *Investigation of the Performance of Hyperspectral Imaging by Principal Component Analysis in the Prediction of Healing of Diabetic Foot Ulcers.* 2018. **4**(12): p. 144.

112. Ding, H. and R.C. Chang. *Comparison of photometric stereo and spectral analysis for visualization and assessment of burn injury from hyperspectral imaging*. in *2015 IEEE International Conference on Computational Intelligence and Virtual Environments for Measurement Systems and Applications (CIVEMSA)*. 2015.

113. Lasch, P., et al., *Imaging of colorectal adenocarcinoma using FT-IR microspectroscopy and cluster analysis.* Biochimica et Biophysica Acta -Molecular Basis of Disease, 2004. **1688**(2): p. 176-186.

114. Dhane, D.M., et al., *Spectral Clustering for Unsupervised Segmentation of Lower Extremity Wound Beds Using Optical Images.* Journal of Medical Systems, 2016. **40**: p. 1-10.

115. Wahabzada, M., et al., *Monitoring wound healing in a 3D wound model by hyperspectral imaging and efficient clustering.* PLoS One, 2017. **12**(12): p. e0186425.

116. Kannan, S., S. Ramathilagam, and A. Sathya. *Robust fuzzy C-means in classifying breast tissue regions*. in *2009 International Conference on Advances in Recent Technologies in Communication and Computing*. 2009. IEEE.

117. Ahmad, N.N., et al., *Characterization of Tissues in Chronic Wound Images.* 2019.

118. Su, J.W., et al., *Depth-sensitive Raman spectroscopy for skin wound evaluation in rodents.* Biomedical optics express, 2019. **10**(12): p. 6114-6128.

119. Chakraborty, C., B. Gupta, and S.K. Ghosh, *Chronic wound characterization using bayesian classifier under telemedicine framework*, in *Medical Imaging: Concepts, Methodologies, Tools, and Applications*. 2017, IGI Global. p. 741-760.

120. Yin, M., et al., *Identification of microbes in wounds using near-infrared spectroscopy.* Burns, 2021.

121. Ohura, N., et al., *Convolutional neural networks for wound detection: the role of artificial intelligence in wound care.* 2019. **28**(Sup10): p. S13-S24.

122. Kim, J., et al., *Novel burn device for rapid, reproducible burn wound generation.* 2016. **42**(2): p. 384-391.

123. Boccara, D. and K. Serror, *Use of digital photography in burn patients: Diagnosis, treatment and follow-up.* Burns, 2019. **45**(8): p. 1935-1936.

124. Ponticorvo, A., et al., *Spatial Frequency Domain Imaging (SFDI) of clinical burns: A case report.* Burns Open, 2020. **4**(2): p. 67-71.

125. Crane, N.J., et al., *Monitoring the healing of combat wounds using Raman spectroscopic mapping.* 2010. **18**(4): p. 409-416.

126. Mellors, B.O., et al. *Mid-infrared spectroscopic imaging to assess wounded tissue health*. in *Optical Biopsy XVII: Toward Real-Time Spectroscopic Imaging and Diagnosis*. 2019. International Society for Optics and Photonics.

127. Mellors, B.O.L., et al., *Machine learning utilising spectral derivative data improves cellular health classification through hyperspectral infra-red spectroscopy.* PLOS ONE, 2020. **15**(9): p. e0238647.

128. Meier, R.J., et al., *Simultaneous Photographing of Oxygen and pH In Vivo Using Sensor Films.* 2011. **50**(46): p. 10893-10896.

129. Crane, N.J. and E.A. Elster, *Vibrational spectroscopy: a tool being developed for the noninvasive monitoring of wound healing.* Journal of biomedical optics, 2012. **17**(1): p. 010902.

130. Crane, N.J., et al. *Developing a toolbox for analysis of warrior wound biopsies: vibrational spectroscopy*. in *Optical Biopsy IX*. 2011. International Society for Optics and Photonics.

131. Baker, S.P., et al., *The injury severity score: a method for describing patients with multiple injuries and evaluating emergency care.* 1974. **14**(3): p. 187-196.

132. Xu, R. and D.C. Wunsch, *Clustering algorithms in biomedical research: a review.* IEEE reviews in biomedical engineering, 2010. **3**: p. 120-154.

133. Deepak, S., P. Ameer, and medicine, *Brain tumor classification using deep CNN features via transfer learning.* Computers in biology, 2019. **111**: p. 103345.

134. Mueller, D., et al., *Fourier transform infrared spectroscopy (FTIR) and multivariate analysis for identification of different vegetable oils used in biodiesel production.* 2013. **13**(4): p. 4258-4271.

135. Ding, C. and X. He. *K-means clustering via principal component analysis*. in *Proceedings of the twenty-first international conference on Machine learning*. 2004.

136. Zhang, N., et al. *Pca-k-means based clustering algorithm for high dimensional and overlapping spectra signals*. in *2018 Ninth International Conference on Intelligent Control and Information Processing (ICICIP)*. 2018. IEEE.

137. Diakides, M., J.D. Bronzino, and D.R. Peterson, *Medical infrared imaging: principles and practices*. 2012: CRC press.

138. Harding, J., et al. *Infrared imaging in diabetic foot ulceration*. in *Proceedings of the 20th Annual International Conference of the IEEE Engineering in Medicine and Biology Society. Vol. 20 Biomedical Engineering Towards the Year 2000 and Beyond (Cat. No. 98CH36286)*. 1998. IEEE.

139. Medina-Preciado, J.D., et al., *Noninvasive determination of burn depth in children by digital infrared thermal imaging.* 2012. **18**(6): p. 061204.

140. Thimsen, E., B. Sadtler, and Y. Berezin Mikhail, *Shortwave-infrared (SWIR) emitters for biological imaging: a review of challenges and opportunities*, in *Nanophotonics*. 2017. p. 1043.

141. Diem, M., et al., *Applications of Infrared and Raman Microspectroscopy of Cells and Tissue in Medical Diagnostics: Present Status and Future Promises %J Spectroscopy: An International Journal.* 2012. **27**(5-6): p. 34.

142. Marcsisin, E.J., *Infrared spectroscopy to monitor drug response of individual live cells.* 2011.

143. Wrobel, T.P. and R. Bhargava, *Infrared Spectroscopic Imaging Advances as an Analytical Technology for Biomedical Sciences.* Analytical Chemistry, 2018. **90**(3): p. 1444-1463.

144. Hobro, A.J. and N.I. Smith, *An evaluation of fixation methods: Spatial and compositional cellular changes observed by Raman imaging.* Vibrational Spectroscopy, 2017. **91**: p. 31-45.

145. Kennedy, G.T., et al., *Spatial frequency domain imaging: a quantitative, noninvasive tool for in vivo monitoring of burn wound and skin graft healing.* J Biomed Opt, 2019. **24**(7): p. 1-9.

146. Moss, D.A., M. Keese, and R. Pepperkok, *IR microspectroscopy of live cells.* Vibrational Spectroscopy, 2005. **38**(1): p. 185-191.

147. Matthäus, C., et al., *Infrared and Raman microscopy in cell biology.* Methods in cell biology, 2008. **89**: p. 275-308.

148. Birarda, G., et al., *IR-Live: fabrication of a low-cost plastic microfluidic device for infrared spectromicroscopy of living cells.* 2016. **16**(9): p. 1644-1651.

149. Zelig, U., et al., *Diagnosis of cell death by means of infrared spectroscopy.* 2009. **97**(7): p. 2107-2114.

150. Wilson, R.H., et al., *Review of short-wave infrared spectroscopy and imaging methods for biological tissue characterization.* Journal of Biomedical Optics, 2015. **20**(3): p. 1-10, 10.

151. Deo, R.C., *Machine Learning in Medicine.* 2015. **132**(20): p. 1920-1930.

152. Raza, K. and N.K. Singh, *A tour of unsupervised deep learning for medical image analysis.* arXiv preprint arXiv:.07715, 2018.

153. Selvan, A.N., et al., *Hierarchical Cluster Analysis to Aid Diagnostic Image Data Visualization of MS and Other Medical Imaging Modalities*, in *Imaging Mass Spectrometry : Methods and Protocols*, L.M. Cole, Editor. 2017, Springer New York: New York, NY. p. 95-123.

154. Kavvadias, V., et al. *A novel endoscopic spectral imaging platform integrating k-means clustering for early and non-invasive diagnosis of endometrial pathology*. in *2013 35th Annual International Conference of the IEEE Engineering in Medicine and Biology Society (EMBC)*. 2013. IEEE.

155. Jolliffe, I.T. and J. Cadima, *Principal component analysis: a review and recent developments.* Philos Trans A Math Phys Eng Sci, 2016. **374**(2065): p. 20150202.

156. Bonnier, F. and H.J.A. Byrne, *Understanding the molecular information contained in principal component analysis of vibrational spectra of biological systems.* 2012. **137**(2): p. 322-332.

157. Teramoto, S., et al., *Hydrogen peroxide-induced apoptosis and necrosis in human lung fibroblasts: protective roles of glutathione.* Jpn J Pharmacol, 1999. **79**(1): p. 33-40.

158. Borner, M.M., et al., *The detergent Triton X-100 induces a death pattern in human carcinoma cell lines that resembles cytotoxic lymphocyte-induced apoptosis.* FEBS Lett, 1994. **353**(2): p. 129-32.

159. Demetriades-Shah, T.H., M.D. Steven, and J.A. Clark, *High resolution derivative spectra in remote sensing.* Remote Sensing of Environment, 1990. **33**(1): p. 55-64.

160. Dehghani, H., et al., *Application of spectral derivative data in visible and near-infrared spectroscopy.* 2010. **55**(12): p. 3381.

161. Dehghani, H., et al., *Quantitative bioluminescence tomography using spectral derivative data.* 2018. **9**(9): p. 4163-4174.

162. Castro, P., T. Zorn, and D. Zezell. *Biochemical characterization of skin burn wound healing using ATR-FTIR*. in *2018 SBFoton International Optics and Photonics Conference (SBFoton IOPC)*. 2018.

163. MacQueen, J. *Some methods for classification and analysis of multivariate observations*. in *Proceedings of the fifth Berkeley symposium on mathematical statistics and probability*. 1967. Oakland, CA, USA.

164. Wold, S., K. Esbensen, and P. Geladi, *Principal component analysis.* Chemometrics and Intelligent Laboratory Systems, 1987. **2**(1): p. 37-52.

165. Assent, I., *Clustering high dimensional data.* WIREs Data Mining and Knowledge Discovery, 2012. **2**(4): p. 340-350.

166. Tsai, F. and W. Philpot, *Derivative Analysis of Hyperspectral Data.* Remote Sensing of Environment, 1998. **66**(1): p. 41-51.

167. Maitra, S. and J. Yan, *Principle component analysis and partial least squares: Two dimension reduction techniques for regression.* Applying Multivariate Statistical Models, 2008. **79**: p. 79-90.

168. Guo, S., et al., *Modified PCA and PLS: Towards a better classification in Raman spectroscopy–based biological applications.* 2020. **34**(4): p. e3202.

169. Wahabzada, M., et al., *Monitoring wound healing in a 3D wound model by hyperspectral imaging and efficient clustering.* 2017. **12**(12): p. e0186425.

170. Struyf, A., et al., *Integrating robust clustering techniques in S-PLUS.* 1997. **26**(1): p. 17-37.

171. Applegate, M., et al., *OpenSFDI: an open-source guide for constructing a spatial frequency domain imaging system.* Journal of Biomedical Optics, 2020. **25**(1): p. 016002.

172. Hayakawa, C., et al., *Optical sampling depth in the spatial frequency domain.* 2018. **24 %J Journal of Biomedical Optics**(7): p. 071603.

173. Mellors, B.O., et al., *Applications of compressive sensing in spatial frequency domain imaging.* 2020. **25**(11): p. 112904.

174. Cuccia, D.J., et al., *Quantitation and mapping of tissue optical properties using modulated imaging.* J Biomed Opt, 2009. **14**(2): p. 024012.

175. Sylvain, G., et al., *First-in-human pilot study of a spatial frequency domain oxygenation imaging system.* Journal of Biomedical Optics, 2011. **16**(8): p. 1-11.

176. Mazhar, A., et al., *Wavelength optimization for rapid chromophore mapping using spatial frequency domain imaging.* J Biomed Opt, 2010. **15**(6): p. 061716.

177. Wilson, R.H., et al., *Quantitative short-wave infrared multispectral imaging of in vivo tissue optical properties.* J Biomed Opt, 2014. **19**(8): p. 086011.

178. Matthew, B.A. and M.R. Darren, *High-speed spatial frequency domain imaging with temporally modulated light.* Journal of Biomedical Optics, 2017. **22**(7): p. 1-7.

179. Vervandier, J. and S. Gioux, *Single snapshot imaging of optical properties.* Biomedical Optics Express, 2013. **4**(12): p. 2938-2944.

180. Torabzadeh, M., et al., *Compressed single pixel imaging in the spatial frequency domain.* J Biomed Opt, 2017. **22**(3): p. 30501.

181. Torabzadeh, M., et al., *Hyperspectral imaging in the spatial frequency domain with a supercontinuum source.* 2019. **24**(7): p. 071614.

182. Edgar, M.P., G.M. Gibson, and M.J.J.N.p. Padgett, *Principles and prospects for single-pixel imaging.* 2019. **13**(1): p. 13-20.

183. Bentley, A., J.E. Rowe, and H. Dehghani, *Single pixel hyperspectral bioluminescence tomography based on compressive sensing.* Biomedical Optics Express, 2019. **10**(11): p. 5549-5564.

184. Farina, A., et al., *Multiple-view diffuse optical tomography system based on time-domain compressive measurements.* 2017. **42**(14): p. 2822-2825.

185. Ochoa, M., et al., *Assessing patterns for compressive fluorescence lifetime imaging.* 2018. **43**(18): p. 4370-4373.

186. Pian, Q., et al., *Compressive hyperspectral time-resolved wide-field fluorescence lifetime imaging.* 2017. **11**(7): p. 411-414.

187. S.Gioux. *AppSFDI*. 2019 [cited 2019 29/7]; Available from: https://healthphotonics.org/ressources/sfdi-resources/.

188. Donoho, D.L., *For most large underdetermined systems of linear equations the minimal* Communications on Pure Applied Mathematics: A Journal Issued by the Courant Institute of Mathematical Sciences, 2006. **59**(6): p. 797-829.

189. Blumensath, T., *Compressed sensing with nonlinear observations and related nonlinear optimization problems.* IEEE Transactions on Information Theory, 2013. **59**(6): p. 3466-3474.

190. Vane, G., et al., *The airborne visible/infrared imaging spectrometer (AVIRIS).* 1993. **44**(2-3): p. 127-143.

191. Hu, D., et al., *Noncontact and wide-field characterization of the absorption and scattering properties of apple fruit using spatial-frequency domain imaging.* 2016. **6**(1): p. 1-11.

192. Mellors, B.O. and H. Dehghani. *A Pixel-Dependent Finite Element Model for Spatial Frequency Domain Imaging Using NIRFAST*. in *Photonics*. 2021. Multidisciplinary Digital Publishing Institute.

193. Angelo, J.P., et al., *Review of structured light in diffuse optical imaging*. Vol. 24. 2018: SPIE. 1-20, 20.

194. Fang, Q. and D.A. Boas, *Monte Carlo simulation of photon migration in 3D turbid media accelerated by graphics processing units.* Optics express, 2009. **17**(22): p. 20178-20190.

195. Yao, R., X. Intes, and Q. Fang, *Generalized mesh-based Monte Carlo for wide-field illumination and detection via mesh retessellation.* Biomedical optics express, 2016. **7**(1): p. 171-184.

196. Tabassum, S., et al., *Two-layer inverse model for improved longitudinal preclinical tumor imaging in the spatial frequency domain.* 2018. **23**(7): p. 076011.

197. Doulgerakis, M., A.T. Eggebrecht, and H.J.N. Dehghani, *High-density functional diffuse optical tomography based on frequency-domain measurements improves image quality and spatial resolution.* 2019. **6**(3): p. 035007.

198. Lighter, D., A. Filer, and H.J.J.o.b.o. Dehghani, *Detecting inflammation in rheumatoid arthritis using Fourier transform analysis of dorsal optical transmission images from a pilot study.* 2019. **24**(6): p. 066008.

199. Hu, D., et al., *A stepwise method for estimating optical properties of two-layer turbid media from spatial-frequency domain reflectance.* 2019. **27**(2): p. 1124-1141.

200. Aguénounon, E., et al., *Real-time, wide-field and high-quality single snapshot imaging of optical properties with profile correction using deep learning.* Biomedical Optics Express, 2020. **11**(10): p. 5701-5716.

201. Haskell, R.C., et al., *Boundary conditions for the diffusion equation in radiative transfer.* 1994. **11**(10): p. 2727-2741.

202. Durduran, T., et al., *Diffuse Optics for Tissue Monitoring and Tomography.* Reports on progress in physics. Physical Society (Great Britain), 2010. **73**(7): p. 076701.

203. Simon, P.E. *Skin Wound Healing*. 2018 [cited 2018 17/7]; Available from: https://emedicine.medscape.com/article/884594-overview.

204. Kirkman, E., S. Watts, and G. Cooper, *Blast injury research models.* Philosophical Transactions of the Royal Society B: Biological Sciences, 2011. **366**(1562): p. 144-159.

205. Nourian Dehkordi, A., et al., *Skin tissue engineering: wound healing based on stem-cell-based therapeutic strategies.* Stem Cell Research & Therapy, 2019. **10**(1): p. 111.

206. Alwosheel, A., S. van Cranenburgh, and C.G. Chorus, *Is your dataset big enough? Sample size requirements when using artificial neural networks for discrete choice analysis.* Journal of Choice Modelling, 2018. **28**: p. 167-182.

207. Beleites, C., et al., *Sample size planning for classification models.* J Analytica chimica acta, 2013. **760**: p. 25-33.